UNIVERSITY OF MANCHESTER

The Radiolytic Steady-State and Factors Controlling H_2 Production

School of Chemistry

Thomas Donoclift

2016

A thesis submitted to the University of Manchester for the degree of Doctor of Philosophy in the Faculty of Engineering and Physical Science

Table of Contents

List of Figures

List of Tables

List of Acronyms and Initialisms

AES	-	Atomic Emission Spectroscopy
AVIDAC	-	Argonne Version of the Institute's Digital Automatic Computer
CANDU	-	Canada Deuterium-Uranium
DCF	-	Dalton Cumbrian Facility
EDTA	-	Ethylenediaminetetraacetic acid
EPSRC	-	Engineering and Physical Sciences Research Council
FGMSP	-	First Generation Magnox Storage Pond
GC	-	Gas Chromatography
HDEHP	-	Di-(2-ethylhexyl)phosphoric acid
HPLC	-	High Performance Liquid Chromatography
ICP	-	Inductively Coupled Plasma
ISO	-	International Organization for Standardization
LET	-	Linear Energy Transfer
MOX	-	Mixed Oxide
MSSS	-	Magnox Swarf Storage Silo
NNL	-	National Nuclear Laboratory
ODE	-	Ordinary Differential Equation
PUREX	-	Plutonium Uranium Redox Extraction
PWR	-	Pressurised Water Reactor
SHE	-	Standard Hydrogen Electrode
SI	-	International System
TCD	-	Thermal Conductivity Detector
TGA	-	Thermogravimetric Analysis
TOC	-	Total Organic Carbon
UV	-	Ultra Violet
VIS	-	Visible

Word count - 42,500

Abstract

Sellafield is home to the UK's largest repository of nuclear waste, including reprocessed uranium and plutonium, as well as a backlog of unprocessed used fuel and waste kept in outdated storage facilities; commonly referred to as "legacy waste". For this reason, Sellafield has often been called the most hazardous place in Western Europe and as such, is currently undergoing a multi-billion pound decommissioning and clean-up operation. Each on-site facility has unique challenges associated with it, many of them presenting situations where the radiation chemistry aspects of the material degradation are not well understood. The key factors that can affect water radiolysis processes in the Sellafield challenges are a high pH environment, the presence of magnesium hydroxide, the presence of iron oxide, and the presence of organic materials. This work examines the effect each of these factors has on H_2 and H_2O_2 production in water radiolysis as well as developing a computational model to offer some understanding to the kinetic behaviour of water radiolysis under such conditions.

The computational model was able to replicate experimental measurements of radiolytic H_2 and H_2O_2 production in both aerated and deaerated water at neutral pH, and provide a further understanding of the role of dissolved oxygen in water radiolysis. Measurements of H_2O_2 from solutions containing NaOH have shown that an increase in pH generally results in a higher steady state of H_2O_2, while measurements of H_2 show a similar increase with a maximum production rate at pH ~11. The model was also able to closely replicate these experimental measurements with some over prediction, which highlights a gap in our understanding of high pH radiolysis and also brings into question the validity of the estimated rate constant for the reaction:

$$\boldsymbol{O^- + O_2^- \xrightarrow{H_2O} 2OH^- + O_2 \;\; k = \; 6.0 \times 10^8 \; M^{-1}s^{-1}}$$

which was originally determined from kinetic model calculations designed to describe the decay of ozonide (O_3^-) during pulse-radiolysis studies of high pH solutions conducted by K. Sehested et al in 1982.

The radiolysis of magnesium hydroxide slurry also resulted in an increased yield of hydrogen gas but had little effect on the yield of hydrogen peroxide. The hydrogen yield was 0.52 molecules per 100eV while a NaOH solution of equivalent pH gave a yield of 0.27, however interference from carbonate may be the cause of the increased yield. A surface effect was also estimated to contribute 0.05 molecules per 100 eV to the hydrogen gas yield.

Hydrogen gas and hydrogen peroxide was measured from the radiolysis of aqueous methanol. This was modelled with a near agreement, but modifications to the model were necessary; highlighting areas of the model that need improvement, as well as providing a reaction scheme from which a more comprehensive model for aqueous methanol radiolysis could be developed.

Declaration

No portion of the work referred to in the thesis has been submitted in support of an application for another degree or qualification of this or any other university or other institute of learning

Thomas A. Donoclift **August 2016**

Copyright Statement

Dedications

Mum

For the strength and freedom to explore
and the support and security to return

Dad

For the support and encouragement
exceeded only by pride

Acknowledgements

I would like to take this opportunity to thank some of the people who have made this work possible. My supervisor Simon Pimblott, even with the busy work schedule that comes with managing an entire research facility, he is still able to provide support and put the well-being of his students and staff above all else. My unofficial but very much appreciated industrial supervisors from the National Nuclear Laboratory (NNL) Howard Sims and Robin Orr, who both take a personal interest in the work going on at the Dalton Cumbrian Facility (DCF) and dedicate much of their own time to helping the researchers in their work.

I would like to acknowledge the EPSRC and Sellafield Ltd for providing the funding that supported this research.

A special thanks to all the members of the Dalton Cumbrian Facility, especially to all the staff who work immeasurably hard and with profound dedication to the values, management, and research carried out at the Dalton Cumbrian Facility. Acknowledgements to the academic staff, Ruth Edge, Aliaksandr Baidak, and Sven Koehler, for always providing a useful and meaningful insight to almost any situation, and for providing valuable guidance in practical radiation chemistry as well as the inspiration and encouragement to pursue potentially interesting avenues of research.

Thank you to the research team at the Dalton Cumbrian Facility for their friendship and for making the workplace an enjoyable place to conduct research.

Chapter 1: Introduction

Overview of Sellafield

Sellafield, shown in Figure 1, is the largest nuclear facility in the UK and has played a key role in the UK nuclear industry for over 60 years. Sellafield began as a Royal Ordinance Factory, producing weapons propellant for use in the Second World War. Soon after the war ended, Sellafield was renamed to Windscale and was repurposed to produce plutonium for the development of nuclear weapons in order to secure the UK's position in the nuclear arms race.

Several years later the focus on acquiring nuclear weapons shifted towards the development of new reactors for civil energy production, with Magnox reactors built on a neighbouring site known as Calder Hall. The two sites were later combined and were once again named Sellafield. Previous operations carried out at Sellafield meant the site was also in a good position to conduct fuel reprocessing operations, alongside energy production. Spent fuel is separated from its now contaminated cladding and dissolved in nitric acid; uranium and plutonium are separated by solvent extraction while the cladding is treated independently. At Sellafield, this industrial process meant storing the contaminated cladding swarf in underwater silos.

The fuel reprocessing process most commonly used is the Plutonium Uranium Redox Extraction method (PUREX) and produces a number of product streams including plutonium, uranium, and other highly active liquors.

The separated uranium can be re-enriched to produce reusable uranium fuel, or mixed with plutonium to produce mixed oxide (MOX) fuel, although much of the reclaimed uranium and plutonium remains unused and is stored at Sellafield. The remaining fission products, classified as high level waste, are treated in various ways, including vitrification, and are also stored at Sellafield.

Figure 1: *An aerial view of the Sellafield Site which covers approximately 6 km^2. Image provided by Sellafield Ltd Press Office.*

Magnox reactors are now an obsolete design of reactors that use unenriched uranium fuel, which was clad in an alloy comprising almost entirely of magnesium, with small amounts of aluminium. Spent fuel from Magnox reactors was briefly stored in a cooling pond before having the cladding removed for reprocessing of the fuel pellets.

The facilities used for this storage, shown in Figure 2, were called the First Generation Magnox Storage Pond (FGMSP) and the Magnox Swarf Storage Silos (MSSS), both of these facilities are now considered to be “Legacy” facilities.

Figure 2: *On the left is The First Generation Magnox Storage Pond (FGMSP) and on the right are the Magnox Swarf Storage Silos (MSSS).*
Images provided by Sellafield Ltd Press Office.

An extended shut down of reprocessing in the first generation reprocessing plant meant that fuel being stored in the Magnox pond was left far longer than intended, resulting in corrosion and a backlog of spent fuel. The Magnox Storage Pond now contains approximately 14,000 m^3 of contaminated water, which includes roughly 1200 m^3 of sludge consisting mainly of magnesium hydroxide and iron oxide.[1] Later, technological advancements rendered the wet storage of Magnox fuel cladding to be an obsolete method and operations moved towards dry storage. However, the construction of a new facility and the huge backlog of material stored in the silo also resulted in corrosion of stored fuel and eventually a state of disrepair for the Magnox Swarf Storage Silos. Both of these legacy facilities present a huge challenge for decommissioning operations as well as a unique opportunity for scientific research.

Radiation Chemistry

Radiation chemistry is the study of chemical change driven by the absorption of energy capable of causing ionisation. This ionising radiation can be of a particulate nature, including but not limited to, alpha (He^{2+}) and beta (e^-) radiation, or non-particulate such as gamma (γ) or X-ray radiation. Radiation chemistry and its experimental methods parallel in many ways to photochemistry, but the differences between the fields are well defined. The fundamental difference between the two fields of study is the quantity of energy involved in the initiation of reactions. In radiation chemistry, this energy is provided by the atomic decay of radioactive nuclei and is far higher than energy used in photochemistry, typically UV radiation. The lower initial energies used in photochemistry tend to only produce molecular excitations rather than direct ionisations. These lower incident energies also mean that each photon will usually only interact once and produce a uniform distribution of excited species in any plane perpendicular to the incident beam. The higher initial energies used in radiation chemistry, often provided by atomic decay, can produce both excitations and ionisations directly. Interactions between ionising radiation and a substance is not necessarily limited to only one interaction; a single high energy photon or particle may interact a number of times. This behaviour gives rise to a non-uniform, track-like structure of interactions; unlike the uniform distributions found in photochemistry.[2]

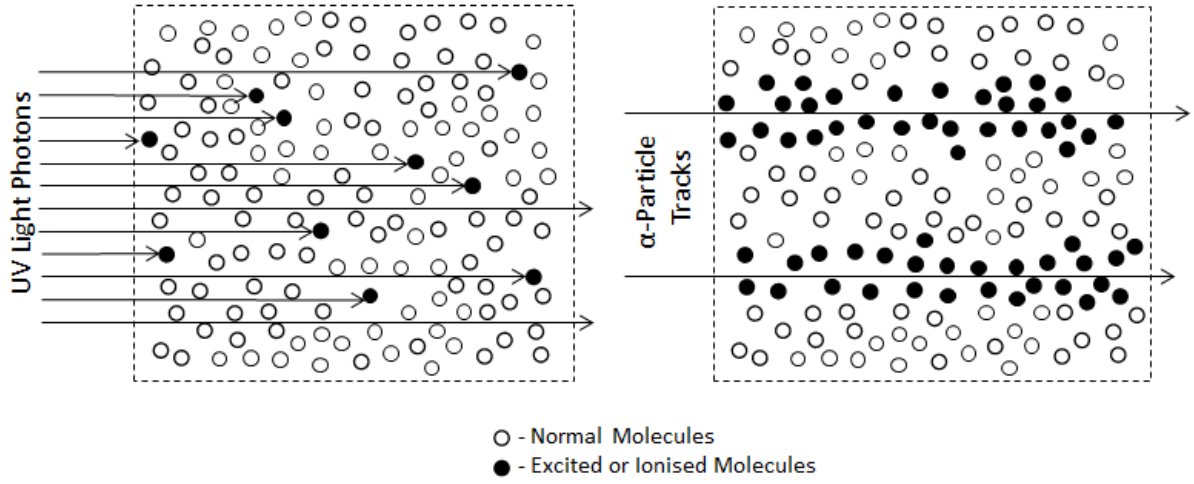

Figure 3: *A representation demonstrating the uniform excitations and ionisations of UV radiation compared to the structured tracks of alpha radiation.*

To fully appreciate the chemical changes initiated by ionising radiation, it is important to have some knowledge of the different types of ionising radiation and the ways in which they interacts with matter. There are two main ways in which radiation chemists provide a source of ionising radiation for experiments. The first involves taking advantage of the atomic decay of radioactive nuclei; this may be a naturally occurring radioisotope or an artificially created isotope. The second involves specialised equipment to directly generate radiation, usually by accelerating particles to a high energy. The major types of ionising radiation are alpha, beta, and gamma, however, in the field of radiation chemistry one may also come across the use of X-rays, fast neutron radiation, proton radiation, and other heavy charged particle radiation. This study utilises cobalt-60 as a source of gamma radiation; other types of radiation were not investigated during this work, however it is necessary to understand some fundamental features of alpha and beta decay to fully appreciate gamma decay.

Alpha α Radiation

Alpha radiation occurs when an unstable atomic nuclei spontaneously ejects an alpha particle. Elements with an atomic number greater than 83 will decay by this mechanism.[3] Alpha particles are fully ionised helium nuclei; they consist of two protons and two neutrons and have no electrons, which gives them a charge of +2. Alpha particles are mono-energetic; this means that every alpha particle emitted from a given radioactive element will have the same energy, characteristic of that element. These energy values typically range between 4 and 10 MeV. This quality means that research facilities capable of artificially producing alpha radiation by ionising and accelerating helium atoms, can select the particle energy required to effectively mimic alpha decay of any radioactive element.

Beta β Radiation

Beta decay involves the conversion of a neutron to a proton or vice versa in order to create a more favourable proton to neutron ratio. This conversion process is accompanied by the ejection of fundamental particles directly from the atomic nucleus. In the case of a neutron converting to a proton, the ejected particles are an anti-neutrino and a high energy electron, while in the reverse case the ejected particles are a neutrino and a positron (the antimatter equivalent of an electron). Unlike alpha particles, beta particles are not mono-energetic. The energy lost through beta decay is shared between the ejected particles and the recoil of the decaying atom; this means beta particle energy ranges from zero up to a maximum energy, characteristic of that element.

Gamma γ Radiation

Gamma radiation is not a particle like the previously mentioned types of radiation, but is a photon with a short wavelength in the region of 3 $x10^{-9}$ to 3 $x10^{-11}$ cm, or approximately 40 KeV to 4 MeV when converted to energy. A gamma ray is emitted when a nucleus in an excited state relaxes to a lower nuclear energy level; there is no change in the number of protons or neutrons during gamma decay. Gamma rays, like alpha particles, are mono-energetic; however, a nucleus may emit several photons as a cascade of energy loss. As gamma emission starts with an excited nucleus, some prior process must take place to result in a nucleus with an elevated energy level. For most gamma emitters, the process is initiated with either alpha or beta decay and the resulting atomic nucleus is left in an excited state. For example, ceasium-137 undergoes beta decay by emission of a beta particle of 1.174 MeV to form stable barium-137. This only happens 5.4% of the time and the more common decay mechanism is the emission of a beta particle of 0.512 MeV to form and excited barium-137 nucleus, this then emits a photon of 0.662 MeV to relax the nucleus to the stable barium-137.

Radiation interactions with matter

In order for radiation to induce a chemical change it must interact with matter in some way. There are many mechanisms by which radiation can interact with matter, as this project focuses on the use of gamma rays; a brief description of the interactions of gamma rays with matter is given below.

In the photoelectric effect, the entire energy of an incident gamma photon is transferred to an electron of some absorbing matter. This electron is ejected from the absorbing atom with energy equal to the incident photon minus the binding energy of that electron. The electrons ejected are often K-shell electrons which have the highest binding energy. As momentum and energy must be conserved it is necessary for the absorbing atom to recoil. As this mechanism involves the recoil of a parent atom, it would not be possible for the photoelectric effect to be the mechanism of interaction with free electrons that do not have a parent nucleus to recoil. In the photoelectric effect, ejected electrons will leave a hole, as this hole is filled by electrons from higher energy levels characteristic X-rays are emitted.

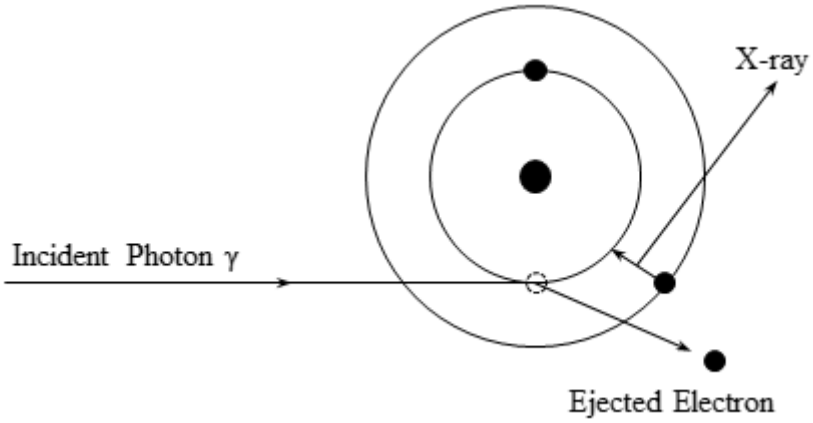

Figure 4: *A representation of the photoelectric effect. Image recreated from Spinks and Wood.*[2]

Although photons cannot interact with free electrons by means of the photoelectric effect, they may interact with free and loosely bound electrons through the Compton Effect. In this mechanism, a photon accelerates an electron thereby reducing its own energy. The photon is scattered, now with reduced energy, while the electron recoils with increased energy.

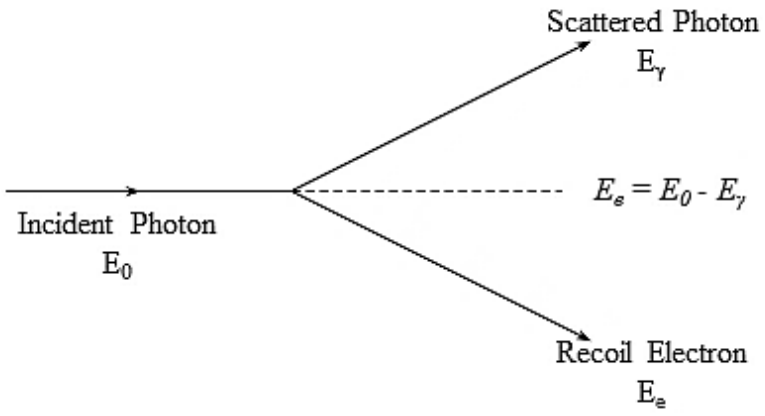

Figure 5: *A representation of the Compton Effect. Image recreated from Spinks and Wood.*[2]

Another mechanism by which a gamma ray may interact with matter is through pair-production. This is only a viable mechanism for photons with energy larger than 1.02 MeV. A photon is completely absorbed by an atomic nucleus and from that nucleus two particles are produced, an electron and a positron. The energy of the incident photon is shared between the rest energy of the two new particles and the kinetic energy of these particles as they move away from the nucleus, a negligible amount of energy is also used as the nucleus recoils. The positron behaves much the same way as the electron until it annihilates with an electron from the medium to produce two 0.51 MeV gamma rays, travelling at 180° from each other.

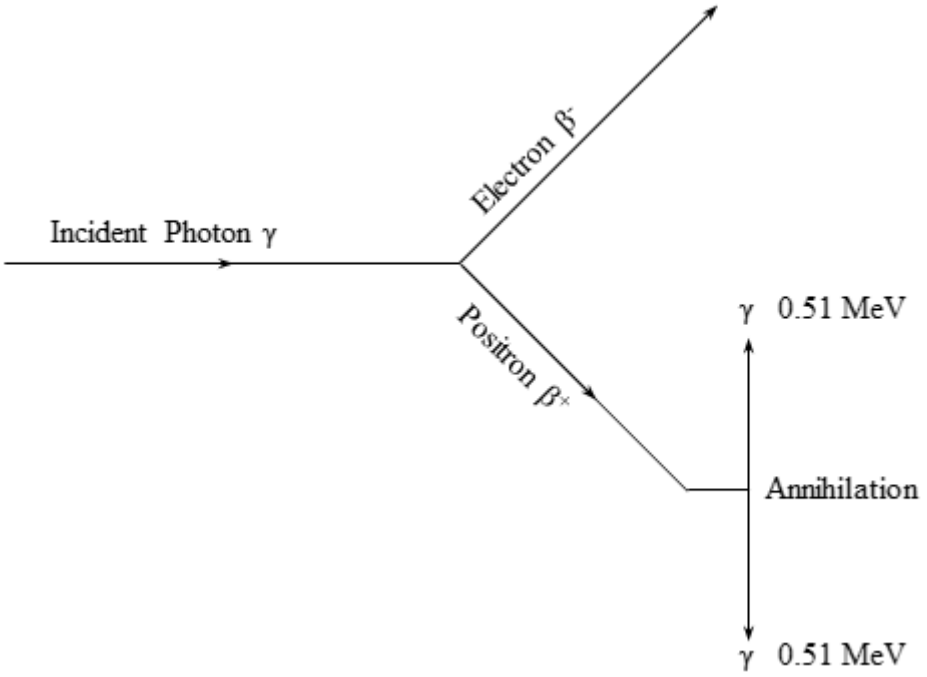

Figure 6: *A representation of pair production and positron annihilation. Image recreated from Spinks and Wood.*[2]

Generally, the interactions of gamma rays with matter result in fast moving electrons; these are often referred to as secondary electrons or delta-rays and have the same interactions with matter as beta particles. It is these secondary electrons that are predominantly responsible for producing the excited states and ionisations in an absorbing material that will initiate chemical changes in said material.[4] For this reason, it is necessary to also understand the interactions with matter these secondary electrons may have. Fast moving electrons lose energy through three main mechanisms; electromagnetic radiation, elastic scattering and inelastic scattering. When a fast electron greater than 100 KeV passes close to an atomic nucleus it is decelerated and slightly deflected. This event is accompanied by emission of electromagnetic radiation, commonly known as Bremsstrahlung radiation and is required for the conservation of energy.

At energies below 100 keV, Bremsstrahlung emission becomes negligible instead electrons tend to lose energy through scattering. Fast moving electrons interact with the bound electrons of a molecule predominantly through inelastic collisions. This interaction transfers energy from the incident electron to the bound molecular electron which can result in ionisation and excitation (and often with production of radical species). If there is an ionisation event, the tertiary electrons produced can cause more ionisation events in the same manner. These events tend to lie closer together as the electron that caused them has a much lower energy than the primary electron that passed by. This engenders a radiation track structure that consists of small groups of ionisation events. These groups are often referred to as spurs.

Fast moving electrons may also interact elastically with matter; this interaction causes the electrons to be deflected by a wide range of angles. This means that a fast moving electron may have moved a significant total distance but may have not travelled particularly far into the absorbing material.

Radiolysis of Water

As mentioned earlier, it is the secondary and tertiary electrons produced from gamma ray interactions that predominantly lead to the formation of ions and radical species that drives chemical change in substances exposed to radiation. Below is a diagram outlining the sequence of events and the different stages of water radiolysis.

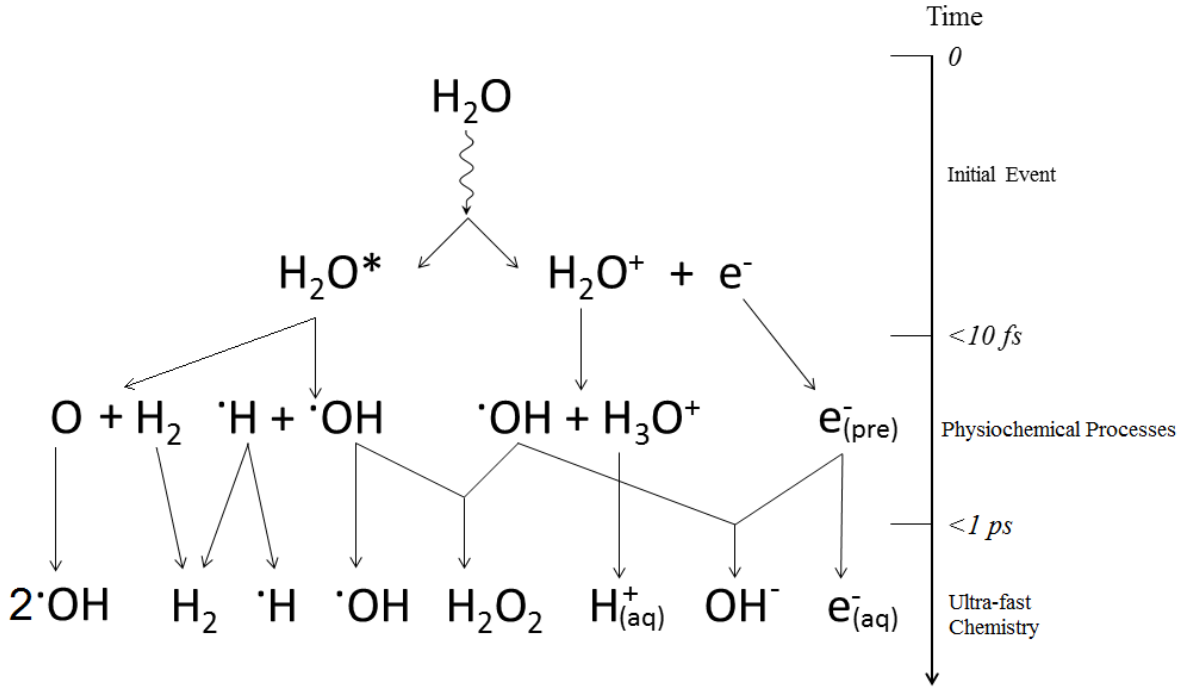

Figure 7: *A scheme showing the early stages of water radiolysis and the production of primary species.*

In water, this initial interaction between a gamma ray and a water molecule produces either an excited state of water or a water cation accompanied by an electron; this is achieved in less than ten femtoseconds (10^{-14}s). Molecules in an excited state may break apart to form hydrogen atoms and hydroxyl radicals or molecular hydrogen and oxygen atoms in a singlet or triplet state, while water cations will quickly react with nearby water molecules to produce hydronium ions and hydroxyl radicals.

The electron produced begins a thermalisation process eventually resulting in a solvated electron, however, at this stage the electron exists as a potentially reactive precursor intermediate. This happens in a time frame of less than 1 picosecond and occurs before diffusion of the spur. During the non-homogeneous stage the produced radicals and ions may react within the spur to produce molecular products such as H_2 and H_2O_2. Eventually the spur species diffuse into the bulk water and these "primary" species produced are said to be homogeneously distributed from this point onwards. The yield at which these primary species are produced are known as primary yields and are often expressed as G-values which have units of micromoles per Joule (SI unit) or molecules produced per 100 eV of energy absorbed (conventional historic units).

$$G = \frac{No.\,of\ molecules\ formed}{100\ eV}$$

This should not be confused with a "chemical" yield, which are the yields of chemical species sometime after homogeneous chemistry has taken place and is also often expressed as a G-value. During the homogeneous stage, reactions between primary species occur, often altering the observed production rates of these species through back reactions. To avoid confusion between the two types of yield a notation system can be used to discern the two. Two notation systems are commonly used throughout the radiation chemistry literature; the first denotes primary yields with the species of interest in subscript whilst the chemical yield is often expressed with the species of interest in parenthesis. For example, the primary and chemical yield of H_2 would be written as G_{H_2} and $G(H_2)$ respectively. The second system simply uses a lowercase "g" to denote primary yields and uppercase "G" for chemical yields. This study will use the latter system.

Most often it is the chemical yield that is measured during an experiment, but it is possible to measure a primary yield with the use of scavengers. A scavenger is a chemical species that can quickly react with a targeted primary species before it is able to diffuse into the bulk solution, effectively removing it and its associated chemistry from the homogeneous stage of radiolysis. The effectiveness of a scavenger is often referred to as the "scavenging capacity" and is quoted as the pseudo-first order rate of reaction between a scavenger (S) and a radical (R) which depends only on the rate constant for said reaction and the concentration of the scavenger. In other words, the scavenging capacity is equal to $\mathbf{k_{S+R}[S]}$.[5] A well-documented example of this is the use of bromide ions to prevent the reaction of hydroxyl radicals with molecular hydrogen, allowing for the room temperature primary yield of H_2 to be measured; this has been done extensively throughout the literature and the g-value is quoted to be 0.45 molecules/100eV.[6] Without the use of the bromide scavenger, hydroxyl radicals would react with H_2 reducing the observed yield; this reduced yield is what is meant by the term chemical yield.

The following summarises some of the properties of the more important primary radicals.

The Hydrated Electron, e_{aq}^-

One of the most reactive primary species of water radiolysis is the hydrated electron. It is a chemical entity that can be thought of as being a single electron somewhat stabilised by a cage of orientated water molecules. Hydrated electrons typically have reaction rate constants close to the diffusion controlled limit with low activation energies. Reactions of hydrated electrons are typically represented as single electron transfer processes and with a reduction potential of -2.9 V vs the standard hydrogen electrode (SHE), the hydrated electron will react with most other species.[7,8]

$$e_{aq}^- + S^n \rightarrow S^{n-1}$$

In the presence of organic compounds, the hydrated electron will act as a nucleophile with enhanced reactivity towards areas adjacent to electron withdrawing groups. Halogenated organics also show enhanced reactivity towards elimination of the halide ion.[9]

$$e_{aq}^- + RX \rightarrow RX^- \rightarrow R^\bullet + X^-$$

The Hydrogen Atom, $H^\cdot$

In terms of Brønsted–Lowry acid–base theory, the hydrogen atom is the conjugate acid of the hydrated electron with a pK_a of 9.6.[7,9]

$$e_{aq}^- + H_{(aq)}^+ \rightleftharpoons H^\bullet$$

The hydrogen atom has a reduction potential of -2.3 V[7,8], similar to that of the hydrated electron, however its chemistry is seldom the same.

Inorganic ions are reduced by the hydrogen atom at slower rates than reduction by the hydrated electron. In certain circumstances, such as in low pH environments, hydrogen atoms can act as an oxidant, reacting with inorganic ions to form a hydride intermediate that soon decomposes to form the oxidised ion and molecular hydrogen.[10]

$$H^{\bullet} + Fe^{2+} \rightarrow \{Fe^{3+}H^{-}\} \xrightarrow{H^{+}} Fe^{3+} + H_2$$

Organic molecules are also subject to oxidation reactions with the hydrogen atom. Saturated organics tend to react by hydrogen abstraction to form molecular hydrogen and a carbon centered organic radical. Unsaturated organics will react by hydrogen addition to the center of unsaturation, again forming a carbon centered organic radical.[9]

$$H^{\bullet} + CH_3OH \rightarrow {}^{\bullet}CH_2OH + H_2$$

$$H^{\bullet} + CH_2CH_2 \rightarrow {}^{\bullet}CH_2CH_3$$

The Hydroxyl Radical, $^{\bullet}$OH

Unlike the previously mentioned primary radicals, the hydroxyl radical has a positive reduction potential of 1.8 V in neutral solution, making it a powerful oxidising species.[11] Reactions of hydroxyl radicals with inorganic ions are often said to be simple electron transfer processes, however it has been suggested that the mechanism actually proceeds through an intermediate adduct.[12] Reactions with inorganic ions have been observed to proceed at rates close to the diffusion limit; however, this is not the case with many metal cations. Reaction rates between the hydroxyl radical and metal cations tend to be slower with rate constants of the order ~3.0 x10^8 M^{-1} s^{-1}.[9]

One explanation for this is that the mechanism for metal cation oxidation involves the addition of the hydroxyl radical to the metal cation, increasing its coordination number and allowing for inner-sphere oxidation to take place.

$$[M(H_2O)_x]^{n+} + {\cdot}OH \rightleftharpoons [(H_2O)_xM\text{-}OH]^{n+} \rightarrow [M(H_2O)_x]^{(n+1)+} + OH^-$$

The intermediate species, $M^{n+}OH$ has actually been observed in cases where M = Tl^+, Ag^+, Cu^{2+}, Sn^{2+}, Fe^{2+} and Mn^{2+}. [12]

As is the case with the hydrated electron and the hydrogen atom, the hydroxyl radical also exists in an acid-base equilibrium with the oxide radical anion $^{\bullet}O^-$.

$$^{\bullet}OH + OH^- \rightleftharpoons {}^{\bullet}O^- + H_2O$$

With a pK_a of 11.9, the reactions of $^{\bullet}O^-$ only become important at high pH. With a few exceptions, reactions of $^{\bullet}O^-$ are typically slower than those of $^{\bullet}OH$. The two species also have different reactivity towards organic molecules. Hydroxyl radicals tend to add to unsaturated bonds as an electrophile, while the conjugate base $^{\bullet}O^-$ acts more like a nucleophile and will abstract hydrogen from a hydrocarbon bond.

Computational Applications in Radiation Chemistry

Early computational studies in the field of radiation chemistry were focused largely on developing the radical diffusion theory and the non-homogeneous stage of water radiolysis to help rationalise experimental observations. One of the earliest water models used coupled differential equations with terms for the competing diffusion and reacting processes to represent the evolution of a spur containing six radical pairs, as a function of time.[13-15]

Although the predicted primary yields from this type of model agree well with experimental data, there are problems associated with this type of approach; the main problems arising from the application of classical chemical kinetics to a system of diminutive volume and extremely fast reactions occurring between only a few reactive species. Such deterministic models often use a typical spur to represent a whole system, fixing the average number of radical pairs as a single integer or in some cases a range of integers. This means that in deterministic models the long-running average value for the number of reactive species is neglected. This small difference can lead to inaccuracies in deterministic calculations of this kind, and so a stochastic approach became the preferred method to these types of non-homogeneous radiolysis calculations.[16]

Deterministic models however, are still the preferred technique for the longer term, homogeneous stage calculations for water radiolysis. Once a suitable set of primary yields has been established it is possible to model the subsequent chemistry in much the same way as any other chemical kinetics simulation.

By describing a reaction set in terms of a series of simultaneous differential equations and by including details of physical parameters such as temperature, it is possible to predict chemical yields of radiolysis and highlight important chemical pathways. This is the general methodology implemented in this study and will be discussed in further detail in subsequent chapters.

Deliverables and Project Aims

Given the technical challenges associated with the Sellafield site and the pressing conditions of legacy facilities, such as the First Generation Magnox Storage Pond and Magnox Swarf Storage Silos, there has been a renewed interest in water radiolysis; especially with respects to high pH and slurry systems. Previous radiolysis studies of high pH solutions have been contradictory and difficult to reproduce. There are very few situations in industry where knowledge of high pH water radiolysis is required as most situations where water radiolysis may occur are in acidic media, with the exception of Pressurised water reactors (PWRs) and CANDU reactor technology, which run under alkali conditions due to added LiOH.[17]

As mentioned previously, the Magnox Swarf Storage Silos at Sellafield Ltd contains large quantities of contaminated magnesium alloy produced from the de-cladding process of spent nuclear fuel. The material contaminated with uranium oxide is stored under water, and over time has corroded to produce large amounts of magnesium hydroxide. To prevent further corrosion, some of the 22 silos at the facility dose the water with sodium hydroxide. Although alleviating some corrosion, this addition increases the pH.

One of the aims of this project is to try and obtain a better understanding of water radiolysis at high pH. Using cobalt-60 as a source of gamma radiation and a range of analytical techniques to determine the production rates of H_2 and H_2O_2 as a function of absorbed dose, it is hoped that the effects of high pH on water radiolysis can be experimentally quantified.

Deterministic computational modelling is then used to investigate the experimentally observed effects of high pH in order to extract a better mechanistic understanding of water radiolysis at high pH.

While there were a number of early water radiolysis studies concerning the effects of various metal oxides and their surface interactions,[18] this is also a subject which has received a renewed scientific interest as there are many situations in the nuclear industry where an understanding of the effects of metal oxides on water radiolysis are significant. These areas include preventing corrosion within operational facilities to extend their lifetime, controlling radiolytic products associated with stored nuclear material, preventing incidences of unexpected gas build up, and managing already heavily corroded facilities such as the legacy ponds and silos at Sellafield Ltd.

In addition to sodium hydroxide, the Magnox Swarf Storage Silos also contain large quantities of magnesium hydroxide; the hydrated form of magnesium oxide. Radiolysis studies concerned with magnesium hydroxide solutions, slurries and solids are scarce,[1,19] despite the obvious need for further investigation. The slight solubility of magnesium hydroxide in water compels a prior understanding of high pH water radiolysis to facilitate understanding the effects of magnesium hydroxide and the presence of a surface. Data collected from experiments involving magnesium hydroxide are therefore also included in this project.

Up until now, the discussed aims of this project have been targeted at the issues associated with the Magnox Swarf Storage Silo rather than with the First Generation Magnox Storage Ponds. These legacy ponds are outdoor, open air ponds that have been used to store spent nuclear fuel for extended periods (far longer than ever intended). As the ponds are open air, they are susceptible to the introduction of natural debris, mostly falling leaves and other biological matter.

This has led to an interest in the effects of organic substances on radiolysis processes in water, with the focus being on some of the decomposition products of decaying organic matter, substances such as humic acids. The complexity of these substances requires general underpinning by first understanding simple organic substances. In this work, the radiolysis of aqueous methanol was studied.

The extended storage of spent fuel in the First Generation Magnox Storage Pond has led to various challenges concerning corrosion products, and their effects on water radiolysis. In the past, spent fuel rods were often grouped into small bundles and placed into steel skips, which were then submerged in the pond. These skips might also contain other contaminated material and the exact content of any given skip is largely unknown. Over time, much of the steel has corroded, resulting in a large build-up of what can only be described as "sludge". The exact composition of this sludge is fairly unknown, but the major constituent is iron oxide present as both red haematite (Fe_2O_3) and black magnetite (Fe_3O_4). Research involving iron oxides and radiolytic processes have mostly been focused on corrosion mechanisms; predominantly adopting an electrochemical approach with very few studies measuring chemical yields of radiolytically produced H_2 and no studies measuring H_2O_2 in the presence of iron oxide.

There are studies that have demonstrated decomposition of H_2O_2 over iron oxide in the absence of a radiation source, but as H_2O_2 is a primary product of water radiolysis, it is continuously being generated and the implications of this production are largely unknown.

Other studies involving metal oxides have also investigated radiation induced dissolution. With both these processes in mind, this project investigates some of the effects of iron oxide on the steady-state concentrations of the molecular radiolysis products, H_2 and H_2O_2.

Chapter 2: Experimental Methods

Source of Radiation and Dosimetry

This project uses cobalt-60 as a source of gamma radiation. Cobalt-60 is an artificial isotope with a half-life of 5.27 years.[2] As cobalt-60 is not a naturally occurring isotope it must be manufactured. This is normally done through neutron bombardment of the non-radioactive isotope, cobalt-59. Stainless steel control rods within a nuclear reactor core, are substituted with cobalt rods and the neutron flux present is enough to transmute cobalt-59 to cobalt-60.[20] The overall reaction for the production and decay of cobalt-60 is shown below:

$$^{59}_{27}Co + n \rightarrow {}^{60}_{27}Co \rightarrow {}^{60}_{28}Ni^{*} + e^{-} + \bar{\nu}_e + \gamma$$

The decay mechanism for cobalt-60 was similar to that of Caesium-137 in that it is initiated by beta decay. Unlike Caesium-137, however, there is no direct route to a stable isotope. Subsequently the decay of cobalt-60 follows one of two paths, both of which begin with the ejection of a beta particle. Cobalt-60 may emit two photons of gamma radiation, but will always emit at least one photon. A cobalt-60 nucleus may eject a beta particle with energy up to 1.48 MeV, this is followed by emission of a photon with energy of 1.33 MeV, however there is only a 0.12% chance that this happens. The more common decay path for cobalt-60 is to eject a beta particle with energy up to 0.31 MeV followed by the emission of two photons with energies of 1.17 MeV and 1.33 MeV.

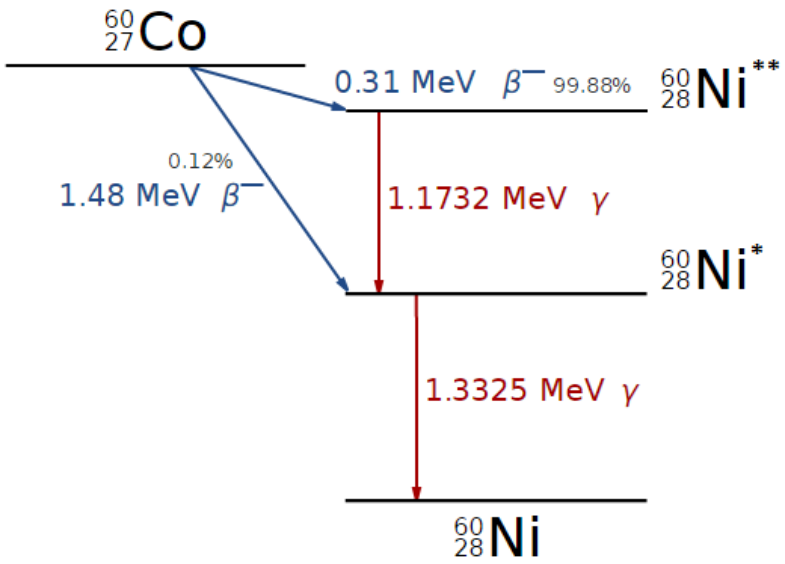

Figure 8: *A decay scheme for cobalt-60.*

Cobalt-60 is a popular source of gamma radiation used by radiation scientists. High dose rates can be achieved with fairly little material.[21] Facilities that conduct experiments using cobalt-60 as a source of radiation use a variety of systems to shield operators from radiation. Older systems can be as rudimental as a water filled hole with cobalt-60 resting at the bottom, samples are lowered in a container and held at a given distance from the source to accumulate dose. More advanced systems involve mechanically lifting cobalt-60 from some shielded well into an experimental area. This area may be a dedicated room for irradiating samples, or it may be a shielded chamber in which samples are placed. The latter example is known as a self-contained irradiator and is the type of irradiator used in this work.

All irradiations reported here were carried out using the Foss Therapy Model-812 Self-Contained Cobalt-60 Irraditor located at the University of Manchester's Dalton Cumbrian Facility (DCF). The Model-812 Irradiator contains three independent housings where cobalt-60 sources may reside, named A, B, and C. Currently only A and C contain cobalt-60 and had a total activity of 528.1 TBq on the original date of measurement (2nd May 2012). Source B is due to be filled after one half-life from the original date to bring the total activity back to a similar level. Both A and C sources are used at the same time for every irradiation throughout this work.

Figure 9: *Image on the left shows the Model-812 Irradiator. On the right is the inside of the irradiator showing the three guide rods that contain the cobalt-60 source during irradiation.*

Samples are placed within the irradiator and are exposed to gamma emission from the cobalt-60 for calculated periods of time to allow samples to accumulate the desired dose.

Radiation doses are defined as the amount of energy deposited per kilogram of sample material and are often quoted as the SI derived unit, Gray (Gy) which has the unit J kg^{-1}. In order to calculate how long a sample should be exposed for requires knowledge of the rate at which radiation energy is deposited into the sample. This is known as a dose rate and is often quoted as Gy min^{-1}. The practice of dose rate determination is known as "dosimetry" and there are a number of physical and chemical methods for determining the dose rate from a given source. Physical methods often deploy tools such as calorimeters and scintillation chambers to directly measure energy, while chemical methods depend on measuring some chemical change that occurs during exposure to radiation that responds linearly with increasing dose. There are many chemical dosimeters available depending on the kind of work being undertaken. For example, vapour phase experiments often measure the condensation of acetylene into benzene to determine a dose rate.[22] For this work the dosimeter used was a ferrous sulphate solution known as the Fricke dosimeter. The Fricke dosimeter was first described in 1927 by Hugo Fricke and has become the most adopted chemical dosimeter among radiation scientists.[23] The standard recipe to make a Fricke dosimeter used in this work is as follows:

Fricke Dosimeter: Dissolve 0.4 grams $FeSO_4 \cdot 7H_2O$ (99% assay, Fisher Chemicals), 0.06 grams NaCl (>99.99% Assay, Calbiochem), and 22 mL concentrated H_2SO_4 (95-98%, Sigma Aldrich). Dilute with distilled water to make 1 litre of Fricke solution.[24]

This solution will slowly oxidise and must be used within a few days; by preventing light from interacting with the solution, it is possible to extend the shelf life of the Fricke solution to three months. The Fricke dosimeter relies on the oxidation of Fe^{II} to Fe^{III} by species produced during the radiolysis of water.

$$H^+_{(aq)} + e^-_{(aq)} \rightarrow H^\bullet$$
$$H^\bullet + O_2 \rightarrow HO_2^\bullet$$
$$Fe^{II} + HO_2^\bullet \rightarrow Fe^{III} + HO_2^-$$
$$HO_2^- + H^+_{(aq)} \rightarrow H_2O_2$$
$$Fe^{II} + H_2O_2 \rightarrow Fe^{III} + {}^\bullet OH + OH^-$$
$$Fe^{II} + {}^\bullet OH \rightarrow Fe^{III} + OH^-$$

The extent of oxidation responds in a linear fashion to ionising radiation until dissolved oxygen is exhausted, this can be up to 500 Gy, but in practice, doses are usually kept between 40 and 400 Gy to ensure measurements are made within the range in which Fe^{III} is of a measurable concentration but Fe^{II} is not fully depleted.[2] With a strong absorbance at 304 nm, Fe^{3+} can be quantified by spectrophotometric analysis and an absorbed dose can be calculated from the following equation:

$$D_{Gy} = 9.647 \times 10^6 \times \frac{\Delta A}{\Delta \varepsilon l \rho G(Fe^{3+})}$$

where D_{Gy} is the absorbed dose in Grays, ΔA is the difference between the optical absorbance before and after irradiation, and $\Delta\varepsilon$ is difference between the molar extinction coefficient of Fe^{2+} and Fe^{3+} at 304 nm, which has an established value of 2201 mol^{-1} cm^{-1}.[2,4] $G(Fe^{3+})$ is the chemical yield of Fe^{3+} and a value of 15.5 is recommended when using cobalt-60, by the International Commission on Radiation Units and Measurements. Path length and solution density are represented by the terms l and ρ respectively.

Irradiations throughout this work were conducted using two sample holding devices, each with a number of different positions. The first device consists of a standard 4x8 test tube rack that has been fixed to an irradiation base plate. The base plate allows the device to be locked in exactly the same position within the Model-812 every time it is used.

This device holds a number of 20 mL headspace vials during irradiations of samples, which are then analysed for H_2O_2 content, the details of which will be discussed later.

The second device is somewhat more complex and is used to hold samples that are analysed for H_2 content, again the details of which are discussed later. This device is designed to keep samples mixed by slowly rotating them along a horizontal axis thus continually inverting samples throughout the irradiation period; it is hence referred to as the "inverter rig". The construction consists of a high torque motor with a top speed of 2 rpm.

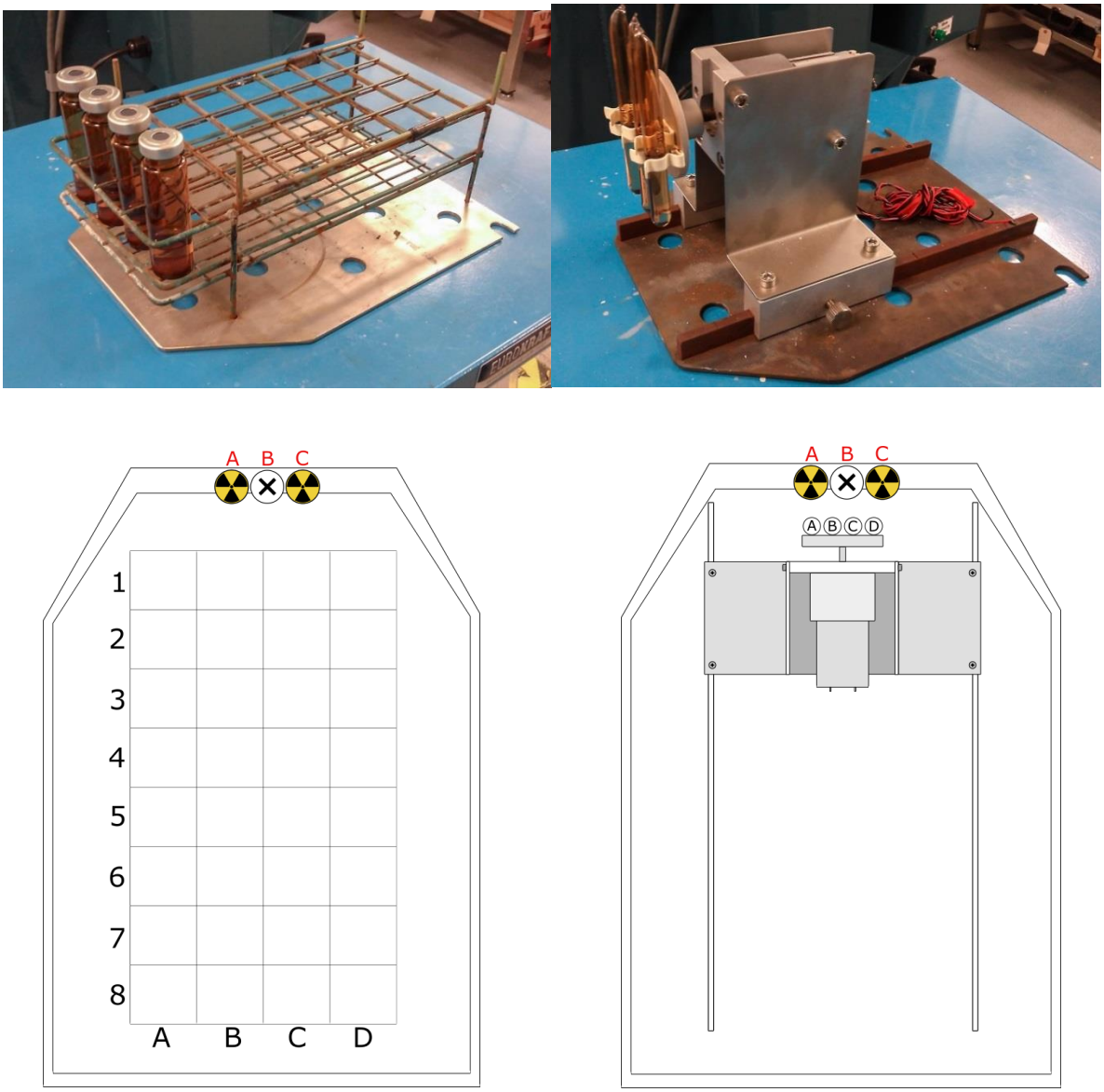

Figure 10: *Sample holding devices for use in the Model-812. Left is the 4x8 rack with its schematic below. On the right is the inverter rig, again with its schematic below.*

Dosimetry measurements were carried out in each of these devices and the results are shown below. Table 1 shows the dosimetry for the 4x8 test tube rack, each position was measured at four time intervals each of which with three replicates. Measurements were carried out in 20 mL headspace vials which were filled with 10 mL of Fricke solution.

Experiments carried out in this device only occupied positions in the first two rows, hence only these results are shown. Table 2 shows the dosimetry of the inverter rig; again each position was measured at four time intervals each with three replicates. The inverter rig only has four positions, which were measured with no rotation mixing. Initially, experiments were to be conducted under stationary conditions before moving on to mixed conditions, however time limitations prevented progression to mixed samples and all samples are conducted with no rotational mixing. From the data obtained, absorbance units were converted to an absorbed dose by use of equation 1 and dose rates are then extracted as the gradient of absorbed dose plotted as a function of time.

Date of Original Measurement: 07/02/2014		
Position	**Dose Rate on Date of Measurement (Gy min^{-1})**	**±% Error**
A1	294.35	7.5
B1	348.27	2.3
C1	323.52	4.1
D1	273.58	8.9
A2	158.45	2.4
B2	185.19	6.2
C2	181.76	2.6
D2	152.48	1.7

Table 1: *Dose rates of the front most two rows of the 4x8 irradiation rack, determined by Fricke analysis. The error indicates the percentage of uncertainty of the obtained gradient.*

Date of Original Measurement: 13/01/2015		
Position	**Dose Rate on Date of Measurement (Gy min^{-1})**	**±% Error**
A	293.79	4.6
B	317.08	4.6
C	302.08	8.7
D	306.16	4.6

Table 2: *Dose rates of the four positions of the inverter rig, determined by Fricke analysis. The error indicates the percentage of uncertainty of the obtained gradient.*

As cobalt-60 decays, dose rates are subject to change with time, however, they change in a predictable manner. The decay of cobalt-60 follows first order kinetics, it is therefore possible to adjust dose rates to account for the decay of the source simply by multiplying the dose rate by the ratio of initial radiation intensity and the intensity after a given time.[2] This can be written as:

$$DR_{Adj} = DR \times \frac{I_t}{I_0}$$

Where:

$$\frac{I_t}{I_0} = e^{-\lambda t}$$

And:

$$\lambda = \frac{\ln 2}{t_{\frac{1}{2}}}$$

DR_{Adj} is the decay adjusted dose rate after time t, λ is the decay constant and $t_{½}$ is the half-life which, for cobalt-60, is 5.27 years. The use of this equation depends on knowing how much time has passed since the original dose rate (DR) was calculated, hence the inclusion of the date on which these measurements were made in Tables 1 and 2.

Water Purification for Radiolysis Experiments

Radiation breaks water molecules into reactive radicals which can react quickly with any impurity present in a sample. It is therefore, of high importance to ensure that any water used in radiolysis experiments is of the highest purity. During the early days of radiation chemistry, high purity water was often obtained through a triple distillation process. Water was distilled firstly through standard means before being distilled again from an acid dichromate solution and finally a third time from an alkaline permanganate solution before being stored in a fused silica container.[4] Advancements in modern, self-contained purification systems have significantly simplified the process of obtaining ultra-pure water for radiolysis experiments. All experiments carried out throughout this work use ultra-pure water dispensed from the ELGA PURELAB Classic, the feed water of which is provided by the ELGA PURELAB Option-S/R 7/15. Through the use of duel bank reverse osmosis units, two independent UV lamp purifiers and deionisation cartridges, the final resistivity of output water is measured to be 18.2 $M\Omega\ cm^{-1}$.

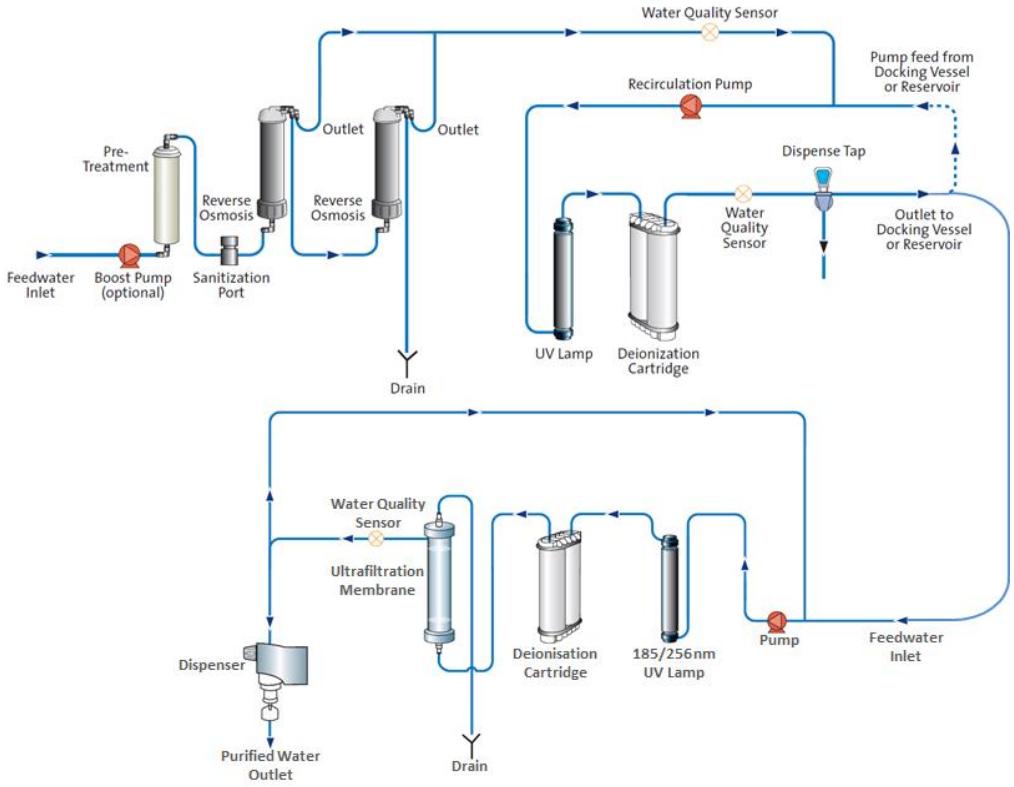

Figure 11: *A diagram of the purification system that provides the ultra-pure water used throughout this work. Image was taken from the ELGA PURELAB user manual.*

Determination of H_2O_2 – Photometric Analysis

Throughout this work, the determination of hydrogen peroxide is carried out using a photometric technique known as the Ghormley Tri-iodide method.[25] This method takes advantage of the redox reaction between hydrogen peroxide and iodide to produce iodine in a 1:1 stoichiometric ratio with hydrogen peroxide. This reaction takes place under acidic conditions and is catalysed by the presence of ammonium molybdate tetrahydrate. Acid is also required to force the resulting equilibrium between iodine and tri-iodide, completely towards the production of tri-iodide, which can then be measured by photometric analysis, this is achieved using potassium phthalate monobasic. A general reaction scheme for this is shown below.

$$H_2O_2 + 2I^- + 2H^+ \rightarrow I_2 + 2H_2O$$

$$I_2 + I^- \rightleftharpoons I_3^-$$

This is a popular method for the determination of hydrogen peroxide in radiolysis studies.[26-29] It is favoured for its relative simplicity over previous methods which typically involved complicated titrations with potassium permanganate. Furthermore, it is also extremely sensitive, enabling accurate measurements of low concentrations of hydrogen peroxide with a lower limit of 1 μM.[30]

The reagent used to reduce hydrogen peroxide is susceptible to self-oxidation and has a very short shelf life. To prevent self-oxidation and prolong the shelf life the reagent is prepared as two reagents designated "part A" and "part B" and are only mixed during analysis. One reagent contains potassium iodide under slightly alkali conditions while the other contains an organic acid salt; potassium phthalate monobasic. Both reagents are prepared according to the recipe originally described by Ghormley.[25]

Part A: Dissolve 1 gram NaOH (≥98%, Sigma Aldrich), 33 grams KI (99.5% Assay, Fisher Scientific), and 0.1 gram $(NH_4)_6Mo_7O_{24}{\cdot}4H_2O$ (≥99%, AppliChem) in 500 mL deionised water.

Part B: Dissolve 10 g $C_8H_5KO_4$ (≥99.95%, Sigma Aldrich) in 500 mL deionised water.

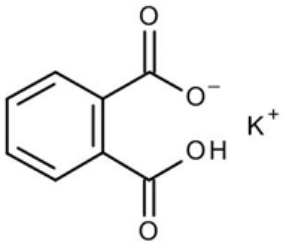

Figure 12: *Structure of Potassium phthalate monobasic ($C_8H_5KO_4$).*

Analytical Procedure

The redox reaction between H_2O_2 and I^- is carried out on a 2 mL aliquot of sample solution. To this, 1 mL of Part A and 1 mL of Part B are added; a few seconds are required for development before transfer to a quartz cuvette for analysis in a Cray 5000 UV/Vis/NIR photospectrometer. Samples that contain solid material are filtered through syringe filters before analysis to remove any solid particles. Samples of elevated pH often required additional acid to reduce the pH to the conditions required for analysis; the quantity of additional acid is determined by testing a blank sample with litmus paper, the quantity is then recorded and the dilution factor accounted for. Utilisation of the Beer-Lambert law allows for the calculation of hydrogen peroxide concentration from an absorbance within the linear range of the technique.

$$A = \varepsilon l c$$

Where A is the optical absorbance, ε is the molar extinction coefficient in M^{-1} cm^{-1}, *l* is the path length (always 1 cm during this work) and c is the concentration in mol dm^{-3}. Determination of the optimum wavelength of absorption was carried out by a scanning analysis of a 62.5 μM solution of hydrogen peroxide prepared by serial dilution of a 1 M standard, which itself, was prepared from a 3%wt. stock solution of hydrogen peroxide in water, purchased from Sigma-Aldrich.

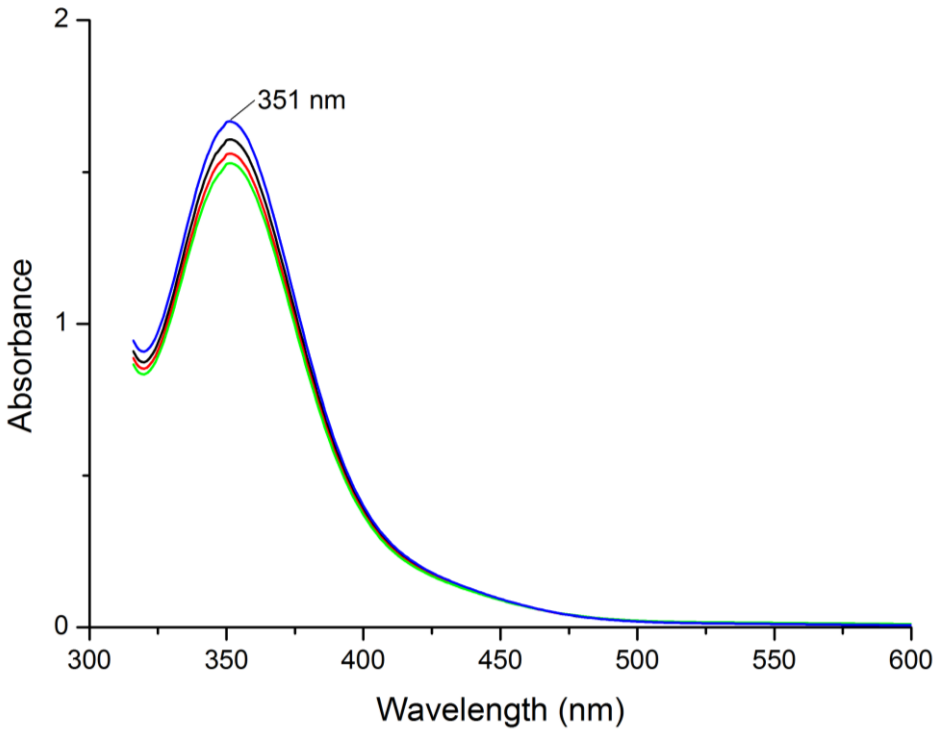

Figure 13: *Scanned absorption spectra of a 62.5 μM H_2O_2 solution.*

The maximum absorbance was determined to be 351 nm, which is consistent with values described in literature.[30,31] A series of standard solutions were made ranging in concentration from 1-300 μM to determine the molar extinction coefficient, shown in Figure 14.

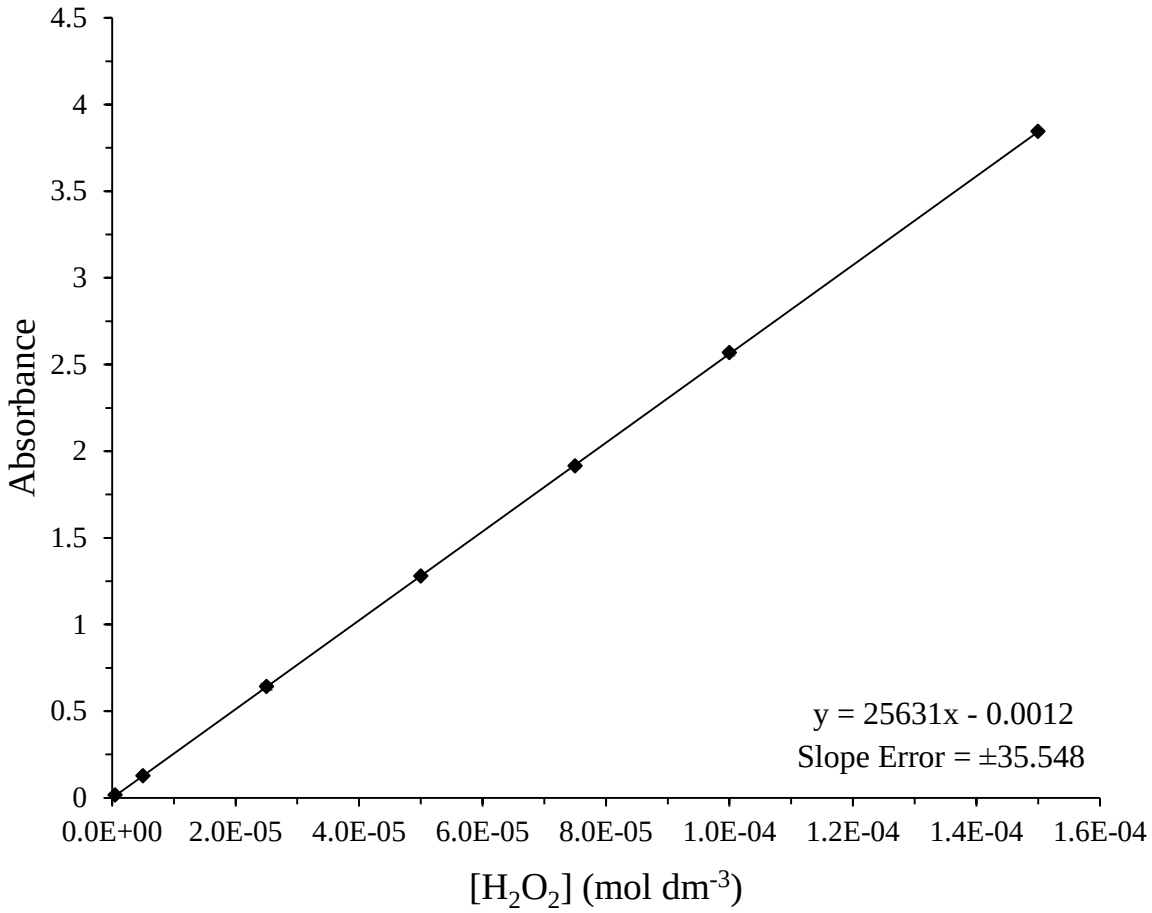

Figure 14: *A calibration curve of H_2O_2 photometric absorption to determine the molar extinction coefficient*

Addition of the tri-iodide reagents dilutes the standard to half the quoted concentration. A dilution factor of 2 is used to correct for this, hence the calibration curve covers the concentration range 0.5-150 µM hydrogen peroxide. The determined molar extinction coefficient was 25631 M^{-1} cm^{-1}; this again is consistent with values quoted in literature.[26,31,32]

Determination of H_2 - Gas Chromatography

Method development

Measurements of hydrogen gas are usually carried out using gas chromatography; frequently paired with mass spectroscopy.[33,34] This work uses only gas chromatography to measure hydrogen gas produced during the radiolysis of samples. The standard technique for gas analysis is to use a gas tight syringe and needle to extract a portion of headspace from a sealed sample. The samples are typically sealed in air tight vials with a rubber septum to allow gas extraction, however due to the effects of radiation on plastics and rubbers, the reliability of this technique remains debatable and often alternative methods are sought. One argument against the use of rubber septa in a radiation field is that they are known to radiolytically produce their own hydrogen which would contribute to any measurements. Although some preliminary laboratory tests indicate that the production of hydrogen from septa seems predictable and can be subtracted from any hydrogen produced from samples, this information was obtained from a single batch of septa and the production rate of hydrogen will most likely vary between batches as nothing is known about the manufacture's quality control tolerances. Another, important argument is concerned with the concentration ranges of hydrogen that will be measured. Aqueous samples that contain no radical scavengers often have low chemical yields for hydrogen, and sampling with a syringe reduces the sample volume to a maximum of 100 µL, attempting to extract a larger volume leads to sampling problems associated with negative pressure within the sealed sample.

The portion of hydrogen entering the gas chromatograph may be reduced even further for samples containing slurries, as much of the hydrogen may remain trapped in the aqueous phase, even after agitation.

Headspace injections may be a viable technique for samples that are known to produce large quantities of hydrogen, but generally measurements made with this technique are often close to, or below the detection limits of the gas chromatograph. Many radiation chemists have adopted a variety of techniques for measuring small quantities of radiolytically produced hydrogen that do not rely on the use of rubber septa. One such technique is the "Crush Tube" method, described in references.[35,36] This method is used for all hydrogen analysis in this work.

The Crush Tube Sampling Method

The crush tube method of gas chromatography uses a modified SRI Model 8610C Gas Chromatograph (GC) with a bespoke sampling device that contains a section of Tygon® tubing that allows for a glass sample vial to be crushed by an external force such as a pair of wrench pliers. Originally the tubing was a standard silicone tube however Tygon® tubing proved to be more durable and less prone to leaks. Figure 15 and 16 show the general schematic for the apparatus as well as the specially made sample vials for this method.

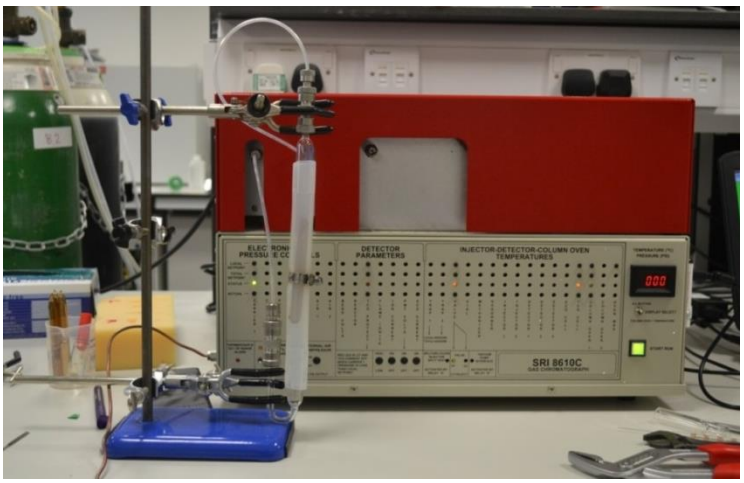

Figure 15: *The modified SRI 8610C Gas chromatograph with inline "crush tube" setup. The sample can be seen inside the silicone tubing.*

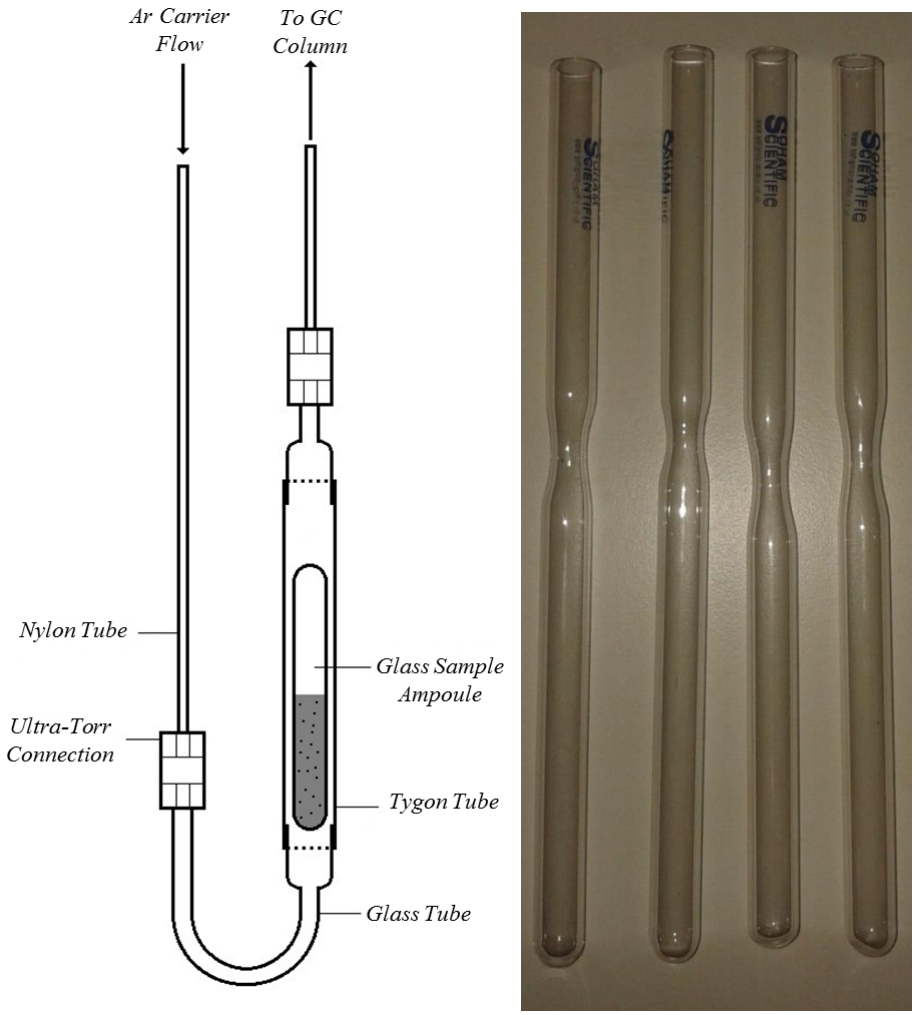

Figure 16: *Image on the left shows a schematic for the sampling apparatus, on the right are the vials used which are flame sealed at the midway neck.*

In order for this technique to work, several modifications must be made to the GC, hence the selection of the highly modular SRI Model 8610C. The first modification was made to the 10-port gas sampling valve to enable carrier gas to flow through the bespoke sampling device during analysis. The unmodified 10-port valve contains a sample loop that connects to the "IN" and "OUT" ports on the external of the GC during sample loading. When the port is rotated to the "INJECT" position, the loop is included in the carrier gas path and the external ports are isolated.

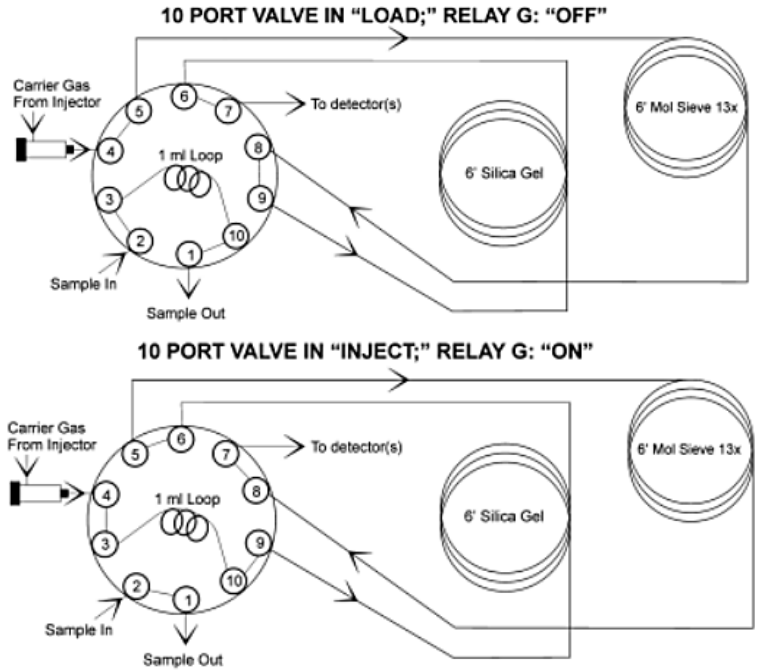

Figure 17: *A schematic of the original setup for the 10-port sampling valve in both off (top image) and on (bottom image) positions.*

It is essential that carrier gas is allowed to continually flow through the system during both sample loading and sample injecting. As the bespoke sampling device creates a closed loop between the external ports it is possible to swap the connections of ports 1 and 10 without disrupting the flow of carrier gas.

This modification isolates the external ports during sample loading but includes them during sample injection and allows sample gas to be carried through the GC.

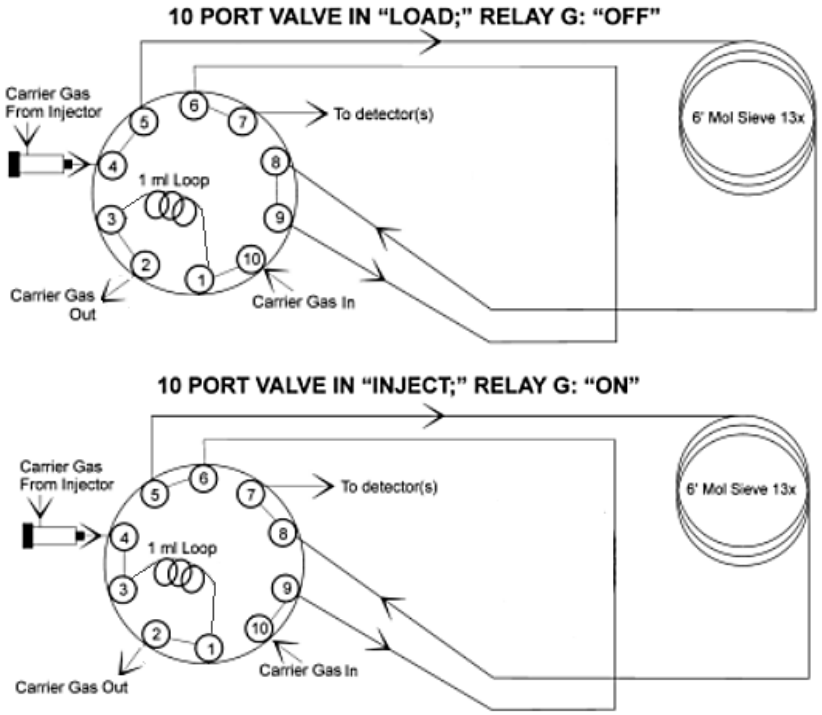

Figure 18: *A schematic for the modified 10-port sampling valve including the removal of the silica gel column.*

Figure 18 also depicts the removal of the silica gel column; this is part of the second modification. The bespoke sampling device contains a large volume of gas that requires a relatively fast carrier gas flow rate to achieve acceptably narrow peaks. This flow rate is quoted in literature as being around 50 mL/min.[35] The Packed silica gel column and the default molecular sieve column simply did not allow for this high flow rate without significant back pressure that can cause damage to equipment, for this reason they were removed. A bespoke column was made from ¼ inch copper tubing and 13x molecular sieve beads. The new column had a total length of 4 m and allowed sufficient flow rates with adequate separation of gasses.

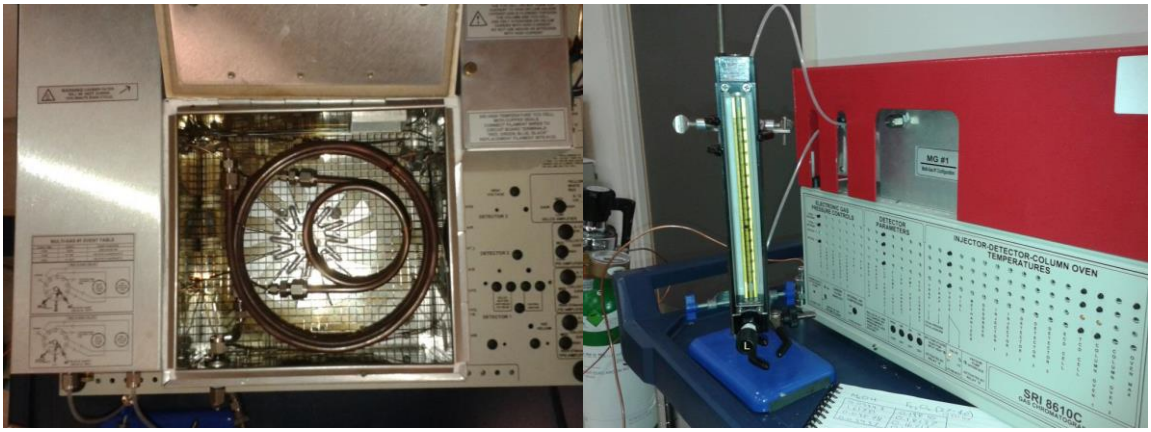

Figure 19: *Image on the left shows the bespoke ¼ inch OD 13x molecular sieve column. On the right the rotameter is connected to calibrate gas flow rates.*

The SRI Model 8610C is not equipped with a digital rotameter, as such it cannot display flow rate information, and instead can only display information about the carrier gas inlet pressure which requires a conversion formula to obtain a meaningful flow rate. The user manual includes conversion factors but these are column specific and as the column has been custom built, it is necessary to manually determine a conversion formula to obtain a flow rate. This was done using a rotameter connected to the external GC ports, by adjusting the inlet pressure and noting the rotameter value, a calibration curve was obtained.

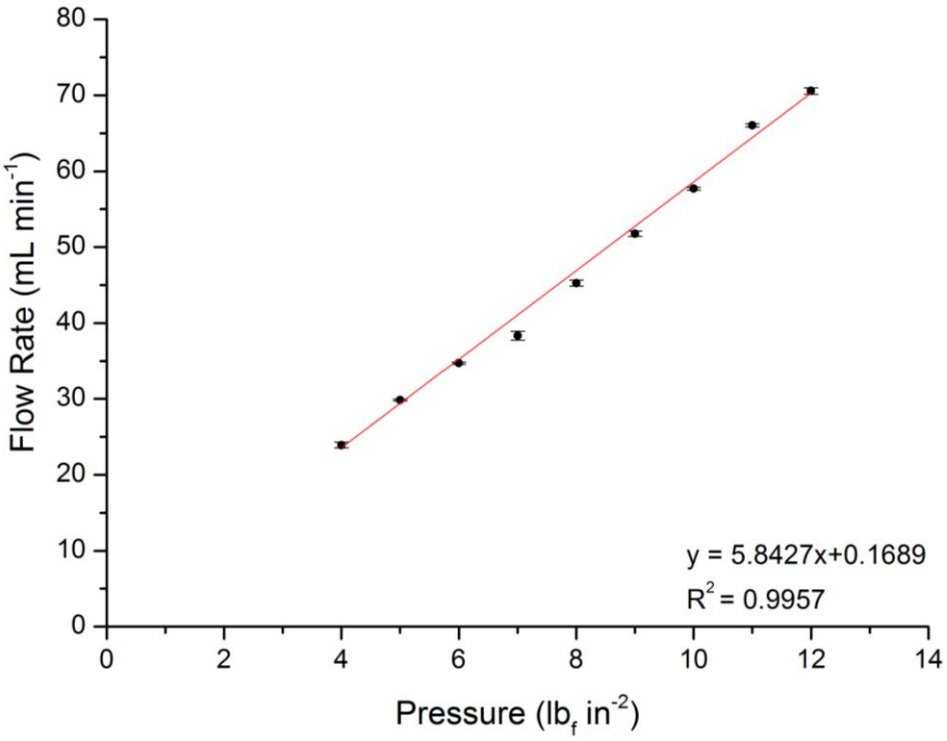

Figure 20: *A calibration curve to provide a conversion to determine carrier gas flow rate.*

Detection of H_2 and Calibration

The SRI Model 8610C is equipped with a thermal conductivity detector (TCD) for the measurement of eluted gas. The TCD consists of a Wheatstone bridge circuit with tungsten-rhenium filaments serving as resistors (Figure 21). Carrier gas containing eluted sample passes over one of the filaments while a second path is reserved for carrier gas only; to serve as a reverence. The filaments are electrically heated and the temperature of the whole unit is carefully controlled. As carrier gas passes over the filaments it conducts heat away from the filament to the detector body, when a sample component flows over the filament the conductivity changes causing the filament to change temperature relative to the reference filament. This change in temperature changes the resistivity of the filament and a change in voltage is recorded.

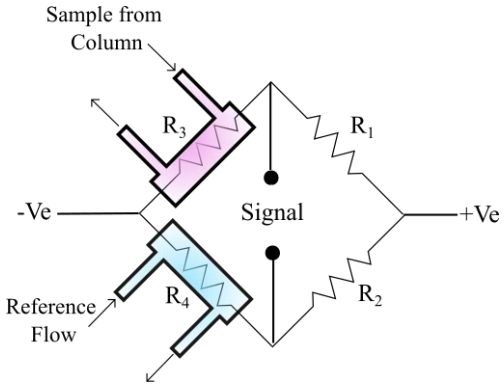

Figure 21: *A schematic of a Wheatstone bridge circuit used in the TCD.*

To achieve a good sensitivity towards a given analyte, it is important to have a large difference in thermal conductivity between said analyte and the carrier gas. Table 3 shows the thermal conductivity values for some common gases. The carrier gas most often used is helium which has a thermal conductivity of 360.36×10^{6} cal s^{-1} cm^{-1} $°C^{-1}$. As many other gases have much lower thermal conductivities, helium often performs well; however, hydrogen is a special case as it also has a high thermal conductivity of 446.32×10^{6} cal s^{-1} cm^{-1} $°C^{-1}$. For this reason, the carrier gas selected for hydrogen measurement was argon, which has a much lower thermal conductivity of 42.57×10^{6} cal s^{-1} cm^{-1} $°C^{-1}$.

Gas	**Thermal Conductivity (cal s^{-1} cm^{-1} $°C^{-1}$ $x10^{6}$) @ 26.7°C**
H_2	446.32
O_2	63.64
N_2	62.40
Ar	42.57
He	360.36

Table 3: *Thermal conductivity of commonly used gases.*
Values taken from the Handbook of Tables for Applied Engineering Science.

Measurements made by the TCD are expressed as a voltage plotted as a function of time. The peaks produced in this plot are integrated and the final result is expressed as the peak area. As the peak area unit is largely arbitrary, a calibration curve must be obtained to relate the peak area to a meaningful quantity of hydrogen. Calibration is carried out by replacing the bespoke sampling device with a simple T-section fitted with a rubber septum. Known quantities of hydrogen gas are injected into the T-section which is then carried through the GC. Figure 22 shows a calibration curve for the linear range of 1 – 500 µL of pure hydrogen at standard room temperature and pressure.

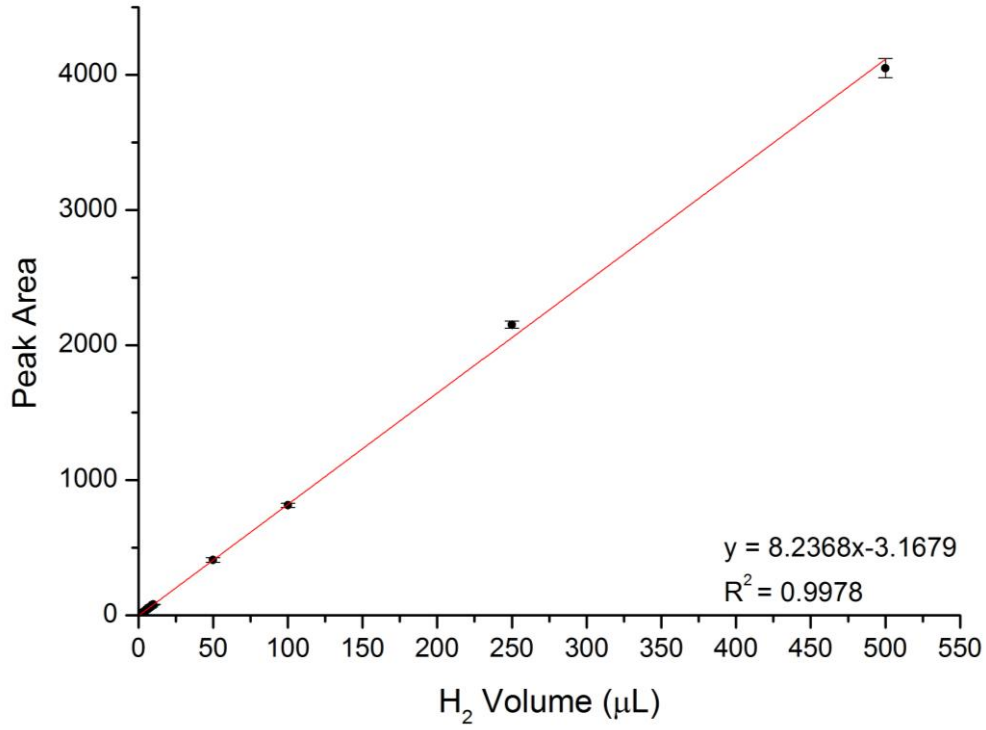

Figure 22: *A calibration curve for quantifying hydrogen gas from chromatograms*

Samples of air/hydrogen mixtures were also injected to make sure there was adequate separation between the gases; good separation between hydrogen and oxygen is observed, but the separation of oxygen and nitrogen is not adequate for analysis of those gases when both are present in large quantities.

Machine parameters were adjusted for optimum performance; these are shown in Table 4. These parameters were used for every experiment throughout this work.

Parameter	Value
Valve Temperature	70 C°
Column Temperature	40 C°
TCD Temperature	220 C°
Flow Rate	50 mL/min
Carrier Gas	Ar

Table 4: *Optimised parameters used for the analysis of H_2 gas.*

Method Validation

It was mentioned previously that the bromide ion is an excellent scavenger of hydroxyl radicals during radiolysis.

$$^{\bullet}OH + Br^- \rightleftharpoons [HOBr]^- \xrightarrow{H^+_{(aq)}} Br^{\bullet} + H_2O \xrightarrow{Br^-} Br_2^{\bullet -}$$

Radiolysis of an aqueous solution of 1 mM bromide results in the elimination of the reaction between the hydroxyl radical and molecular hydrogen in solution.[37] Other than diffusion to the gas phase, a reaction with hydroxyl radicals is the only significant removal path of hydrogen at neutral pH. The removal of dissolved oxygen by argon sparging also simplifies much of the radiolysis chemistry, allowing for a more reproducible experiment. This means that the hydrogen measured from the radiolysis of a deaerated, 1 mM bromide solution is in fact a primary yield and is quoted throughout the literature as being $G_{H_2} = 0.45$; this is an average value from a range of studies.[2,4,5,38,39]

In order to secure confidence in this technique, a validation experiment was carried out in which a 1 mM solution of potassium bromide was used to determine the primary yield of hydrogen which was then compared to the literature value.

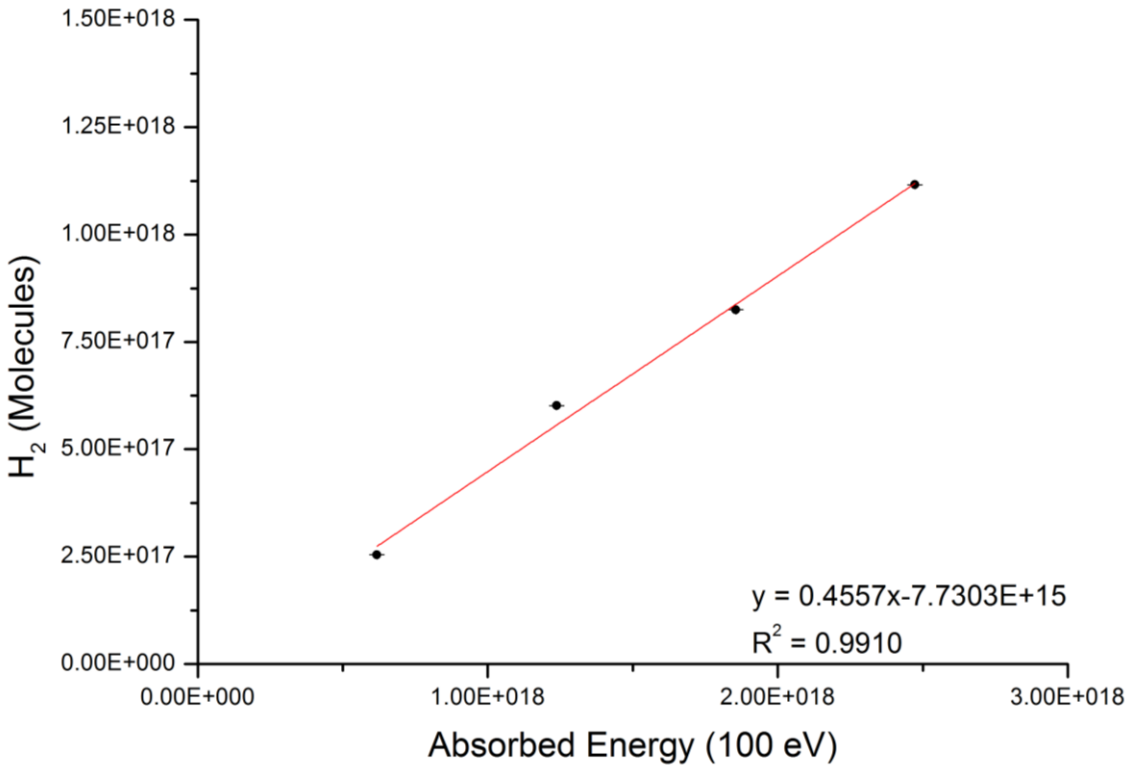

Figure 23: *Method validation by the determination of the well-established primary yield of H_2 through hydroxyl scavenging by bromide.*

As expected, the hydrogen concentration increased linearly with absorbed dose over the experimental range. When the number of hydrogen molecules is plotted as a function of absorbed energy in sets of 100 eV, the gradient gives G_{H_2} = 0.456 ±0.025, matching well to the average value quoted in literature.

Sources of Error

The majority of experiments carried out in this work use the absorbed energy, or dose, as the independent variable and, using one of the analytic techniques discussed above, either a photometric absorption value or the integrated response to hydrogen gas detection, as the dependant variable. Both the dependant and independent variable have errors associated with them which are discussed below.

Determining the quantity of absorbed energy to the sample relies on the procedure of dosimetry, discussed earlier in this chapter. The errors reported in Tables 1 and 2 are the percent error of the gradient obtained from the measurement of Fe^{3+} as a function of time. As the experiments carried out in this work are plotted as a function absorbed dose, and there is an element of uncertainty associated with the dose rates, the uncertainty of the calculated absorbed dose increases with increasing dose. This uncertainty in the absorbed dose is included in many of graphs showing experimental data and is represented by horizontal error bars.

Sources of Error in the Determination of H_2O_2

The determination of H_2O_2 relies mainly on the calibration curve to yield a molar extinction coefficient, determined to be 25631 M^{-1} cm^{-1} with an uncertainty of ± 35.5 M^{-1} cm^{-1}. The molar extinction coefficient is used to convert the measured absorbance of a sample to a concentration of H_2O_2, however, this value has a dependence on temperature. The ambient temperature of the laboratory fluctuates slightly, but it was decided that the effects were too minor to consider. The irradiation of samples, on the other hand, resulted in samples heating slightly, to a temperature that would be significant.

This was largely mitigated by leaving samples to cool for a few minutes until they reached room temperature, however, an increase in temperature may affect the radiation chemistry.

Solutions used to calibrate, and reagents used to analyse samples, also carry an associated uncertainty in their concentrations. The standards used to produce the calibration curve were prepared from a stock solution of 3 % wt. H_2O_2 (Sigma Aldrich). From this, the 0.882 M solution was diluted to 1 mM which was used in a serial dilution to create the standards ranging from 1 – 300 μM. Uncertainty in the concentrations will have been introduced by the tolerances of the pipettes and volumetric flasks used. The pipettes used were the Gilson Pipetman P1000 and P20 which are certified to comply with ISO 8655 that imposes maximum allowable systematic errors of ± 8.0 μL and ± 0.2 μL for the P1000 and P20, respectively. The maximum allowable random error for the P1000 is quoted to be ≤ 3.0 μL and ≤ 0.1 μL for the P20. The volumetric flasks used were class A Glassco brand flask that conform to ISO 1042. Of the range of flasks used, the largest error was 0.0025 %.

Any uncertainty in the concentrations of the analytical reagents used to reduce H_2O_2 is largely irrelevant as the chemicals used to perform the analysis are provided in a large excess. Stoichiometrically speaking, as long as the concentration of iodide is at least three times that of H_2O_2, the analysis should work, in reality the concentration of iodide is several times higher than this, ensuring all H_2O_2 is reduced. The sum of the above errors are assumed to contribute to less than 1% of the total uncertainty of any measurements of H_2O_2.

Sources of Error in the Determination of H_2

The experimental technique provides a means to quantify hydrogen gas by volume. In order to make a comparison to predictions made by the computational model it was necessary to convert this value to a concentration (mol dm^{-3}). This means knowing the volume of the headspace in the crush tube vials. As these vials are flame sealed, they naturally have an irregular shape and calculating a precise volume is difficult, for this reason the conversion uses an estimated headspace volume of 2 mL.

Hydrogen gas is quantified by the integration of a change in voltage with respects to time; however the voltage response measured can be affected by a number of factors. Factors such as temperature and pressure are controlled automatically by the machine. Moisture can also affect the response of the TCD and this is controlled by running a "bake out" cycle prior to running any analysis. One factor that cannot be prevented is the slow oxidation of the tungsten-ruthenium filament which lowers the sensitivity of gas detection. This can be accounted for by performing regular calibrations, often 3 or 4 point calibrations that are compared to the original calibration curve. If there is any deviance from the original curve then a full calibration is performed and this is then used for the following analyses. The calibration curve shown in Figure 22 was the first full calibration performed, throughout the duration of this project the gradient of this curve gradually decreased, this was accounted for using the calibration process mentioned above. As calibrations are performed by hand with a gas tight syringe, most of the error is likely introduced at this point. The average error of calibration points was ± 2.5% in the calibration curve given in Figure 22, for other calibrations not shown in this work the average error was always less than 5%.

Chapter 3: Computational Methodology

The earliest recorded computational approaches to solving problems in the field of radiation chemistry date back to 1958, when the AVIDAC computer in Chicago was used to model radical diffusion kinetics.[40] Since then, different mathematical techniques have found use in modelling problems found in the field of radiation chemistry and with ever increasing computational power, complicated calculations can be performed in seconds rather than days. In the early days of computational radiation chemistry, primary yields were calculated by deterministic methods involving the diffusion of a single spur. However, it became apparent that a Monte Carlo approach held several advantages over deterministic methods for the description of early stage radiolysis. Such advantages include the ability to incorporate the effects of a variety of different spur sizes and other entities arising from secondary electrons.[41] For this reason, modern radiolysis models usually fall into two categories, depending on what stage of radiolysis is being modelled. Monte Carlo calculations often concern the non-homogeneous, early stages of radiolysis due to the stochastic nature of energy deposition into a medium; as mentioned earlier these calculations often predict the primary yields of radiolysis products.[42] If the primary yields are already known, a deterministic approach is often employed to model the resulting homogeneous chemistry in a similar way to most other chemical kinetics models; through the use of simultaneous ordinary differential equations (ODE).[27,43-46] Newer radiolysis models are moving towards a multi-scale approach in which the output of the stochastic stage is fed directly into the deterministic stage.[47]

In this project, a deterministic kinetic model for homogeneous chemical stage radiolysis has been developed using a software package called FACSIMILE, developed by MCPA software Ltd.

FACSIMILE utilises Gear methodology for auto-adaptive time step control, coupled with Newton-Raphson iterations for prediction correction, to deliver a robust simultaneous ordinary differential equation solver. The FACSIMILE language is largely based on the Fortran language, but is tailored for use by the scientific community and includes its own high level notations for simplifying ODE construction.[48] The chemical model developed here is largely based on the rate coefficient compilation by Elliot and Bartels, [46] as well as other literature sources.[27,43,45,49]

This chapter gives a detailed description of how the model in this project works. In essence the model functions by producing primary radiolysis species at rates determined by their primary yields and a dose rate parameter, while simultaneously solving a set of ODEs that represent the chemical reactions that describe the radiolysis chemistry. At the same time, the model is also bound by framework calculations that describe various physical parameters including, but not limited to, temperature effects and species volatility. Each of these concepts is described in detail in the following sections, as well as the core radiolysis reaction set.

Production of Primary Species

As this model is only concerned with the homogeneous radiolysis chemistry that occurs after diffusion of the primary species away from any kind of track structure, the effect of radiation can be represented by a series of zero order production equations with rate constants derived from the dose rate and the species primary yield. Each primary radiolysis species has its own equation that defines its rate of production; the general form of this equation is shown below.

$$k_i = \frac{D_R \times E_C \times \rho \times G_i}{N_A}$$

D_R is the dose rate given in Gy min^{-1} and G_i is the primary yield for species *i*. N_A is Avogadro's number and provides the conversion of molecules to moles, while ρ is the density of water and converts mass to volume; ρ also has its own temperature dependency which is calculated elsewhere in the code. E_C is a constant that effectively converts the units of dose rate (J kg^{-1} min^{-1}) into time units compatible with a zero order rate constant (mol dm^{-3} s^{-1}) and energy units compatible with primary yields (molecules 100 eV^{-1}) and has a value of 1.04×10^{15} and carries the unit 100 eV s^{-1}.

The dose rate is initially set by the user and is constant throughout the calculation; however, primary yields are not set by the user and are initially set depending on other parameters such as temperature and pH. Table 5[2] shows the primary yields for water radiolysis by gamma-rays at neutral pH and at room temperature, the following section describes the factors that can alter these values and details how they are incorporated into the model.

Primary Species	e_{aq}^-	$H^\bullet$	$^\bullet OH$	H_2	H_2O_2
g-Value	2.63	0.55	2.72	0.45	0.68

Table 5: *Primary yields for γ-radiolysis of water at neutral pH and standard pressure and temperature.*[2]

Factors Affecting Primary Yields

Temperature

The rate of diffusion of primary species away from spurs created by ionising radiation is affected by temperature. As the temperature is increased, the rate of diffusion of radical species increases, as does the rate of recombination reactions. The yields obtained at high temperature are determined by this competition between diffusion and recombination rates. Experiments carried out by Hochanadel and Ghormley (Table 6)[50] first show this effect over a temperature range of 2 – 65 °C in which higher temperatures favour increased radical yields and decreased molecular yields.

Primary Species	g-Value			Temperature coefficient, % °C^{-1}
	2°C	23°C	65°C	
$H^{\bullet} + e_{aq}^{-}$	3.59	3.67	3.82	+0.10±0.03
$^{\bullet}OH$	2.80	2.91	3.13	+0.18±0.04
H_2	0.38	0.37	0.36	-0.06±0.03
H_2O_2	0.78	0.75	0.70	-0.15±0.03
$-H_2O$	4.35	4.41	4.54	+0.07±0.03

Table 6: *Temperature effects on the primary yields of water radiolysis.*[50]

A recent extensive compilation by Elliot and Bartels, includes measurements of primary yields at temperatures from 20 – 350°C from multiple sources and collates this data to provide fitted equations for use in computational models. The primary yield of the hydrated electron was determined by product analysis of nitrogen formation from samples containing nitrous oxide.[51-54] The chemical yield of nitrogen is equal to the primary yield of the hydrated electron due to the following scavenging reaction.

$$e^{-}_{(aq)} + N_2O \rightarrow N_2O^{-} \rightarrow N_2 + O^{-}$$

Organic compounds were also added to scavenge hydroxyl radicals and prevent them from reacting with hydrated electrons. Pulse radiolysis studies were also included[55] but only the data from nitrogen yield measurements were recommended for use.

For the determination of the hydroxyl primary yield, pulse radiolysis was the primary method used. The method described used bicarbonate to effectively convert hydroxyl radicals to the carbonate radical, which is more easily measured.

The temperature dependency of the extinction coefficient for the carbonate radical was estimated by integrating normalised absorption spectra as a function of temperature, originally collected by Elliot *et al*.[53] The resulting temperature dependency of the hydroxyl radical primary yield is in agreement with an independent pulse radiolysis study that used a ferrocyanide ion solution to measure the temperature dependency of the hydroxyl yield, up to 105°C.[53]

The temperature dependence of the hydrogen peroxide primary yield was determined by three independent studies. Measurements in acrylamide solutions provided the temperature dependency up to 100°C.[53] Further measurements made in deaerated solutions containing nitrate and methanol extended this range to 150°C.[56] Estimations of the peroxide primary yield to high temperatures were made based on the assumption that it was equivalent to the chemical yield of oxygen in an alkali solution containing nitrous oxide or iodine; this approach expanded the temperature range to 270°C.[54]

The primary yield of molecular hydrogen as a function of temperature has been measured by three laboratories. In each case, hydrogen was directly measured from solutions containing either, a nitrous oxide and organic mix, or nitrite ions. In both cases, the measurements agreed well across all three laboratories.[51,53,54]

Several attempts at measuring the primary yield of the hydrogen atom as a function of temperature have been made, however only two data sets are considered reliable, as others do not agree with the established yield at room temperature; although all data sets show an increase in yield with temperature.

The chemical yield of molecular hydrogen from deaerated solutions containing nitrate and phosphite ions is said to be equal to the sum of the primary yields of molecular hydrogen and the hydrogen atom; subtracting the already established primary yield of molecular hydrogen from these measurements should give the primary yield of the hydrogen atom. These measurements agreed well with the established room temperature value and gave a temperature dependence up to 200°C.[53] The temperature dependence was expanded to 350°C based on estimations of the ratio between the hydrogen atom primary yield and hydrated electron primary yield which was calculated from data obtained during other experiments performed in alkali solutions. Unfortunately, this data is described as archived and unpublished. The collated data from the experiments described above are shown in Figure 24 with polynomial fits overlain, the equations for these polynomials are given in Table 7, and are used in the modelling calculations reported.

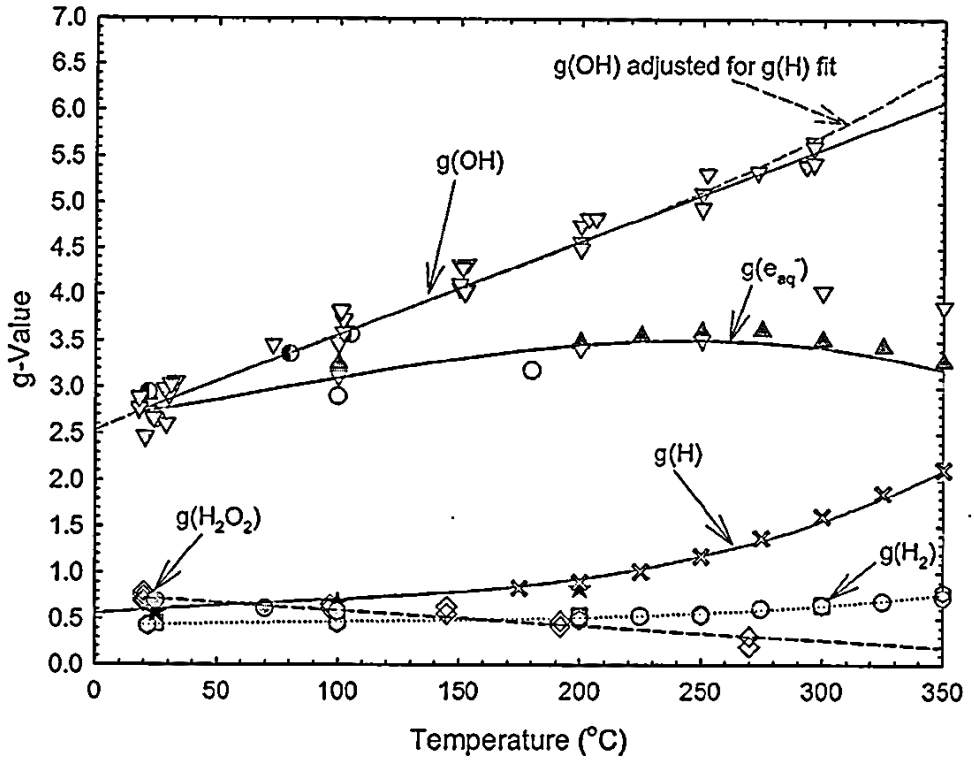

Figure 24: *Collected data from literature showing measured primary yields as a function of temperature. Provided by Elliot and Bartels 2008*[45]

Primary Yield	Polynomial
$g(e_{aq}^-)$	$2.641 + 4.162\times10^{-3}\,t + 9.093\times10^{-6}\,t^2 - 4.717\times10^{-8}\,t^3$
$g(H_2O_2)$	$0.752 - 1.620\times10^{-3}\,t$
$g(H_2)$	$0.419 + 8.721\times10^{-4}\,t - 4.971\times10^{-6}\,t^2 + 1.503\times10^{-8}\,t^3$
$g(^{\bullet}OH)$	$2.531 + 1.134\times10^{-2}\,t - 1.269\times10^{-5}\,t^2 + 3.513\times10^{-8}\,t^3$
$g(H^{\bullet})$	$0.556 + 2.198\times10^{-3}\,t - 1.184\times10^{-5}\,t^2 + 5.223\times10^{-8}\,t^3$

Table 7: *Polynomial equations for estimating temperature effects on primary yields.*[45] *Where t is the temperature in °C*

Incorporation of any kind of temperature dependence into a prediction that will be compared with experimental data requires knowledge of the experimental temperature. This is especially important in chemical kinetic models such as this, as almost all the reaction rate constants are temperature dependent. For this reason, a test was conducted to measure the temperatures experienced by samples during irradiation.

The test was carried out with vials which had thermocouples attached, the vials were filled with water. The vials were irradiated for 16 hours and the temperature was recorded every 5 minutes, the average recording is shown in Figure 25. A polynomial fit was made from the first 4 hours of data which was applied in the code to control the rate of temperature change during a calculation; the simulated temperature is shown as the red dashed line in Figure 25.

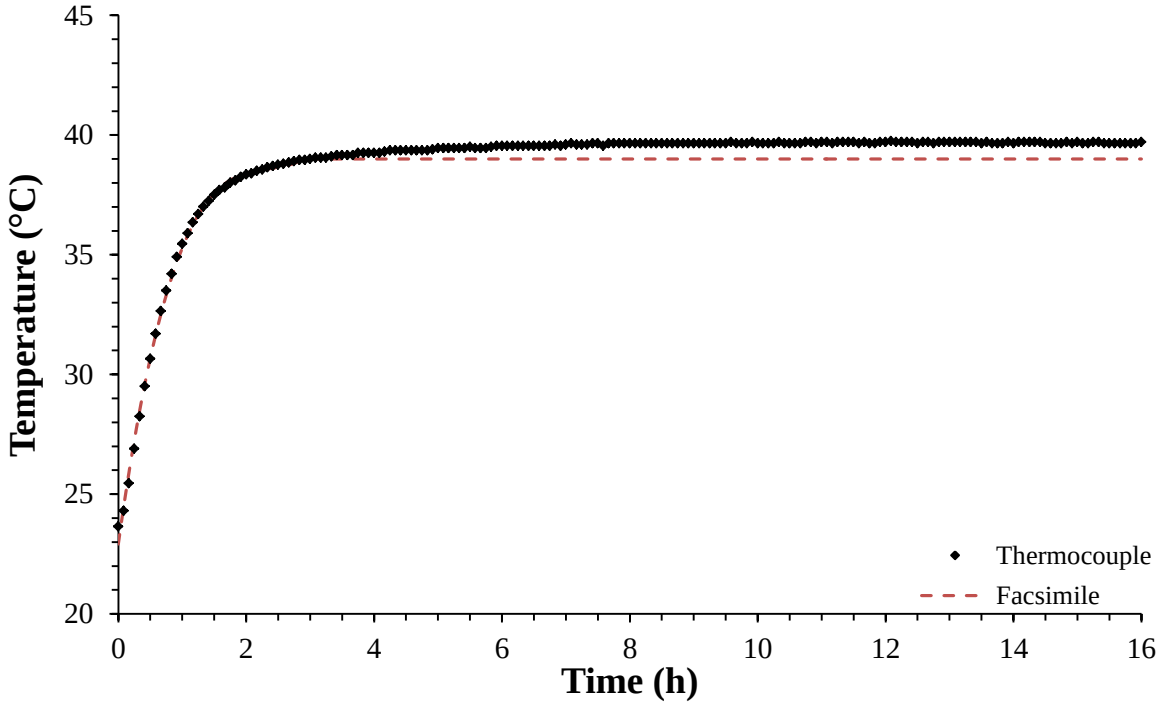

Figure 25: *A comparison of the sample temperature profile logged by thermocouple, to the temperature profile calculated in the computational model.*

There are many "bulk" radiolysis models in literature, few of which make any reference to the way in which temperature is controlled. It can only be assumed that these models use a fixed temperature, which would produce less accurate predictions, especially during early periods where the temperature change is significant. It should be said that this approach should be used with caution as this temperature profile depends on the equipment being used to irradiate samples and the dose rate involved.

The majority of energy from the radioactive sources ends up being deposited into the shielding material of the irradiation unit. This heats the surrounding air within the irradiation chamber, which is often not circulated.

pH

The effect of pH on the primary yields of water radiolysis has been a subject of discussion for many decades, yet experimental data on the subject is relatively sparse at high and low pH. Early radiolysis experiments often took place in acidic medium and so acidity became one of the first variables considered for investigations into the effects of pH on primary yields. Table 8[57] shows primary yields data from 0.4 M sulfuric acid samples where the pH = 0.46; the values shown are averages over multiple sources.

Reference	$g(e_{aq}^-) + g(H^\bullet)$	**$g(^\bullet OH)$**	**$g(H_2)$**	**$g(H_2O_2)$**	**$g(-H_2O)$**	**Ref #**
Ferradini C. *et al*	3.70	2.80	0.45	0.90	4.60	58
Allen A.O, Lefort M.	3.65	2.95	0.45	0.80	4.55	4,59
Sworski T. J.	3.70	2.92	0.39	0.78	4.48	60
Hochanadel C. J. *et al*	3.70	2.90	0.40	0.80	4.50	61
Mahlman H. A. *et al*	3.68	2.96	0.45	0.81	4.58	62
Hayon E. *et al*	3.66	2.97	0.40	0.76	4.50	63,64
Sehested K. *et al*	3.62	2.89	0.39	0.76	4.41	65
Spinks & Wood	3.65	2.90	0.40	0.78	4.45	2

Table 8: *A collection of measurements of primary yields made in 0.4 M solution of sulphuric acid (pH = 0.46).*[57]

The noticeable changes to the primary yields, when compared with those at neutral pH, are consistent throughout the literature, including further sources not included in Table 8.

The change in primary yields is not massive in the pH range 0.46 – 7, but neither is it insignificant. With the exception of the molecular hydrogen yield, all primary yields increase slightly at low pH. The main explanation for this involves the conversion of hydrated electrons to hydrogen atoms within the radiation spurs. In neutral solutions the hydrated electron readily reacts with the hydroxyl radical to form hydroxide, but when the hydrated electrons are converted to hydrogen atoms, the reaction with hydroxyl radicals is suppressed.

The hydrogen atoms do not react with hydroxyl radicals as quickly as hydrated electrons and so the hydroxyl radicals become effectively "protected" at low pH. This explains the increase in primary yield of the reducing species (hydrated electron plus the hydrogen atom) and the increase in the hydroxyl radical yield. With an increase in hydroxyl radicals comes an increase in the peroxide primary yield via the dimerisation of hydroxyl radicals. The decrease of the molecular hydrogen primary yield is due to the dimerisation of hydrogen atoms having a slower coefficient than the reaction between two hydrated electrons.

$$e^-_{aq} + H^+_{(aq)} \rightarrow H^\bullet \qquad k = 2.10 \times 10^{10}\ M^{-1}\ s^{-1}$$

$$e^-_{aq} + {}^\bullet OH \rightarrow OH^- \qquad k = 3.02 \times 10^{10}\ M^{-1}\ s^{-1}$$

$$H^\bullet + {}^\bullet OH \rightarrow H_2O \qquad k = 1.53 \times 10^{10}\ M^{-1}\ s^{-1}$$

The effect high pH has on the primary radiolysis yields of water is not as well documented. The number of studies is fewer than those conducted in acidic medium and the data from said studies do not always agree. Table 9[57] shows a collection of primary yields measured in alkali samples where the pH ≈ 13.5.

Reference	$g(e_{aq}^-)$ + $g(H^\bullet)$	$g(^\bullet OH)$ + $g(^\bullet O^-)$	$g(H_2)$	$g(H_2O_2)$ + $g(HO_2^-)$	$g(-H_2O)$	Ref #
Draganić *et al*	**3.18**	2.72	0.45	0.68	4.09	5,38
Hayon E.	**3.27**	3.04	0.43	0.53	4.12	66
Haissinsky M.	**3.34**	3.01	0.4	0.56	4.14	67
Dainton F. S. *et al*	**3.85**	3.4	0.36	0.58	4.57	68,69
Cheek C. H. *et al*	**2.8**	2.1	0.45	0.84	3.7	70
Fielden E. M. *et al*	**3.57**	2.8	-	-	-	71
Czapski G. *et al*	**3.3**	-	-	0.56	-	72

Table 9: *A collection of primary yields measured in alkali solutions (pH ≈ 13.5).*[57]

At high pH, the hydroxide ion can react with the hydroxyl radical within the spur, forming the oxide radical anion $^\bullet O^-$ in the following equilibrium.

$$^\bullet OH + OH^- \rightleftharpoons {}^\bullet O^- + H_2O \qquad pK_a = 11.9$$

At high concentrations of hydroxide, the hydroxyl radical may be completely replaced by the oxide radical anion. A consequence of this shift is the decrease in the peroxide primary yield, as it is thought that the dimerisation of the oxide radical anion to form peroxide is slower than the neutral equivalent dimerisation of hydroxyl radicals. This is something that is observed across almost all the studies conducted at high pH. The reaction between the hydrated electron and the oxide radical anion is also slower than the corresponding neutral equivalent reaction. It is, therefore, expected that the primary yield of oxidising radicals, $G(^\bullet OH) + G(^\bullet O^-)$ would increase with increasing pH, as would the total primary yield of reducing radicals, $G(e^-_{(aq)}) + G(^\bullet H)$. The primary yield of molecular hydrogen is mostly unaffected by the increased pH; this would suggest that the net decomposition yield of water must increase in order to satisfy the material balance equation.

$$g(-H_2O) = g(e_{aq}^-) + g(H^\bullet) + 2g(H_2) = g(OH^\bullet) + g(O^{\bullet-}) + 2(g(H_2O_2) + g(HO_2^-))$$

Despite the difficulty in deriving quantitative agreement across the available data, there are studies that offer qualitative agreement with the expected changes to primary yields at high pH.[66-69] There are also studies that do not agree, and propose that the primary yields are largely unaffected by pH.[5,38,70,73]

Despite the oxide radical anion being the main radiation produced oxidising radical in aqueous alkali medium and therefore having a significant effect on the chemistry, reaction rate coefficients associated with it are largely unknown and rely on estimation. The lack of reliable rate coefficients for the reactions of the oxide radical anion is an important factor to consider when attempting to model the radiolysis of water at high pH.

It has been shown, using stochastic simulations, that the chemistry of the oxide radical anion can have a significant impact on the prediction of primary yields. Initial predictions of the stochastic model by Pimblott *et al.*[74] showed an increase in the peroxide primary yield at high pH. This is counter to the accepted trend observed experimentally of a decreasing peroxide primary yields at high pH. In order to match the observed decrease in peroxide primary yield, a single rate constant was changed from 2.0×10^{10} M^{-1} s^{-1} to 6.5×10^{9} M^{-1} s^{-1} for the reaction below.

$$O^{\bullet-} + {}^\bullet OH \rightarrow HO_2^-$$

This change had the effect of reversing the trends of the primary yield predictions at high pH, resulting in agreement with experimental data. Soon after this, the rate constant for the reaction between the oxide radical anion and the hydroxyl radical was measured to be 7.4 $\times 10^9$ M^{-1} s^{-1}, which is much closer to the adjusted rate constant used in the stochastic simulation than the original estimate.[49]

Figure 26 shows literature values for the measured primary yields as a function of pH, from this, polynomial equations were fitted which were combined in a multiple regression analysis with the equations fitted to temperature analysis data. Table 10 shows the resulting equations. While this approach gives an estimate of the primary yields as a function of both temperature and pH, it is not an ideal solution. This type of estimation is better suited to a stochastic type track chemistry calculation.

A stochastic approach could also account for the effects of different linear energy transfer (LET) values, which are discussed in the next section. A multi-scale approach could even procedurally produce stochastically calculated primary yields that feed into a deterministic chemical kinetic simulation.

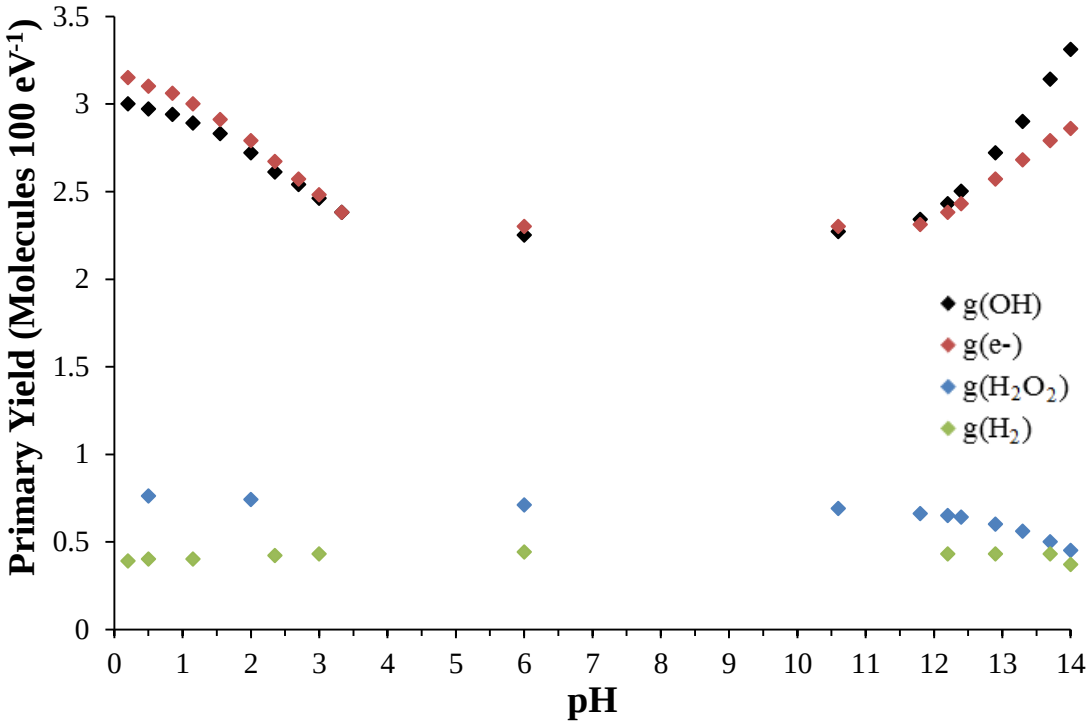

Figure 26: *A reproduction of data provided by Hayon[75] showing the effect of pH on primary radiolysis yields.*

Primary Yield	Multiple Regression Equation
$g(e_{aq}^-)$	$2.8 + 2.85\times10^{-3} \times t - 2.51\times10^{-2} \times pH$
$g(H_2O_2)$	$8.45\times10^{-1} - 1.51\times10^{-3} \times t - 1.7\times10^{-2} \times pH$
$g(H_2)$	$3.88\times10^{-1} + 8.29\times10^{-4} \times t + 5.99\times10^{-4} \times pH$
$g(^{\cdot}OH)$	$2.43 + 1.11\times10^{-2} \times t - 1.2\times10^{-3} \times pH$
$g(H^{\cdot})$	$4.44\times10^{-1} + 3.67\times10^{-3} \times t - 2.4\times10^{-4} \times pH$

Table 10: *Multiple regression polynomials used to estimate the combined effect of temperature and pH on the primary yields of water radiolysis.*

Linear Energy Transfer (LET)

Linear energy transfer is a way of expressing the rate at which an ionising particle loses energy through a medium. Sometimes referred to as "stopping power", linear energy transfer is quoted as the average energy loss divided by a fixed path length, usually micro meters or nano meters (keV μm^{-1} or eV nm^{-1}). This parameter is frequently expressed as an average rate of energy loss across the entire particle's track; this is because the energy loss rate of an ionising particle is not uniform. As a high energy ionising particle begins its journey through a material, energy loss events are sparse and only small quantities of energy are transferred so the particle continues largely un-deflected. As this energy lost to these small transfers accumulates, and the energy of the charged particle decreases, the cross section of interactions increases. This means that there are more energy loss events for a given linear distance as the particles path becomes less linear. A true linear energy transfer profile of a particle would take the form of a Bragg curve, such as the example shown below.

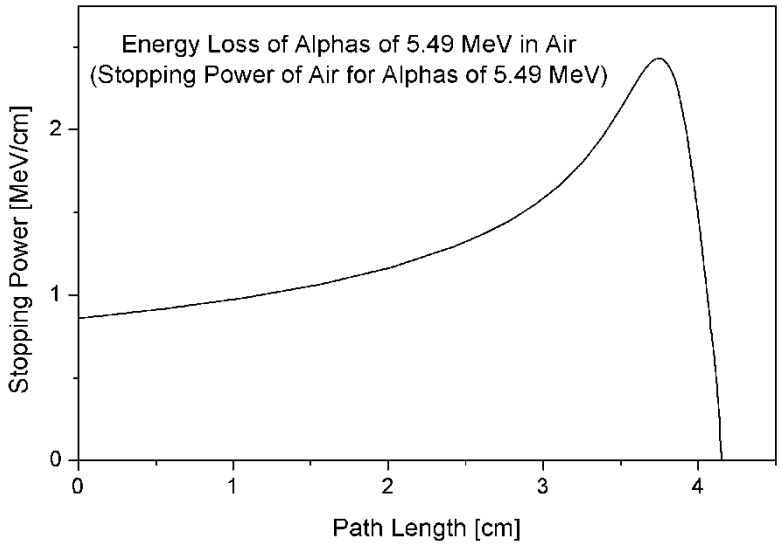

Figure 27: *An example of a Bragg peak. Energy loss of alphas of 5.49 MeV in Air. Image released to public domain.*

For ease of comparison this profile is usually averaged to give a single LET parameter. Ionising particles of higher mass and/or lower energy have higher LET values. The implications of linear energy transfer are manifested in the radiation track structure. Increasing LET values have the effect of increasing the spur distribution density as illustrated in the diagram below.

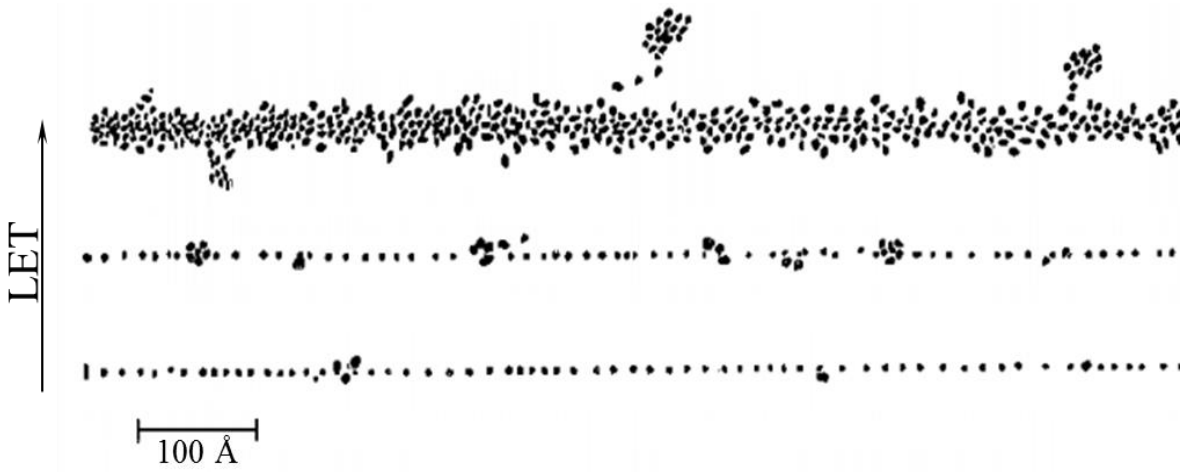

Figure 28: *A schematic representation of how linear energy transfer (LET) alters the distribution of spurs along a radiation track. Image was recreated from Allen A.O.*[4]

The distribution of spurs along a track has an effect on the diffusion of primary radiolysis species and ultimately alters the primary yields. Experiments carried out using ^{210}Po to irradiate solutions of iron sulphate through various thicknesses of mica have shown the effects of changing LET on the yield of oxidation of Fe^{2+}.[76] From this, subsequent studies using cyclotron accelerated protons have measured the effects of LET on the primary yields of water radiolysis.[77] Compiling the data from these studies gives a general picture of the effects of LET on water radiolysis primary yields, which is shown below.

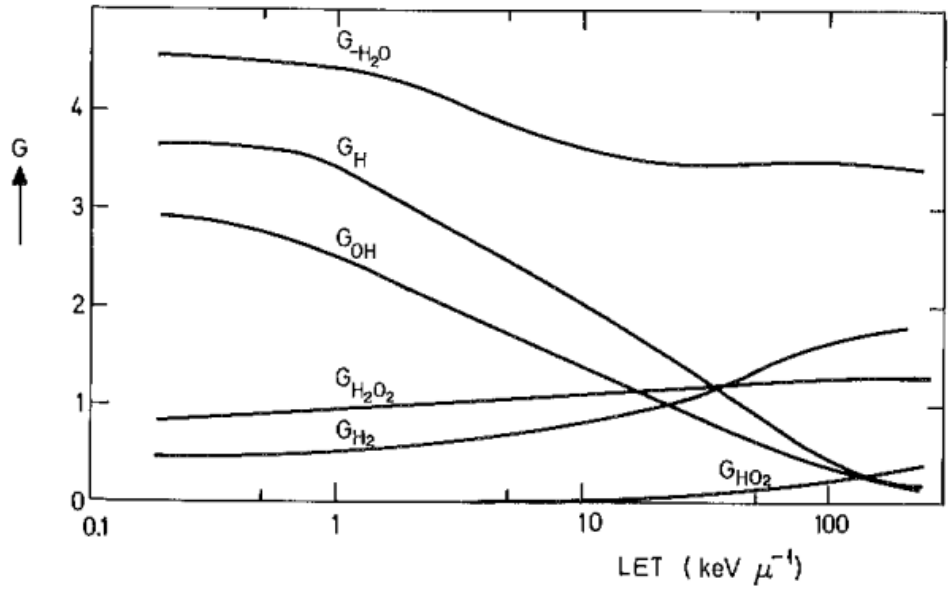

Figure 29: *Simulation data showing the effects of increasing linear energy transfer on the primary yields of water radiolysis. Image was recreated from Allen A.O.*[4]

The general trend shows an increase in the formation of molecular products at higher LET at the expense of radical species (with the exception of hydroperoxyl radical ($^{\cdot}HO_2$)) at very high LET values, whilst lower LET values favour the radical species. Currently, there is no clear agreed explanation as to how the hydroperoxyl radical is formed at high LET. Gamma rays from cobalt-60 fall in the low LET range and have an average value of 0.23 keV μm^{-1}.[78]

As the experiments conducted throughout this project used only cobalt-60 as a source of radiation, it was not necessary to incorporate the effects of linear energy transfer into this radiolysis model, nor was it necessary to include the primary yield of hydroperoxyl radicals into this model as the yield is negligible at the LET value of cobalt-60. Future iterations of this model would need to include the effects of linear energy transfer, as well as better methods for coping with the effects of temperature and pH; this is discussed in more detail in Chapter 8.

Mass Transfer of Volatile Species

The transfer of volatile species is not something that affects radiolysis primary yields, but it is important to include as the aqueous reactions of volatile species, namely molecular hydrogen and oxygen, will partition into the gas phase. This mass transfer is described within the model as two equations:

$$H_{2(aq)} \rightleftharpoons H_{2(g)}$$

$$O_{2(aq)} \rightleftharpoons O_{2(g)}$$

These equations take the form of first order rate equations with the rate constant substituted for a time dependant, net mass transfer coefficient (k_{app}) which includes an interfacial mass transfer coefficient (ν_{int}) and the Henry's equilibrium partition coefficient (K_p).[27]

$$\frac{dC^i_{(aq)}}{dt} = -k^i_{app}(t) \times C^i_{(aq)}(t)$$

$$k^i_{app} = v^i_{int} \times \frac{A_{int}}{V_{aq}} \left(1 - K^i_p \frac{C^i_g(t)}{C^i_{aq}(t)}\right)$$

C^i refers to the concentration of species i, in either the gas phase, or the aqueous phase. A_{int} and V_{aq} are used to describe some of the geometry of the radiolysis vessels used in experiments. A_{int} is the interfacial surface area between the two phases, while V is the volume of the aqueous or gas phase denoted by its subscript. As experiments were conducted in different sized vials depending on the analysis technique used, different values of A_{int} and V were used when comparing model predictions to experimental data.

This method assumes that the volume of liquid and covering gas is the same, which was true for all the experiments conducted during this work. If the liquid to gas volume ratio was anything other than 1, then the above differential should be adjusted to account for this ratio by the following modification.

$$\frac{-V_l}{V_g} \times \frac{dC^i_{(aq)}}{dt} = k^i_{app}(t) \times C^i_{(aq)}(t)$$

The interfacial mass transfer coefficient (v_{int}) incorporates the use of the stagnant two-film model which provides a description of resistance to diffusion through un-mixed boundary layers (see Figure 30[79]).

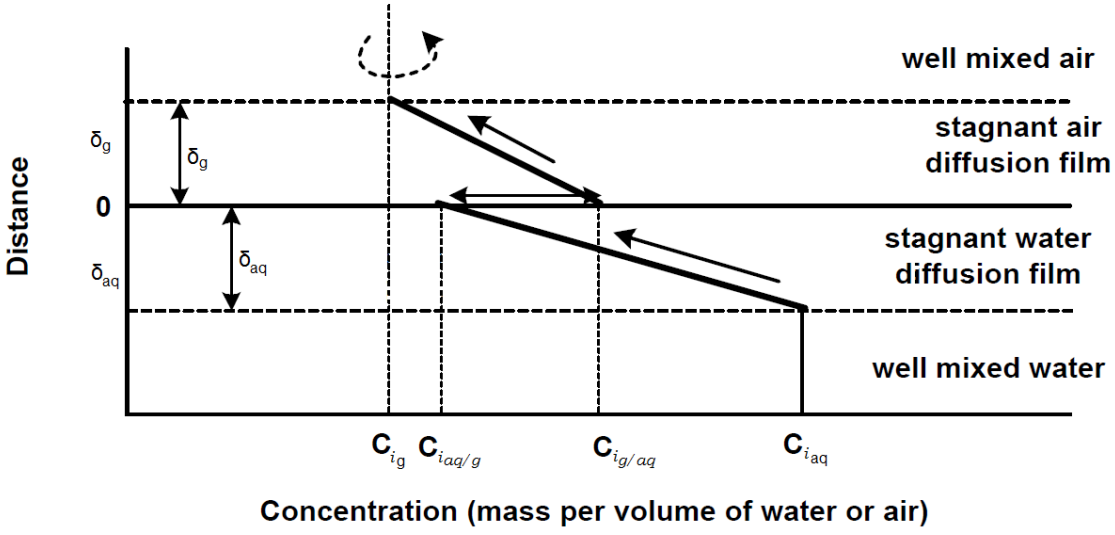

Figure 30: *A representation of the stagnant two-film model used to calculate the partitioning of volatile species.*[79]

The stagnant two-film model is incorporated into the mass transfer coefficient by relating the species diffusivity coefficients (D), the boundary thickness (δ), and the Henry's equilibrium partition coefficient (K_p).

$$\frac{1}{v_{int}^{i}} = \frac{1}{\left(\frac{D_{aq}^{i}}{\delta_{aq}}\right)} + \frac{K_{p}^{i}}{\left(\frac{D_{g}^{i}}{\delta_{g}}\right)}$$

$$K_{p}^{i} = \frac{C_{aq}^{i}(eq)}{C_{g}^{i}(eq)}$$

The diffusivity of volatile species is a temperature dependant coefficient which is included in the model through the use of polynomial fits to data obtained from literature, and is shown in figure 31[80-83]. Henry's coefficients were taken from literature which included equations for describing the temperature dependence, so a polynomial fit was not necessary[84]. The Henry's equilibrium partition coefficient is a dimensionless ratio between the aqueous and gas phase concentrations of a volatile species at equilibrium. This value is related to the Henry's law constant (k_H) by the following relationship.

$$T \times k_{H}^{i} = 12.2 \times K_{p}^{i}$$

The value 12.2 is used to convert between the Henry's law coefficient in mol m_{aq}^{-3} Pa^{-1} and the dimensionless Henry's law coefficient. While T represents the temperature in Kelvin, the Henry's law constant also has its own temperature dependency built in; this is described by the following relationship.

$$k_H = k_H^{\theta} \times EXP\left(\frac{\Delta H_{soln}}{R}\left(\frac{1}{T} - \frac{1}{T^{\theta}}\right)\right)$$

The Henry's constant at standard temperature (298.15 K) (k_H^{θ}) is quoted in the literature as being 1.3×10^{-3} mol dm^{-3} atm^{-1} for oxygen and 7.8×10^{-4} mol dm^{-3} atm^{-1} for hydrogen. ΔH_{soln} is the enthalpy of solution and R is the gas constant, the average ratios are quoted in the literature as 1650 for oxygen and 543 for hydrogen.[84]

This gives values for the Henry's equilibrium partition coefficient (K_p^i) of 0.019 and 0.031 for hydrogen and oxygen respectively, at 25°C and smaller values at higher temperatures.

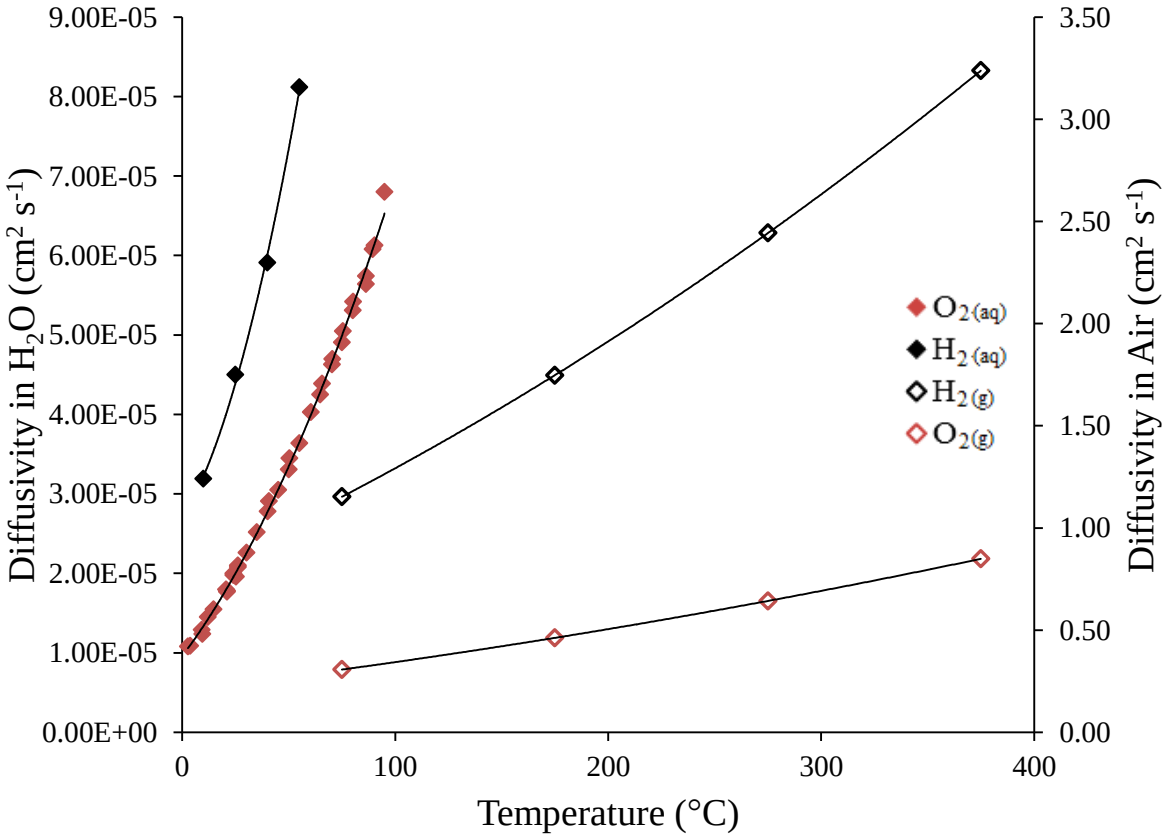

Figure 31: *The diffusivity of O_2 and H_2 in both water and air as a function of temperature.*

Diffusivity	Polynomial
$O_{2(aq)}$	$2.0\times10^{-9} \times t^2 + 4.0\times10^{-7} \times t + 1.0\times10^{-5}$
$O_{2(g)}$	$1.0\times10^{-6} \times t^2 + 1.2\times10^{-3} \times t + 0.2073$
$H_{2(aq)}$	$1.0\times10^{-8} \times t^2 + 4.0\times10^{-7} \times t + 3.0\times10^{-5}$
$H_{2(g)}$	$5.0\times10^{-6} \times t^2 + 4.7\times10^{-3} \times t + 0.7719$

Table 11: *Polynomial equations used to estimate the temperature effects on the diffusivity of O_2 and H_2 in both gas and aqueous phases where t = temperature (C°).*

Water Radiolysis Reaction Set

The radiolysis model simulates the chemical kinetics of homogeneous radiolysis through the use of simultaneous differential equations that represent the independent chemical reactions taking place. The model therefore includes a set of reactions accompanied by reaction rate constants. Tables 12 - 14 gives a summary of the reaction set used, with a full description of the reaction set, including the associated temperature dependences is given in appendix A. The reaction rate coefficients are taken from multiple sources with the majority from the compilation of A. J. Elliot and D. M. Bartels.[45]

Reaction Number	Primary Species Production	G-value (Molecules/100eV)	Ref
G0	$H_2O \rightsquigarrow e^-_{(aq)}$	2.71	45
G1	$H_2O \rightsquigarrow H^\bullet$	0.54	45
G2	$H_2O \rightsquigarrow H_2$	0.41	45
G3	$H_2O \rightsquigarrow {}^\bullet OH$	2.70	45
G4	$H_2O \rightsquigarrow H_2O_2$	0.68	45
G5	$H_2O \rightsquigarrow H^+_{(aq)}$	2.71	45

Table 12: *A list of Primary Species used to model water radiolysis*

Reaction Number	Chemical Reactions	Rate Constant k (M^{-1} s^{-1} @25°C)	Ref
R0	$e^-_{aq} + e^-_{aq} \rightarrow H_2 + 2OH^-$	7.26×10^9	45
R1	$e^-_{aq} + H^\bullet \rightarrow H_2 + OH^-$	2.76×10^{10}	45
R2	$e^-_{aq} + {}^\bullet OH \rightarrow OH^-$	3.55×10^{10}	45
R3	$e^-_{aq} + {}^\bullet O^- \rightarrow 2OH^-$	2.31×10^{10}	49
R4	$e^-_{aq} + H_2O_2 \rightarrow OH^- + {}^\bullet OH$	1.36×10^{10}	45
R5	$e^-_{aq} + HO_2^\bullet \rightarrow HO_2^-$	1.30×10^{10}	45
R6	$e^-_{aq} + HO_2^- \rightarrow O^{\bullet -} + OH^-$	3.51×10^9	49
R7	$e^-_{aq} + O_2 \rightarrow O_2^{\bullet -}$	2.25×10^{10}	45
R8	$e^-_{aq} + O_2^{\bullet -} \rightarrow O_2^{2-} + H_2O$	1.30×10^{10}	43,49
R9	$H^\bullet + H^\bullet \rightarrow H_2$	5.14×10^9	45
R10	$H^\bullet + {}^\bullet OH \rightarrow H_2O$	1.09×10^{10}	45
R11	$H^\bullet + H_2O_2 \rightarrow {}^\bullet OH + H_2O$	3.65×10^7	45
R12	$H^\bullet + O_2 \rightarrow HO_2^\bullet$	1.30×10^{10}	45
R13	$H^\bullet + O_2^{\bullet -} \rightarrow HO_2^-$	1.14×10^{10}	45
R14	$H^\bullet + HO_2^\bullet \rightarrow 2{}^\bullet OH$	1.14×10^{10}	45
R15	$H^\bullet + HO_2^- \rightarrow {}^\bullet OH + OH^-$	1.37×10^9	85

R16	$H^{\bullet} + O_3 \rightarrow {}^{\bullet}OH + O_2$	2.20×10^{10}	43
R17	${}^{\bullet}OH + {}^{\bullet}OH \rightarrow H_2O_2$	4.81×10^{9}	45
R18	${}^{\bullet}OH + H_2O_2 \rightarrow H_2O + HO_2^{\bullet}$	2.92×10^{7}	45
R19	${}^{\bullet}OH + HO_2^{-} \rightarrow OH^{-} + HO_2^{\bullet}$	8.13×10^{9}	45
R20	${}^{\bullet}OH + HO_2^{\bullet} \rightarrow H_2O + O_2$	8.84×10^{9}	45
R21	${}^{\bullet}OH + O_2^{\bullet-} \rightarrow OH^{-} + O_2$	1.10×10^{10}	45
R22	${}^{\bullet}OH + O_3 \rightarrow HO_2^{\bullet} + O_2$	1.10×10^{8}	43
R23	${}^{\bullet}O_3^{-} + H_2O_2 \rightarrow O_2^{\bullet-} + O_2 + H_2O$	1.59×10^{6}	43
R24	${}^{\bullet}O_3^{-} + HO_2^{-} \rightarrow O_2^{\bullet-} + O_2 + OH^{-}$	8.87×10^{5}	43
R25	${}^{\bullet}O_3^{-} + H_2 \rightarrow O_2 + H^{\bullet} + OH^{-}$	2.49×10^{5}	46
R26	${}^{\bullet}O_3^{-} + {}^{\bullet}OH \rightarrow HO_2^{\bullet} + O_2^{\bullet-}$	6.000×10^{9}	43
R27	${}^{\bullet}O_3^{-} + {}^{\bullet}OH \rightarrow HO^{-} + O_3$	2.50×10^{9}	43
R28	${}^{\bullet}O_3^{-} + H^{+}_{(aq)} \rightarrow O_2 + {}^{\bullet}OH$	9.00×10^{10}	43
R29	$O_2^{\bullet-} + O_2^{\bullet-} \xrightarrow{+H_2O} O_2 + O_2^{2-}$	2.99×10^{-1}	43
R30	$O_2^{\bullet-} + HO_2^{-} \rightarrow O_2 + {}^{\bullet}O^{-} + OH^{-}$	8.23×10^{-2}	43
R31	$O_2^{\bullet-} + H_2O_2 \rightarrow O_2 + {}^{\bullet}OH + OH^{-}$	1.30×10^{-1}	43
R32	$O_2^{\bullet-} + HO_2^{\bullet} \rightarrow O_2 + HO_2^{-}$	7.60×10^{7}	43
R33	$O_2^{\bullet-} + {}^{\bullet}O_3^{-} \rightarrow O^{2-} + 2O_2$	1.00×10^{4}	43
R34	$O_2^{\bullet-} + O_3 \rightarrow {}^{\bullet}O_3^{-} + O_2$	1.50×10^{9}	43
R35	$HO_2^{\bullet} + HO_2^{\bullet} \rightarrow H_2O_2 + O_2$	8.40×10^{5}	45
R36	$HO_2^{\bullet} + H_2O_2 \rightarrow O_2 + H_2O + {}^{\bullet}OH$	5.00×10^{-1}	49
R37	$HO_2^{\bullet} + O_3 \rightarrow {}^{\bullet}OH + 2O_2$	5.00×10^{8}	43
R38	$H_2O_2 + HO_2^{-} \rightarrow O_2 + H_2O + OH^{-}$	4.50×10^{-4}	43
R39	$O_3 + OH^{-} \rightarrow HO_2^{-} + O_2$	4.80×10^{1}	43
R40	$O_3 + HO_2^{-} \rightarrow {}^{\bullet}OH + O_2 + O_2^{\bullet-}$	5.50×10^{6}	43
R41	$O_3 + H_2O_2 \rightarrow {}^{\bullet}OH + O_2 + HO_2^{\bullet}$	3.71×10^{-2}	43
R42	$H^{\bullet} + {}^{\bullet}O^{-} \rightarrow OH^{-}$	2.00×10^{10}	43

R43	$^{\bullet}O_3^- + e^-_{aq} \rightarrow 2OH^- + O_2$	1.60×10^{10}	43
R44	$O_3 + e^-_{aq} \rightarrow {}^{\bullet}O_3^-$	3.60×10^{10}	43
R45	$H_2O_2 \rightarrow 2{}^{\bullet}OH$	2.30×10^{-7}	86
R46	$O^{2-} + H_2O \rightarrow 2OH^-$	1.00×10^{10}	43
R47	$^{\bullet}O^- + H_2 \rightarrow {}^{\bullet}H + OH^-$	1.28×10^{8}	45
R48	$^{\bullet}O^- + H_2O_2 \rightarrow O_2^{\bullet-} + H_2O$	5.55×10^{8}	49
R49	$^{\bullet}O^- + HO_2^- \rightarrow O_2^{\bullet-} + OH^-$	7.86×10^{8}	45
R50	$^{\bullet}O^- + O_2^{\bullet-} \rightarrow O^{2-} + O_2$	6.00×10^{8}	43
R51	$^{\bullet}O^- + {}^{\bullet}O^- \rightarrow O_2^{2-}$	1.00×10^{8}	43
R52	$^{\bullet}O^- + {}^{\bullet}OH \rightarrow HO_2^-$	7.61×10^{9}	49
R53	$^{\bullet}O^- + O_3^- \rightarrow 2O_2^{\bullet-}$	7.00×10^{8}	43
R54	$^{\bullet}O^- + O_3 \rightarrow O_2^{\bullet-} + O_2$	1.00×10^{9}	43

Table 13: *A list of reactions used to model water radiolysis.*

	Equilibria	k_f (M^{-1} s^{-1} @25°C)	k_b (M^{-1} s^{-1} @25°C)	Ref
R55/56	$H_2O \rightleftharpoons H^+_{(aq)} + OH^-$	1.17×10^{-3}	1.18×10^{11}	45
R57/58	$H_2O_2 \rightleftharpoons H^+_{(aq)} + HO_2^-$	8.90×10^{-2}	4.78×10^{10}	45
R59/60	$H_2O_2 + OH^- \rightleftharpoons HO_2^- + H_2O$	1.27×10^{10}	1.40×10^{6}	45
R61/62	$HO_2^- + OH^- \rightleftharpoons O_2^{2-} + H_2O$	3.51×10^{5}	1.10×10^{6}	43
R63/64	$^{\bullet}OH \rightleftharpoons H^+_{(aq)} + {}^{\bullet}O^-$	8.90×10^{-2}	4.78×10^{10}	45
R65/66	$^{\bullet}OH + OH^- \rightleftharpoons {}^{\bullet}O^- + H_2O$	1.27×10^{10}	1.40×10^{6}	45
R67/68	$^{\bullet}O^- + O_2 \rightleftharpoons {}^{\bullet}O_3^-$	3.75×10^{9}	2.62×10^{3}	45
R69/70	$HO_2^{\bullet} \rightleftharpoons H^+_{(aq)} + O_2^{\bullet -}$	4.78×10^{10}	7.35×10^{5}	45
R71/72	$HO_2^{\bullet} + OH^- \rightleftharpoons O_2^{\bullet -} + H_2O$	1.27×10^{10}	1.63×10^{-1}	45
R73/74	$H^{\bullet} \rightleftharpoons e^-_{aq} + H^+_{(aq)}$	5.83	2.10×10^{10}	45
R75/76	$H^{\bullet} + OH^- \rightleftharpoons e^-_{aq} + H_2O$	2.44×10^{7}	1.74×10^{1}	45
R77/78	$H^{\bullet} + H_2O \rightleftharpoons H_2 + {}^{\bullet}OH$	4.58×10^{-5}	3.95×10^{7}	45
R79	$H_{2(aq)} \rightleftharpoons H_{2(g)}$	2.69×10^{-3}		
R80	$O_{2(aq)} \rightleftharpoons O_{2(g)}$	1.03×10^{-4}		

Table 14: *A list of equilibria used to model the radiolysis of water.*

Computational Assumptions and Error

The first assumption this model makes is that radiolysis does not occur in the gas phase. In reality this is not the case, however the density of the gas phase is so small compared to that of the aqueous phase that any contribution from gas phase radiolysis will be negligible. There are several reactions that do not include any kind of temperature dependence for their associated rate constants. This is due to a lack of information available in the literature, many of the species involved in these reactions are notoriously difficult to measure reaction rate constants for; thus these reactions have a fixed rate constant across all temperatures. The method for estimating the primary yields to account for both temperature and pH effects is not an ideal method. Multiple linear regression analysis is often used to empirically predict the value of a single dependant variable based on the contributions of multiple independent variables. In the case of this model, the independent variables are temperature and pH; a full model would also include LET as a third independent variable. The number of observations considered for the regression analysis is less than ideal due to the scarcity of available data, coupled with the difficulty of relating non-linear variables, means that predictions of primary yields are loose estimates at best. The coefficient of determination (R^2) gives information about how well the multiple regressions fit the data and is shown in Table 15; where μ denotes the estimated standard deviation of the error.

Primary Yield	R^2	μ
$g(e_{aq}^-)$	0.612	0.249
$g(H_2O_2)$	0.934	0.045
$g(H_2)$	0.907	0.032
$g(^{\bullet}OH)$	0.950	0.265
$g(H^{\bullet})$	0.925	0.108

Table 15: *Statistical information concerning the estimation of primary yields used to model the radiolysis of water.*

The partition of volatile species depends on a number of parameters, some of which are dependent on geometry. Although H_2O_2 is not a volatile species, its concentration is strongly affected by the concentration of aqueous O_2, it is therefore necessary to include gas partitioning methods in both H_2 and H_2O_2 model calculations. The interfacial surface area (A_{int}) is one such parameter, although this can be roughly determined by measuring the geometry of the vials being used. Other parameters such as the boundary thicknesses (δ) are not so easily measured and are parameter fitted. This is done using the parameter fitting functionality built into FACSIMILE. Experimental data is supplied to FACSIMILE and the desired parameters to fit are declared, the calculation is then performed a number of times, slightly varying the declared parameters each time until the predicted values better match the provided experimental data. For this work, the data provided to FACSIMILE was the concentration of H_2 and H_2O_2 in aerated water as a function of dose (Figures 32-33). Vials of different geometry have different boundary thicknesses, the values used throughout this work are shown in Table 16.

Parameter	Vial Used for H_2 Analysis	Vial Used for H_2O_2 Analysis
$\mathbf{A_{int}\ (m^2)}$	5.02×10^{-5}	2.84×10^{-4}
$\mathbf{\delta_{aq}\ (m)}$	5.80×10^{-4}	5.10×10^{-4}
$\mathbf{\delta_{g}\ (m)}$	2.60×10^{-2}	2.60×10^{-2}

Table 16: *Parameters used to describe interfacial surface area (Aint) and boundary thicknesses (δ) for sample vials of different geometry.*

Chapter 4: The Radiolysis of Aqueous Solutions at High pH

Preliminary Radiolysis Studies of Pure Water

Preliminary experiments to measure hydrogen peroxide and hydrogen gas concentrations from the radiolysis of aerated and deaerated water at neutral pH were carried out as a control to which other measurements may be compared. Computational modelling of these pure water systems were performed with the radiolysis model described in Chapter 3 to validate the models performance.

Measurements of hydrogen peroxide were made using the Ghormley Tri-iodide method described in Chapter 2. The pH of the stock was measured using a Mettler Toledo SevenMulti™ pH meter equipped with a probe capable of measuring pH in the range 0-14, and was found to be 6.99. Aliquots of 10 mL from the pure water stock were sealed in 20 mL headspace vials so that the liquid to headspace ratio was 1:1, and were irradiated in row 1 of the 4x8 sample rack; the average dose rate was 283.9 Gy min^{-1}. The experiment was run twice, prior to irradiation samples used in the first run were sealed but left aerated while samples used in the second run were sealed in gas tight vials equipped with rubber septa and were sparged for 20 minutes with zero grade argon gas to remove all dissolved oxygen. The results of the two experimental runs are shown in Figure 32.

Preliminary measurements of hydrogen gas production were also carried out using pure water. 2 mL aliquots of pure water stock were flame sealed in 4 mL glass vials which were then secured in the inverter rig and irradiated for various periods of time: the average dose rate was 285.1 Gy min^{-1}. Post irradiation analysis was carried out by the previously described crush tube method of gas chromatography.

As flame sealing introduces slight irregularity in the volume of headspace, an assumption was made that the headspace of the sealed vial was 2 mL.

This allows the conversion of measured quantities (µL) of hydrogen to a concentration (mol dm^{-3}). Once again the experiment was run twice with the second experimental run using samples that have been deaerated with argon and the results are shown in Figure 33.

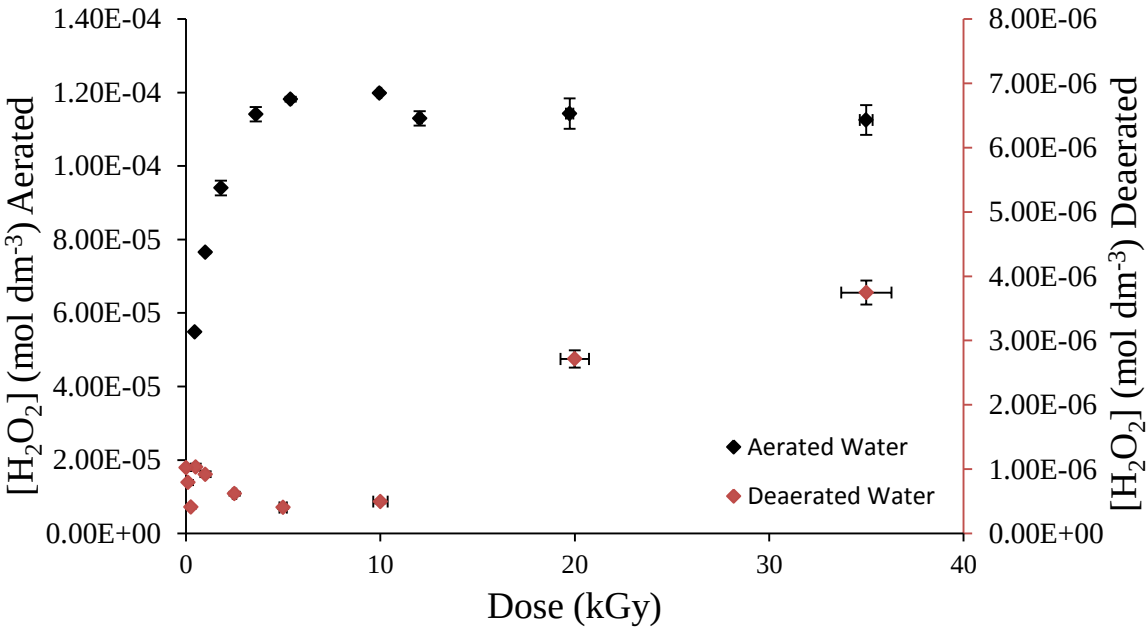

Figure 32: *Measurements of H_2O_2 concentration as a function of dose for aerated water (♦) and deaerated water (♦). Vertical error bars show the standard deviation between replicates while horizontal error bars show the dose range for replicates.*

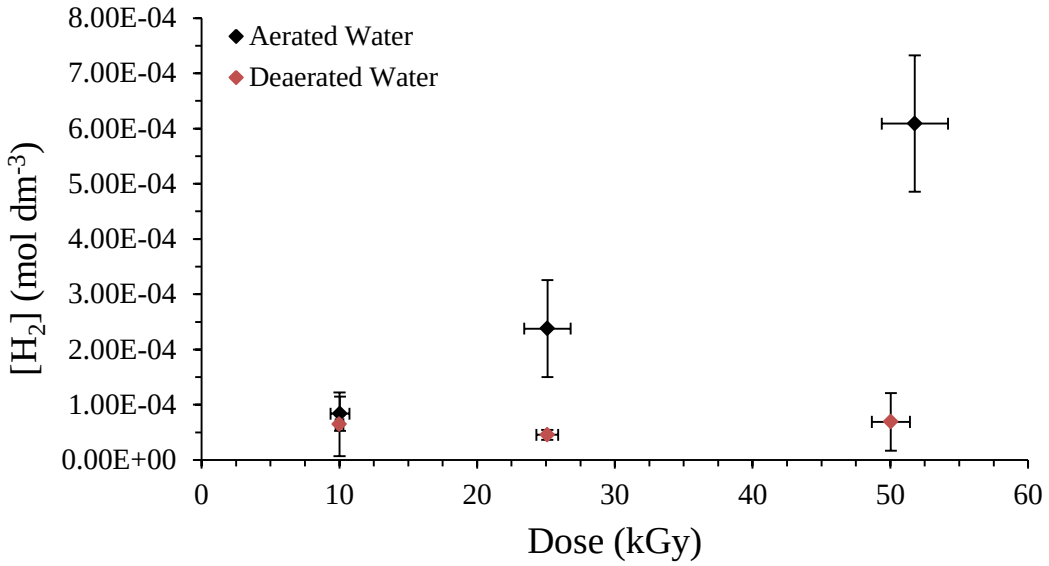

Figure 33: *Measurements of H_2 as a function of dose in aerated (♦) and deaerated (♦) samples. Vertical error bars show the standard deviation of replicates while horizontal error bars show the dose range for replicates.*

Discussion

Aerated samples resulted in a steady-state concentration of hydrogen peroxide at approximately 1.1 $\times 10^{-4}$ mol dm^{-3}, while molecular hydrogen continues to form with absorbed dose over the range considered. In order to satisfy the mass balance requirements, some other species must be formed after the achievement of the peroxide steady-state that is also proportional to hydrogen formation. The most likely candidate for this is molecular oxygen, which would have to be formed at half the rate of hydrogen.

Samples that did not contain any dissolved oxygen failed to produce significant quantities of hydrogen peroxide or hydrogen gas, with a very low steady state eventually achieved at approximately 4.0 $\times 10^{-6}$ mol dm^{-3}. This may be attributed to the radiolytic production of oxygen required to satisfy mass balance. Using the radiolysis model a predicted chemical yield can be obtained after the establishment of the hydrogen peroxide steady state to show that mass balance is satisfied by oxygen production. The predicted chemical yields were calculated between doses of 15 kGy to 30 kGy.

For oxygen gas, the predicted chemical yield was $G(O_2) = 0.011$ while the predicted yield of hydrogen gas formation in deaerated water was $G(H_2) = 0.022$. In both cases, samples that were aerated produced much larger quantities of hydrogen and hydrogen peroxide than their deaerated equivalents. This was somewhat expected as it has long been considered that dissolved oxygen is reduced and the reduction products are able to react with hydroxyl radicals, preventing them from removing hydrogen peroxide and hydrogen.[87] The general scheme, first proposed in 1954, for this protection mechanism is initiated by the reaction of hydrogen atoms with oxygen to produce hydroperoxyl radicals, these then react with hydroxyl radicals to reform water and oxygen, or with itself to form hydrogen peroxide and oxygen.[4]

$$H^{\cdot} + O_2 \rightarrow HO_2^{\bullet} \quad \text{(R12)}$$

$$^{\cdot}OH + H_2O_2 \rightarrow H_2O + HO_2^{\bullet} \quad \text{(R18)}$$

$$HO_2^{\bullet} + HO_2^{\bullet} \rightarrow H_2O_2 + O_2 \quad \text{(R35)}$$

$$^{\cdot}OH + HO_2^{\bullet} \rightarrow H_2O + O_2 \quad \text{(R20)}$$

More recent studies by the research group led by Clara Wren have deployed computational methods to investigate further, the effects of dissolved oxygen on the steady-state concentration of both hydrogen peroxide and molecular hydrogen.[86] The calculations performed in this study also supported the idea that dissolved oxygen is reduced and it is the reduction products that scavenge hydroxyl radicals, resulting in the protection of hydrogen peroxide and molecular hydrogen. The calculations revealed that oxygen is mainly reduced by the hydrated electron and that the superoxide formed is responsible for the scavenging of hydroxyl radicals. This process serves as a catalytic mechanism for the overall reaction between the solvated electron and hydroxyl radicals.

$$e^-_{aq} + O_2 \rightarrow O_2^- \quad \text{(R7)}$$

$$O_2^- + {}^\bullet OH \rightarrow OH^- + O_2 \quad \text{(R21)}$$

Overall Reaction: $$e^-_{aq} + {}^\bullet OH \rightarrow OH^- \quad \text{(R2)}$$

This scavenging of hydroxyl radicals has a larger impact on protecting hydrogen as the reaction between hydrogen and the hydroxyl radical is the only significant removal path of hydrogen in neutral conditions.

Wren proposes that high concentrations of hydrogen peroxide seen in aerated solutions can be attributed to a change in the production pathway for hydrogen peroxide in the presence of oxygen. The reaction between both the reduction products of oxygen becomes the dominant production pathway for hydrogen peroxide.

$$HO_2^\bullet + O_2^- \rightarrow HO_2^- + O_2 \quad \text{(R32)}$$

$$H^+_{(aq)} + O_2^- \rightleftharpoons HO_2^\bullet \quad \text{(R69/70)}$$

$$H^+_{(aq)} + HO_2^- \rightleftharpoons H_2O_2 \quad \text{(R57/58)}$$

Similar calculations were performed in this work using the computational method described in Chapter 3. The computational predictions shown in figures 34 and 35 serve as a baseline to demonstrate that the computational model performs well, at least at a fundamental level before building up to more complex systems.

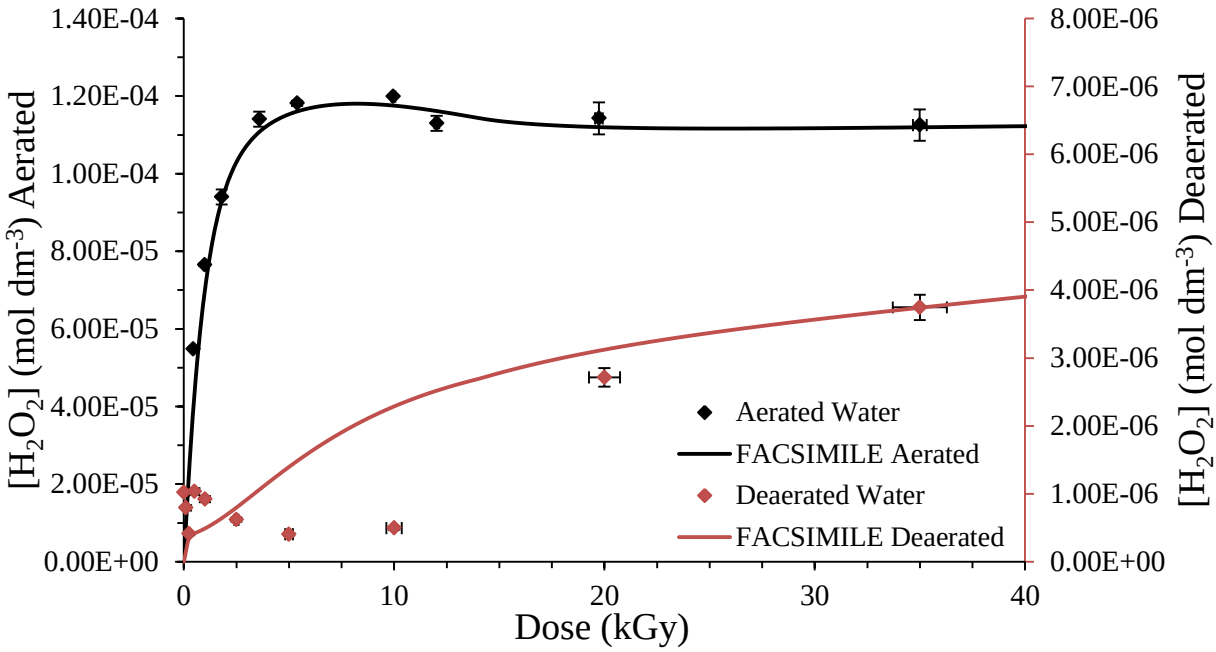

Figure 34: *Predicted concentrations of H_2O_2 as calculated by the radiolysis model for both aerated (—) and deaerated (—) conditions.*

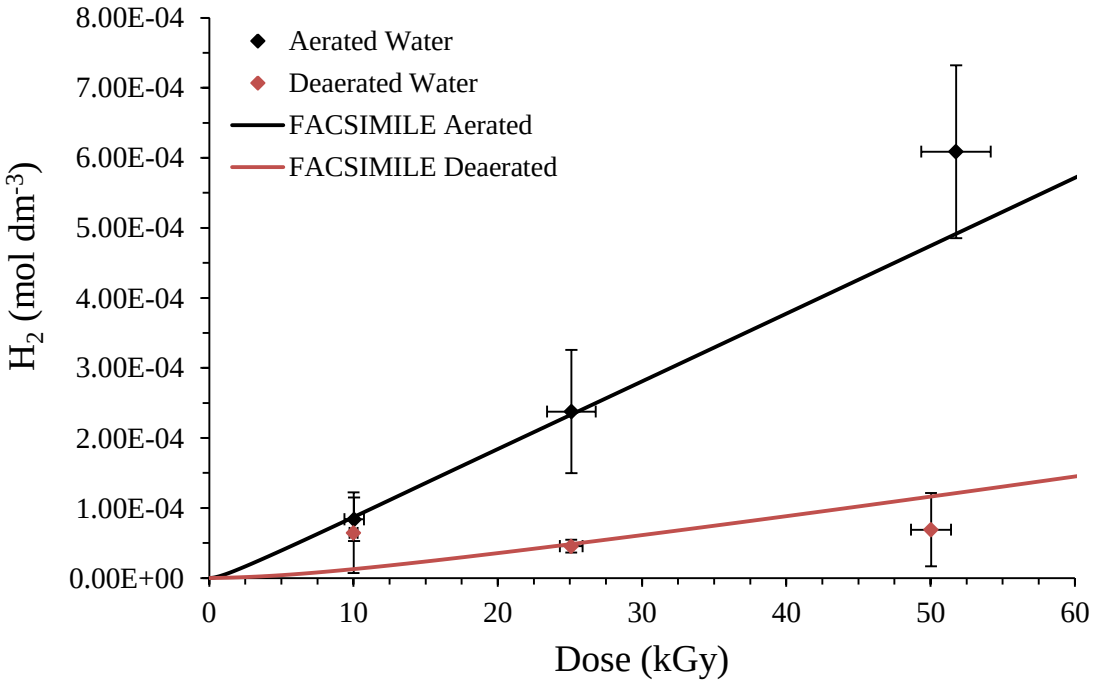

Figure 35: *Predicted concentrations of H_2 gas as calculated by the radiolysis model for both aerated (—) and deaerated (—) conditions.*

The predictions made for the concentrations of hydrogen peroxide and hydrogen gas in pure water match well with the observed measurements, especially for the concentration of hydrogen peroxide produced in aerated water. The most obvious discrepancy is the disparity between the early predictions of hydrogen peroxide concentration and the measured concentration for deaerated samples, which is most likely due to imperfect oxygen removal from the samples. As the predictions are in generally good agreement with the experimental measurements it is not unreasonable to assume that steady state concentrations of other species, which cannot or were not determined experimentally during this work, can be estimated by the model.

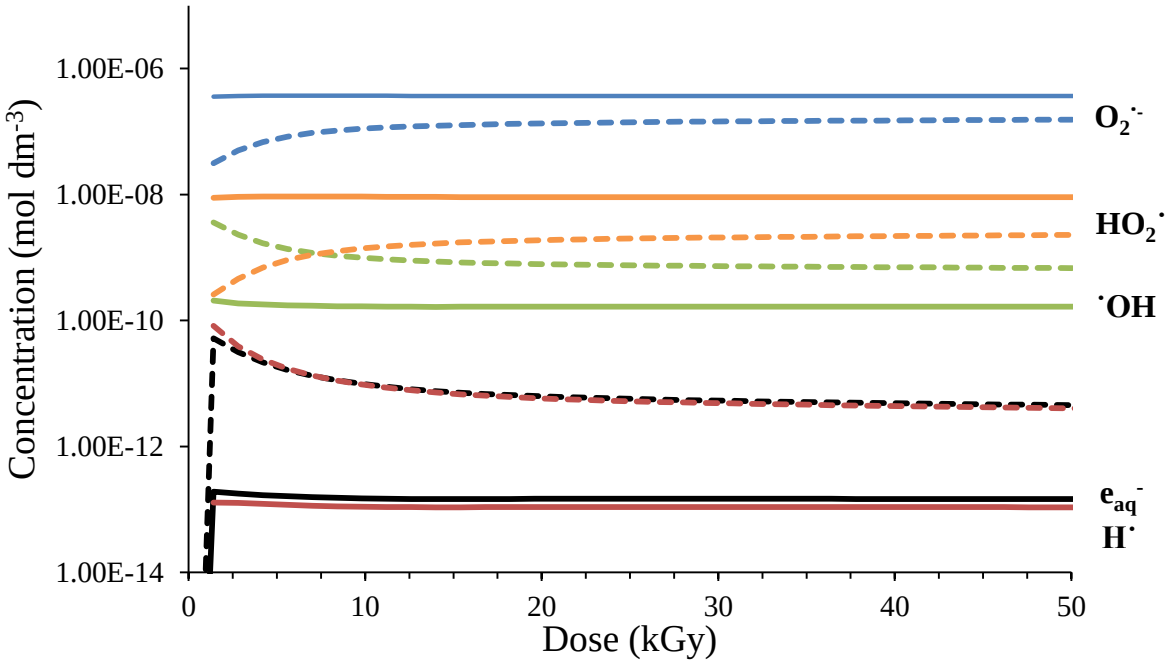

Figure 36: *Calculated concentrations of the major oxidising and reducing water radiolysis species as a function of dose. Solid lines represent aerated conditions while broken lines represent deaerated conditions.*

Figure 36 shows the predicted concentrations of various radical species in both aerated and deaerated water. The calculated concentrations agree with previously published calculations by Wren and co-workers.[86]

Under aerated conditions, reducing species $H^{\cdot}$ and e_{aq}^{-} have significantly lower concentrations than in deaerated conditions due to scavenging by oxygen. The resulting reduction products of oxygen are superoxide and hydroperoxyl radicals, and both show an increased concentration in aerated conditions.

The experiments in the following sections concerning the measurement of hydrogen peroxide, were all performed in aerated conditions to resemble the conditions at the Sellafield site. Measurements of hydrogen were, for the most part, carried out under deaerated conditions.

Measurements of H_2O_2 in the Radiolysis of High pH Solutions

Stock solutions of various pH were prepared using NaOH dissolved in ultra-pure water. From each stock, sample sets were prepared from 10 mL aliquots of stock solution and sealed in 20 mL glass vials with aluminium crimp caps. The pH of the remaining sample stocks were measured and recorded. Irradiation dose rates were calculated from original measurements using the Fricke dosimetry method described previously. Sample sets were loaded into row 1 of the 4x8 irradiation rack and irradiated using the Model-812 cobalt-60 irradiator until they reached the desired dose. Table 17 summarises the dose rates and pH of the sample batches examined:

Sample Batch ID	Average Dose Rate for Row 1 (Gy min^{-1})	Measured pH
H2O2-PH00	285.12	6.99
H2O2-PH01	274.97	10.41
H2O2-PH02	274.07	11.08
H2O2-PH03	283.64	12.30
H2O2-PH04	274.67	12.74

Table 17: *Conditions of samples used to investigate hydrogen peroxide in high pH radiolysis.*

Results

Post irradiation analysis for H_2O_2 was carried out immediately after irradiation, using the previously described tri-iodide method. Analysis of high pH samples required additional acid to lower the pH to the conditions required by the analytical method; the quantities of acid used were recorded and the dilution effects have been accounted for. The results of this study are shown in Figure 37.

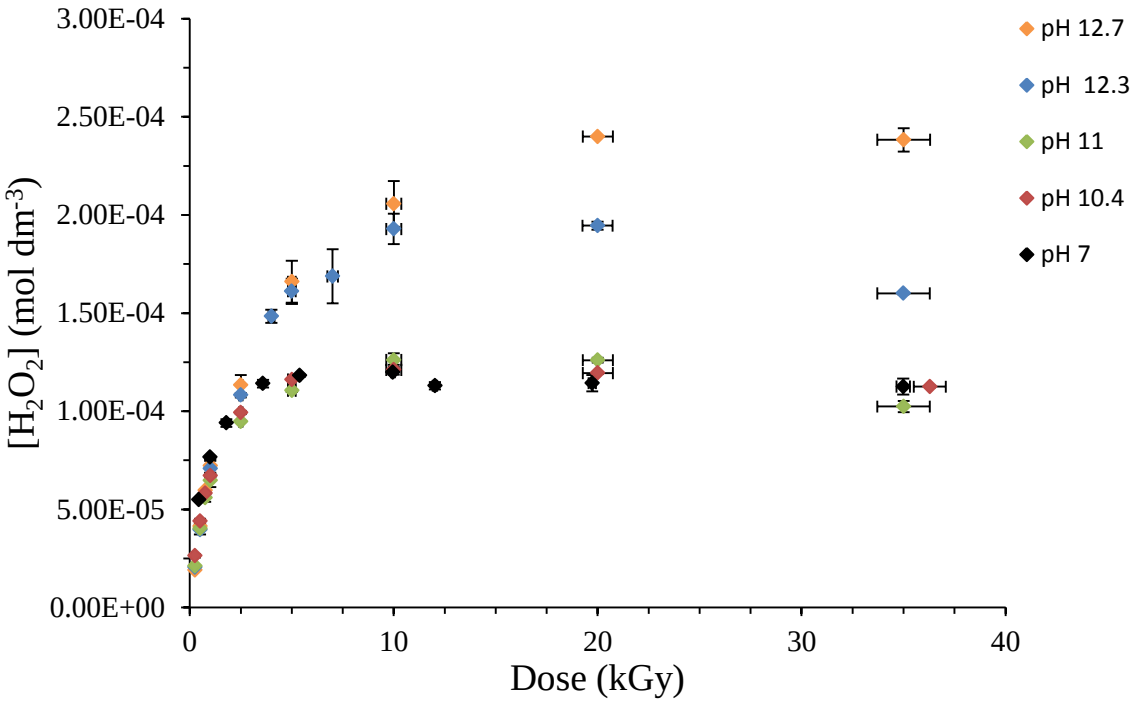

Figure 37: *Measurements of H_2O_2 concentrations as a function of dose for samples initially at pH 7 (♦), pH 10.4 (♦), pH 11 (♦), pH 12.3 (♦), and pH 12.7 (♦). All samples were aerated. Vertical error bars are the standard deviation between replicates, while horizontal error bars show the dose range for replicates.*

The steady state concentration of hydrogen peroxide is fairly consistent at about 1.15×10^{-4} mol dm^{-3} within the pH range 7-11, each attaining steady state after roughly 5 kGy. At higher pH values, both the steady state concentration and the dose at which steady state is achieved increase.

Samples at pH 12.3 required roughly 10 kGy to obtain a peak steady-state concentration of 1.95×10^{-4} mol dm^{-3} of hydrogen peroxide, while samples at pH 12.7 required even higher doses, almost 20 kGy to reach a steady concentration of 2.38×10^{-4} mol dm^{-3}. The data set from samples at pH 12.3 shows an apparent decrease in hydrogen peroxide concentration of ~18% at 35 kGy. A similar decrease in hydrogen peroxide concentration is also observed in samples of pH 11.

Measurements of H_2 in the Radiolysis of High pH Solutions

Stock solutions of various pH were prepared using NaOH, to match the pH range used in the measurement of hydrogen peroxide. Many of the acid-base equilibria used in the description of water radiolysis have pK_a values in the pH range investigated by this study. The behaviour of H_2 production observed at high pH may be influenced by a change in chemistry brought about by a shift in one or more of the acid-base equilibria. Table 18 shows the equilibria of interest and their associated pK_a value while Table 19 includes the measured pH of the stock solutions.

Equilibrium	pK_a
$\cdot OH \rightleftharpoons H^+_{(aq)} + \cdot O^-$	11.84
$H_2O_2 \rightleftharpoons H^+_{(aq)} + HO_2^-$	11.68
$H^\bullet \rightleftharpoons H^+_{(aq)} + e^-_{aq}$	9.74
$HO_2^\bullet \rightleftharpoons H^+_{(aq)} + O_2^-$	4.83

Table 18: *A list of important equilibria and their associated pK_a values.*

For the measurement of hydrogen, sample sets were prepared from 2 mL aliquots of stock solution which were transferred to glass "crush tube" vials described in chapter two. The vials were connected to a glass manifold via stainless steel needles and sparged with zero grade argon for 20 minutes to remove any dissolved oxygen before samples were flame sealed under argon.

Irradiation dose rates were calculated from original Fricke dosimetry study described previously. Samples were loaded into the four positions available in the inverter rig and irradiated until they reached the desired dose.

Results

After irradiation samples were analysed for hydrogen gas by gas chromatography using the "crush tube" technique described in Chapter 2. Figure 38 shows the amounts of H_2 produced as a function of radiation dose. As production rates of hydrogen gas are linear as a function of absorbed dose, chemical yields can be identified as the gradient, expressed in terms of molecules per 100 eV of absorbed energy. These results are summarised in Table 19 while the data is shown in Figure 38.

Sample Batch ID	Average Dose Rate for Inverter Rig (Gy min^{-1})	Measured pH	G(H_2)	Error ±
H2-PH00	283.85	6.99	0.021	0.002
H2-PH01	284.08	10.63	0.071	0.018
H2-PH02	290.39	12.32	0.352	0.005
H2-PH03	286.34	13.07	0.176	0.010

Table 19: *Conditions of samples used to investigate hydrogen gas in high pH radiolysis.*

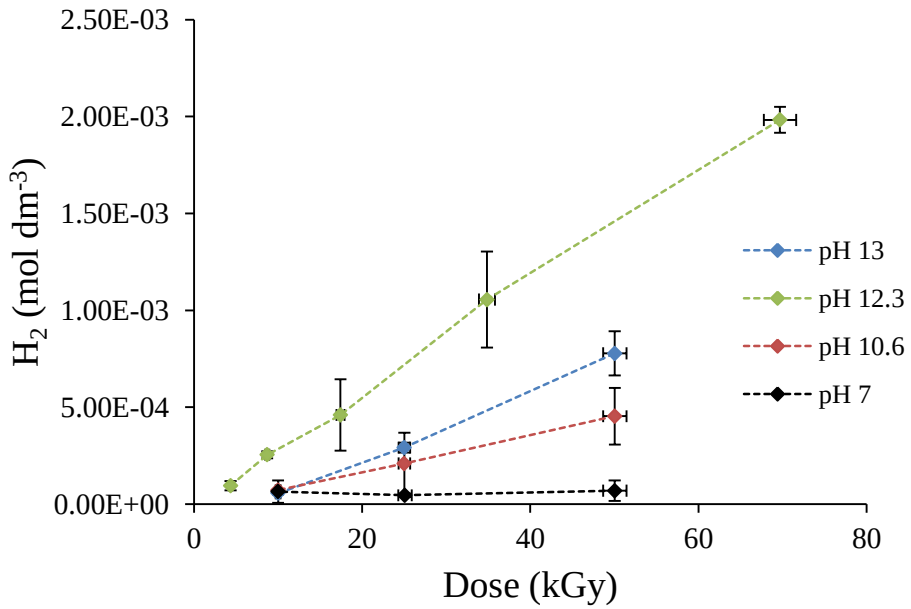

Figure 38: *Measurements of H_2 gas as a function of dose at pH 7 (♦), pH 10.6 (♦), pH 12.3 (♦), and pH 13 (♦). Dashed lines are provided to clarify the data trends, all samples were deaerated. Vertical error bars show the standard deviation between replicates while horizontal error bars show the dose range for replicates.*

Increasing the pH has the effect of increasing the chemical yield for hydrogen over the pH range 7 to 12.3; however the data set for pH 13 shows that the chemical yield for hydrogen is less than samples at pH 12.3. The results of the calculations using the reaction scheme given in Tables 12 - 14, for both hydrogen peroxide and hydrogen gas production are shown in Figures 39 and 40, respectively.

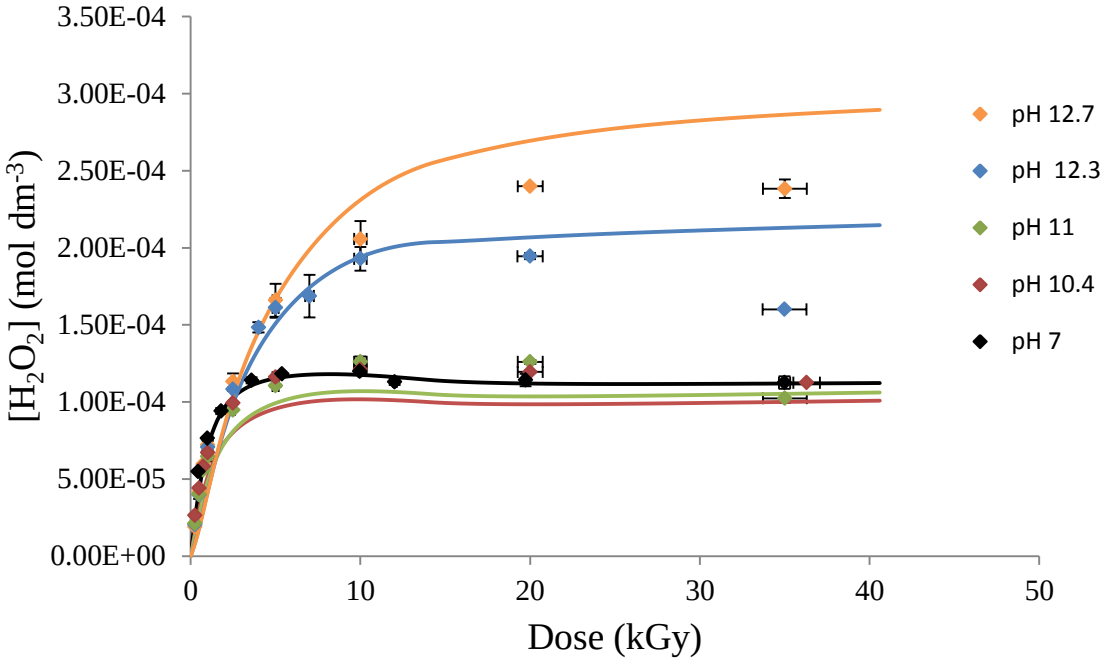

Figure 39: *Model calculations to show the predicted concentrations of H_2O_2 as a function of dose at various pH.*

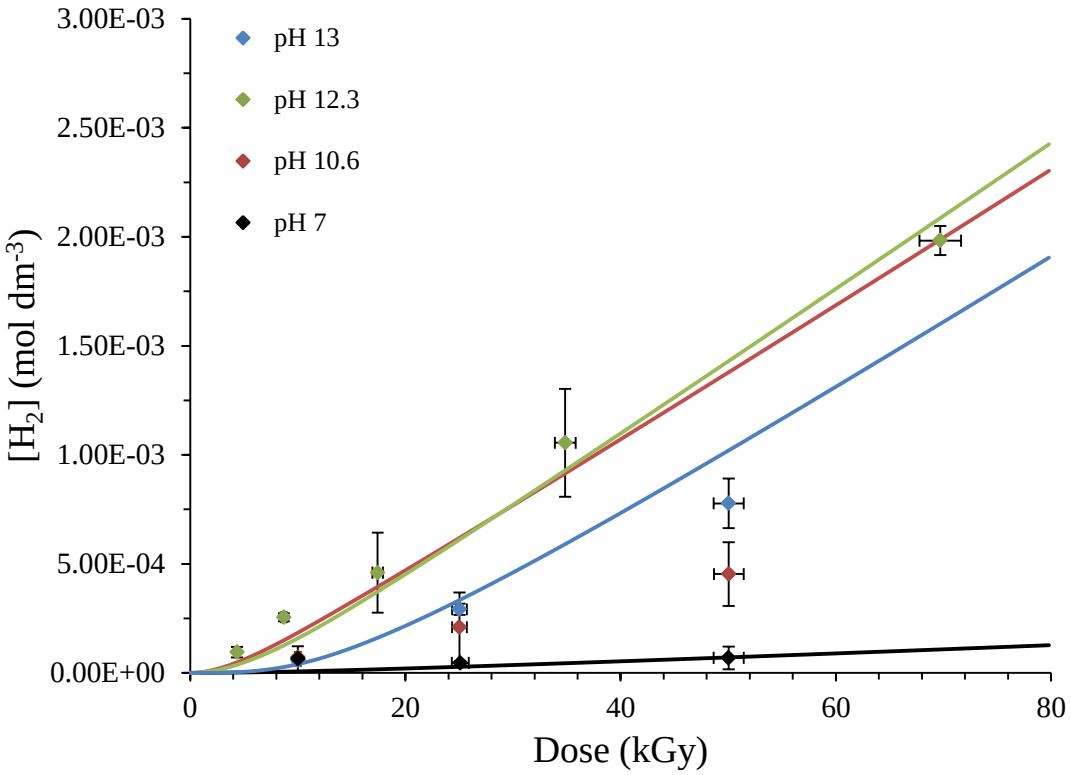

Figure 40: *Model calculations to show the predicted concentrations of H_2 gas as a function of dose at various pH.*

Calculated concentrations of hydrogen peroxide show the same trends as the data. The predictions at pH 10.4 and 11 take slightly longer to reach steady state than what the experimental data shows. Higher pH calculations follow the same trend as the experimental data but overestimate the steady state concentrations of hydrogen peroxide, especially in the calculations at pH 12.7.

Calculated concentrations of molecular hydrogen follow a slightly more unexpected trend. Predictions made for pH 10.6 massively overestimate hydrogen production rates: this is symptomatic of a misunderstanding of the mechanistic chemistry. A similar error has also been noted by Wren when performing calculations at this pH, a suggested fix was to increase the reaction rate between ozinide and molecular hydrogen by a factor of 8.[86]

Even with this higher rate, the over prediction of hydrogen is still large at pH 10.6, while predictions for pH 12.3 agree reasonably well with experimental data. This information at least helps to narrow the pH range at which this misunderstanding manifests. The pH range afflicted by over prediction of hydrogen falls close to the pK_a of the dissociation of the hydrogen atom at 9.74.

$$H^{\bullet} \rightleftharpoons H^{+}_{(aq)} + e^{-}_{(aq)} \qquad pK_a = 9.74$$

The reverse reaction rate for the above equilibrium has been measured with good agreement over a number of laboratories; however, the forward reaction rate is calculated based on the relationship between the reverse reaction rate and the equilibrium constant.[45] This equilibrium constant is derived from the Gibbs free energy of formation of $H^{\bullet}$ in the gas phase, combined with an estimated value for the free energy of solvation of $H^{\bullet}$. This estimation is a value between those for the free energy of solvation of He atoms and H_2 molecules.[8,88]

Both computational and experimental data show the same trend at pH 13 in that the production rate of hydrogen is less than that observed at lower pH, however the calculations once again overestimate the rate shown by the experimental data. Some more features of this discrepancy are discussed further in the following section.

Discussion

The radiolytic removal of hydrogen from solution by the hydroxyl radical has long been referred to as the Allen chain.[25] In this mechanism the hydroxyl radical reacts with molecular hydrogen to reform water and a hydrogen atom, the chain is then extended by the reaction of the hydrogen atom with hydrogen peroxide to reform the hydroxyl radical, with the net effect being the removal of H_2 and H_2O_2.

Propagation Steps:

$$^{\bullet}OH + H_2 \rightarrow H^{\bullet} + H_2O \qquad k_{78} = 4.0 \times 10^7\ M^{-1}\ s^{-1}$$

$$H^{\bullet} + H_2O_2 \rightarrow {}^{\bullet}OH + H_2O \qquad k_{11} = 3.65 \times 10^7\ M^{-1}\ s^{-1}$$

Termination:

$$H^{\bullet} + {}^{\bullet}OH \rightarrow H_2O \qquad k_{10} = 1.09 \times 10^{10}\ M^{-1}\ s^{-1}$$

Aside from transference into the gas phase, this chain is the only removal path for hydrogen under neutral pH conditions. At higher pH, radical species are converted into their base forms and a new chain is established.[43]

$$H^{\bullet} + OH^- \rightleftharpoons e_{aq}^- + H_2O \qquad \text{(R75/76)}$$

$$^{\bullet}OH + OH^- \rightleftharpoons O^{\bullet -} + H_2O \qquad \text{(R65/66)}$$

Propagation Steps:

$$O^{\bullet -} + H_2 \rightarrow e_{aq}^- + H_2O \qquad k_{47} = 1.28 \times 10^8\ M^{-1}\ s^{-1}$$

$$e_{aq}^- + HO_2^- \rightarrow O^{\bullet -} + OH^- \qquad k_{49} = 7.86 \times 10^8\ M^{-1}\ s^{-1}$$

Termination:

$$e_{aq}^- + O^{\bullet -} \rightarrow 2OH^- \qquad k_3 = 2.31 \times 10^{10}\ M^{-1}\ s^{-1}$$

Given the higher rate constants involved in the alkali chain, it would seem that the chain reaction established in the basic form has a higher efficiency than its neutral equivalent, yet observations show a higher chemical yield of hydrogen at high pH and would suggest otherwise. This can largely be resolved by considering the effects of oxygen on these chain reactions. Oxygen acts as a poison to both the chain reactions removing hydrogen, causing an increase in hydrogen yield. The mechanism by which oxygen disrupts the chain is through reactions with solvated electrons to produce superoxide which in turn reacts with OH radicals, or in the case of alkali solutions, $^{\bullet}O^{-}$, preventing them from reacting with hydrogen as well as reforming oxygen.

$$e_{aq}^{-} + O_2 \rightarrow O_2^{\bullet -} \quad \text{(R7)}$$

$$^{\bullet}OH + O_2^{\bullet -} \rightarrow OH^{-} + O_2 \quad \text{(R21)}$$

$$^{\bullet}O^{-} + O_2^{\bullet -} + H_2O \rightarrow 2OH^{-} + O_2 \quad \text{(R50)}$$

In alkali solution, $^{\bullet}O^{-}$ is also susceptible to a direct reaction with oxygen to form ozonide ions, while a neutral equivalent reaction between hydroxyl radicals and oxygen does not exist. As the experimental measurements of hydrogen gas from solutions of sodium hydroxide were carried out in deaerated conditions, there should be no initial dissolved oxygen and any oxygen present would have been radiolytically formed. Figure 41 shows the calculated steady state concentration of aqueous oxygen compared to hydrogen gas formation as a function of pH; from this it is clear that an increase in pH leads to a rise in radiolytically produced oxygen, which is proportional to the amount of hydrogen generated.

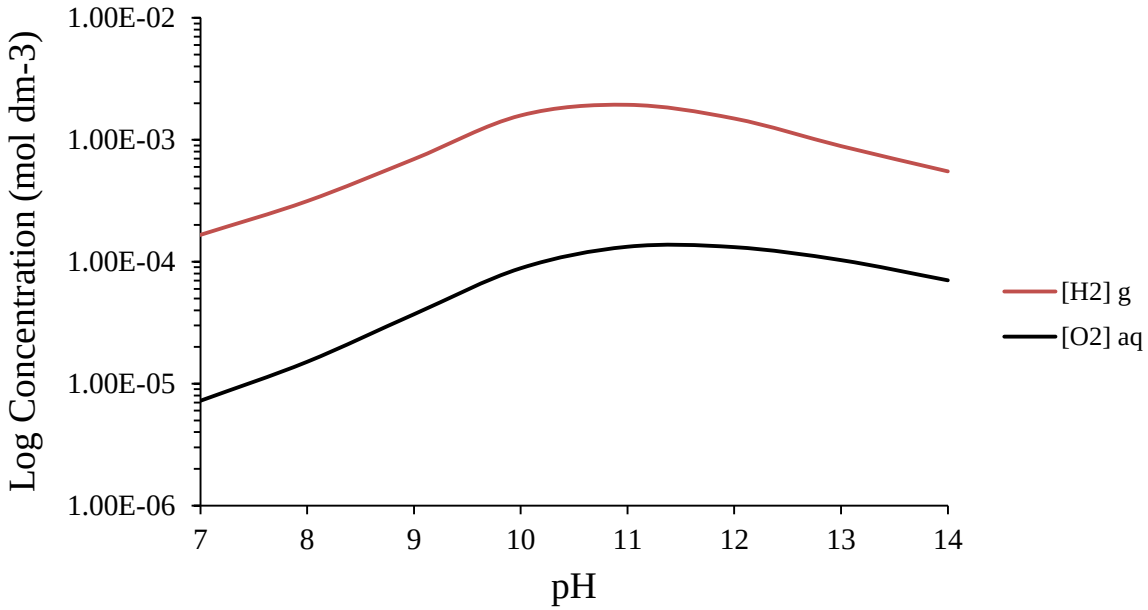

Figure 41: *Model calculations showing the concentrations of aqueous oxygen and hydrogen gas from deaerated water after 80 kGy at 280 Gy min^{-1}, to show the related behaviour between the two.*

Analysis of the calculated reaction rates gives an insight to why the concentration of radiolytic oxygen first rises with pH and then falls after pH 12 and may help to reveal the source of the over-prediction at pH 10.6. All the following reaction rates are taken from the end of the experimental range i.e. 80 kGy with a dose rate of 280 Gy min^{-1}. At neutral pH, it is the reaction between the superoxide ion and the hydroxyl radical (R21) that is the main source of radiolytic oxygen, but as the pH rises beyond pH 10 the rate of this reaction begins to fall, from ~1.40 ×10^{-6} mol dm^{-3} s^{-1} to 8.86 ×10^{-8} mol dm^{-3} s^{-1} at pH 14. This drop is mainly due to the equilibrium between the hydroxyl radical and its basic form, $^{\bullet}O^{-}$ which has a pK_a of 11.9. As one would expect, the reaction rate of the equivalent base reaction (R50) rises as the pH increases, although this increase does not fully compensate for the decrease in rate of R21.

This is because the reaction between the solvated electron and superoxide (R8) has a larger rate constant than R50 and with the conversion of hydrogen atoms to solvated electrons at high pH, R8 out competes R50.

In principal, many other reactions produce oxygen, but the rates of these reactions are often negligible. Only the rate of oxygen production through the reaction of superoxide and hydroperoxyl (R32) sees an increase over the pH range 10-12 which may be significant to radiolytic oxygen production. Figure 42 shows the rates of the three main molecular oxygen producing reactions (R21, R50, and R32), as well as the reaction rate for R8 and the combined reaction rates for R8 and R50, as a function of pH. When the combined reaction rates of R8 and R50 are compared with the reaction rate of R21, it becomes obvious that there is a transition from the removal of super oxide by R21 to removal by both R8 and R50; this is the main cause of a decrease in oxygen concentration after pH 12. Figure 43 shows the sum of reaction rates that lead to oxygen formation and removal as a function of pH.

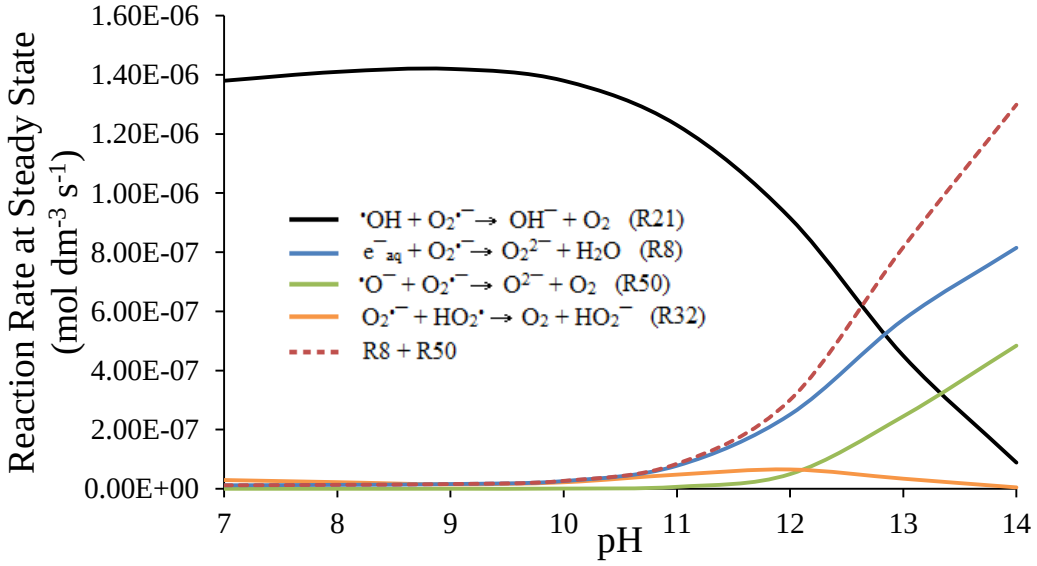

Figure 42: *Model predictions of the steady-state reaction rates of R21, R50, and R32 at various pH for γ radiolysis of deaerated water at a dose rate of 280 Gy min^{-1}.*

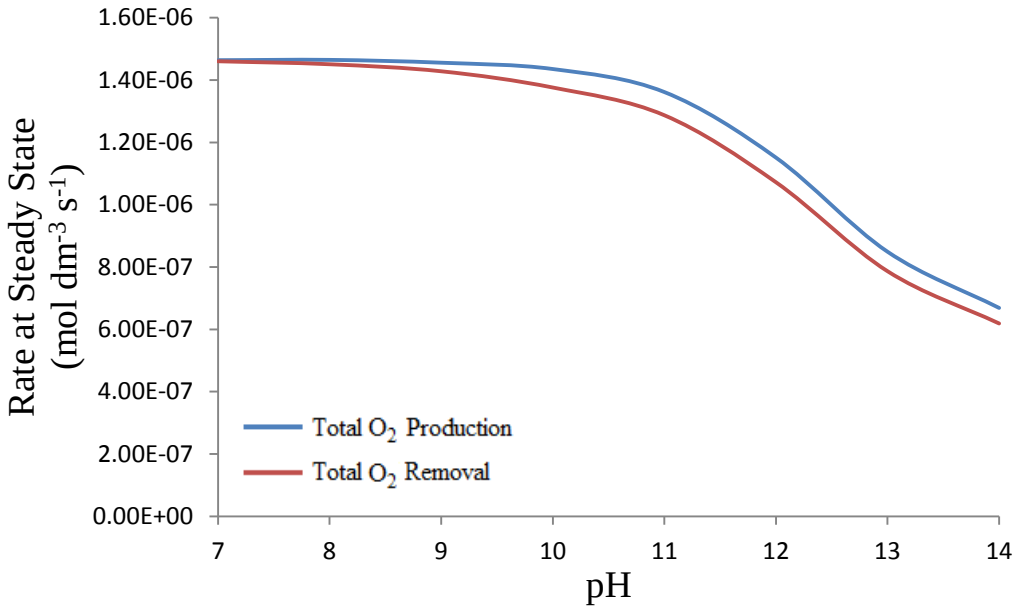

Figure 43: *The sum of the steady state rates of all reactions that produce O_2 (—) compared with the sum of the steady state rates of all reactions that remove O_2 (—). These totals do not include rates of production or removal from mass transfer reactions. This calculation is for the γ radiolysis of deaerated water to a dose of 80 kGy at a rate of 280 Gy min^{-1}.*

At pH 7 the rate of oxygen production matches the rate at which it is removed and a low steady state concentration of aqueous oxygen is achieved before the end of the 80 kGy calculation range. At higher pH the rate of oxygen removal diverges and so oxygen can accumulate to a higher concentration over a longer period of time; longer than that of the 80 kGy range used. Excluding transfer into the gas phase, there are only three reactions that effectively remove oxygen, so it was worth investigating how the rates of these reactions changed with pH. Figure 44 shows the rates of reactions R6, R7, R8, R12, and R67 as a function of pH.

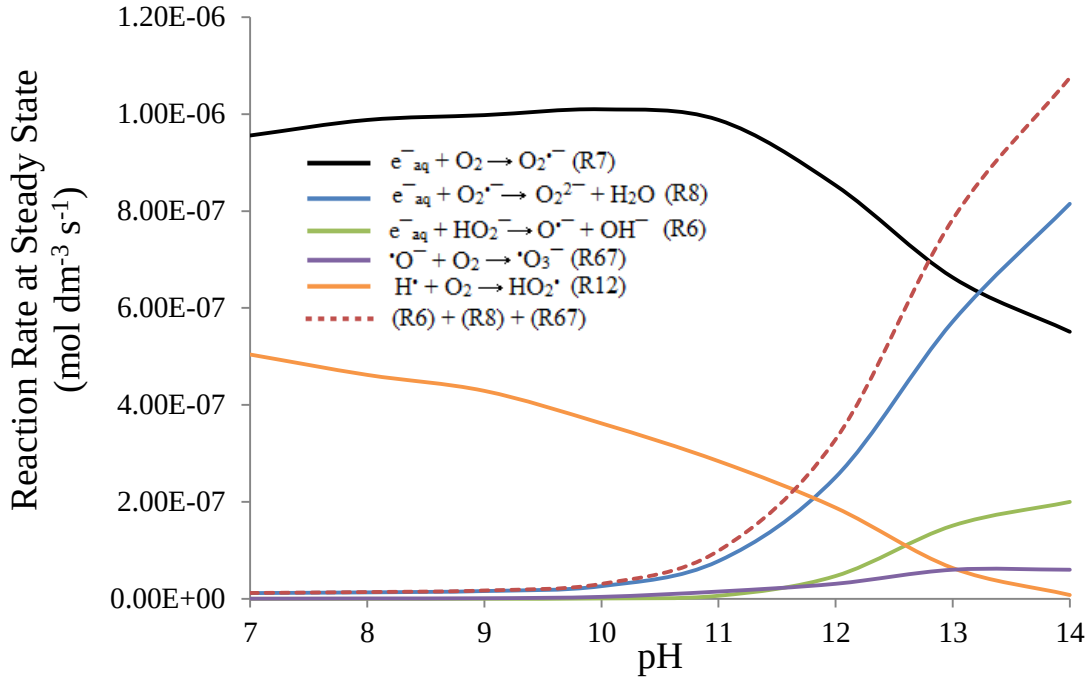

Figure 44: *Model predictions of the steady-state reaction rates of R7, R12, and R67 at various pH. This calculation is for the γ radiolysis of deaerated water to a dose of 80 kGy at a rate of 280 Gy min^{-1}.*

The first removal path of oxygen is the reaction between the solvated electron and oxygen to produce superoxide (R7), this reaction does not see a significant change in rate below pH 11, after which the rate begins to fall. The second reaction is the reduction of oxygen by the hydrogen atom (R12), the rate of this reaction falls steadily as pH increases; this is due to the conversion of hydrogen atoms to solvated electrons by hydroxide which has a pKa of 9.6. The decline in rate of this reaction, accompanied by no significant increase in the rate of oxygen removal by solvated electrons, may be the main contribution to the increased concentrations of oxygen at pH > 9. It was thought that this might also be the cause of the over prediction, but any attempt to increase this rate constant is largely negated by an accompanying increase in the rate of reaction R32. The final removal path of oxygen is the reaction with $O^{\bullet -}$ to form ozonide (R67).

The rate of this reaction increases rapidly with pH, from 1.94×10^{-8} mol dm^{-3} s^{-1} at pH 9 to 1.46×10^{-6} mol dm^{-3} s^{-1} at pH 14, however ozonide is unstable and decomposes to reform oxygen at a rate not much lower than its formation.

Subtracting the rate of oxygen reformation from the decomposition of ozonide gives the actual rate of oxygen removal by $^{\bullet}O^{-}$ of 1.10×10^{-9} mol dm^{-3} s^{-1} at pH 9 and 6.00×10^{-8} mol dm^{-3} s^{-1} at pH 14. It should be noted that the decomposition rate of ozonide was excluded from the total rate of oxygen formation in figure 44 while the rate of oxygen removal by ozonide formation was the subtracted values quoted above.

The main removal mechanism of hydrogen peroxide is by reaction with solvated electrons. In the presence of oxygen, the removal of hydrogen peroxide by solvated electrons is largely out competed by reactions between the solvated electrons and oxygen or superoxide. The rate constant for the reaction between oxygen and the solvated electron (R7) is 2.25×10^{10} dm^3 mol^{-1} s^{-1} while for the reaction of hydrogen peroxide and the solvated electron (R4) is only 1.36×10^{10} dm^3 mol^{-1} s^{-1} and so hydrogen peroxide is initially protected from reactions with the solvated electron as long as oxygen or superoxide is available. In alkali conditions where the pH is larger than 11.6, the conjugate base of hydrogen peroxide, HO_2^- becomes the dominant peroxide species. This reacts even slower with the solvated electron, with a rate constant of 3.65×10^9 dm^3 mol^{-1} s^{-1} so the protection effect is even stronger. It was mentioned earlier that beyond pH 11 the rate of reaction R21 falls significantly as $^{\bullet}OH$ is converted to its basic form and the equivalent base reaction (R50) does not see a sufficient equivalent increase in rate. The reason given was that R50 was out competed by the reaction between superoxide and the solvated electron (R8).

This not only serves to protect hydrogen peroxide by competing with solvated electrons but also contributes to the increased concentration of hydrogen peroxide as the product of R8 is in fact hydrogen peroxide.

$$e_{aq}^{-} + O_2^{\bullet -} \rightarrow O_2^{2-} \qquad \text{(R8)}$$

$$O_2^{2-} + H_2O \rightleftharpoons HO_2^{-} + OH^{-} \qquad \text{(R61/62)}$$

Although this may account for the increased steady state of hydrogen peroxide at high pH, Figure 39 still shows a slight over prediction for calculations made at pH 12.3 and 12.7. As the equilibrium between the hydroxyl radical and the oxygen anion has a pK_a of 11.84, it was thought that the over prediction could be a result of the estimations used for the rate constants of the reactions involving the oxide radical anion. There is little data available for the rate constants of reactions involving $^{\bullet}O^{-}$. As reaction R51 and R52 both lead to the formation of peroxide, it initially was thought that these reactions may have rate constants that are too high, however removing these reactions from the model made no significant difference to the predicted production of H_2O_2.

$$O^{\bullet -} + O^{\bullet -} \rightarrow O_2^{2-} \xrightarrow{H_2O} HO_2^{-} + OH^{-} \qquad \text{(R51)}$$

$$O^{\bullet -} + {}^{\bullet}OH \rightarrow HO_2^{-} \qquad \text{(R52)}$$

It was instead found that other oxide radical anion reactions had an effect on the predicted value for H_2O_2. A total of four oxide radical anion reactions influence the predicted values, with two of them making a significant difference. Reducing the rate constant for the reactions R47 and R48 made a slight improvement to the prediction of H_2O_2, a more significant effect can be seen by altering the rate constants for R49 and R50.

$$O^{\bullet-} + HO_2^- \rightarrow O_2^- + OH^- \quad \text{(R49)}$$

$$O^{\bullet-} + O_2^- \rightarrow \{O^{2-}\} \xrightarrow{H_2O} 2OH^- + O_2 \quad \text{(R50)}$$

Originally the rate constant for R49 was an estimation reported by Buxton et al in 1988[9] with a value of 4.0 ×10^8 M^{-1} s^{-1}. Since then, this rate constant has been measured by C. R. Stuart and D. C. Ouellette and is reported as being 7.86 ×10^8 M^{-1} s^{-1} at 25°C.[45] The value for the rate constant for R50 was originally estimated by Sehested *et al* in 1982[89] to be 6.0 ×10^8 M^{-1} s^{-1}. This estimation was made by adjusting the rate constant for R50 and R53 in a kinetic model, to produce a prediction that agreed with the decay of ozonide, measured experimentally by pulse radiolysis. By increasing the rate constant for R50 from 6.0 ×10^8 M^{-1} s^{-1} to 4.8 ×10^9 M^{-1} s^{-1} an improved agreement to the predicted steady state concentration of H_2O_2 is found. This is shown in Figure 45.

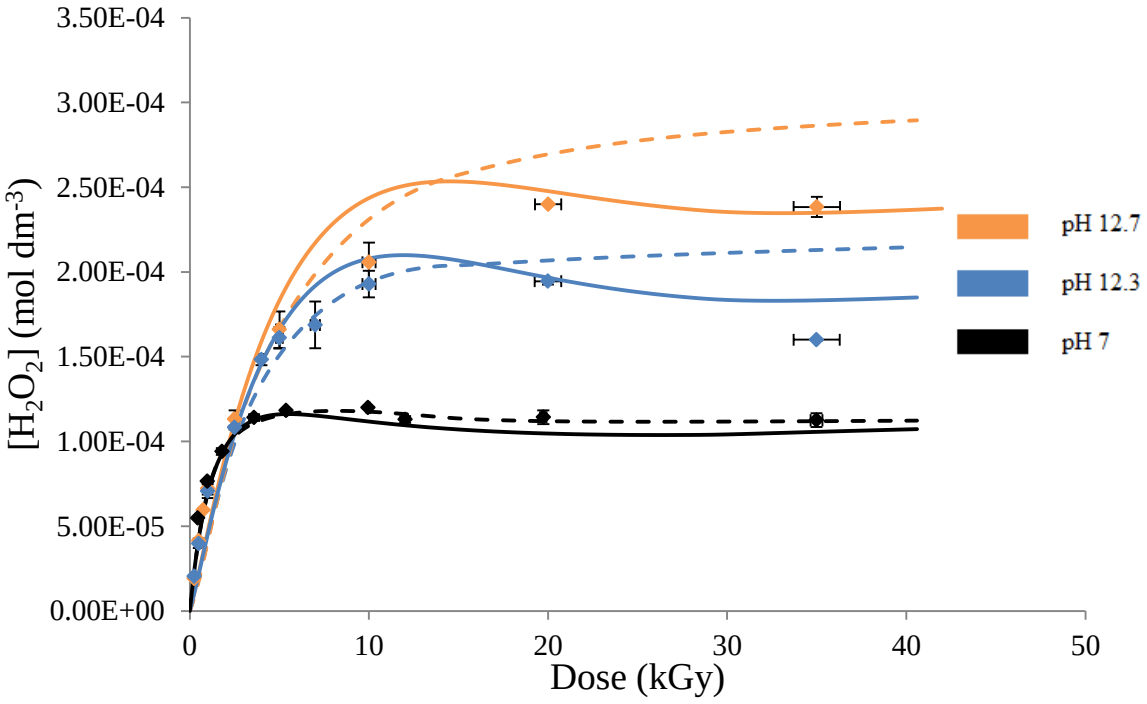

Figure 45: *Dashed lines show the original prediction where k_{50} = 6.0 ×10^8 M^{-1} s^{-1} while solid lines show the predictions with the increased k_{50} = 4.8 ×10^9 M^{-1} s^{-1}.*

With the modified reaction rate constant for R50, the predictions for the steady state concentrations of H_2O_2 are closer to the experimental values at high pH.

Although this calculation improves the prediction for the steady state concentration it also appears to increase the rate at which the steady state is achieved moving the prediction away from the experimental data. The cause of this discrepancy may have something to do with the way in which some of the equilibria have been implemented in the model and should be investigated in the future. This modification also has little effect on the over prediction of hydrogen gas at pH 10.4.

Chapter 5: Radiolysis of Magnesium Hydroxide

Context

The Magnox Swarf Storage Silo contains 22 silos used to store magnesium alloy cladding that has been removed from spent Magnox fuel elements. The magnesium fuel cladding is stored underwater where it readily corrodes to form magnesium hydroxide and hydrogen gas by the following reaction.[90]

$$Mg + 2H_2O \rightarrow Mg(OH)_2 + H_2$$

Hydrogen gas poses an obvious hazard and is closely monitored, however, production rates are not predictable. Much of the magnox fuel cladding is contaminated with uranium and other fission products, contributing an additional supply of hydrogen through water radiolysis. Dose rates are often further increased as some of the silos were used to dispose of other beta and gamma emitting waste. The presence of the magnesium hydroxide complicates the radiolysis processes as (a low) solubility in water drives up the pH, while undissolved magnesium hydroxide provides additional surfaces where radiolysis processes are poorly understood.

Experiments were conducted to investigate the effects of magnesium hydroxide on the radiolytic production yields of hydrogen gas and hydrogen peroxide. The investigation began by measuring hydrogen yields in solutions of magnesium hydroxide and comparing hydrogen yields to solutions containing sodium hydroxide solution with the same pH. Pure water is also included as a control and the magnesium hydroxide samples included both homogeneous saturated solutions of aqueous magnesium hydroxide and heterogeneous slurries containing undissolved magnesium hydroxide.

Method

The saturated solution was prepared in bulk using magnesium hydroxide (Sigma Aldrich BioUltra ≥ 99.0%) and ultra-pure water; solids were separated by centrifuge as filters may introduce organic contamination. 2 mL aliquots of saturated magnesium hydroxide solution were transferred to sample tubes and flame sealed under air. The pH of the remainder of the saturated solution was measured to be 10.6. Slurry samples were prepared by weighing 0.1 g of magnesium hydroxide into a glass vial before adding 2 mL of ultra-pure water. Samples were also flame sealed under air before being mechanically mixed by agitation. Samples were irradiated using the inverter rig; however the samples were left stationary and were not inverted during irradiation. Samples were irradiated at an average dose rate of 281 Gy min^{-1} until the desired dose was reached, samples were then analysed for hydrogen by the "crush tube" gas chromatography method previously described. Figure 46 shows the production of hydrogen as a function of dose for both saturated solutions, and solid containing slurries of magnesium hydroxide. This is compared with measurements obtained from pure water and an aqueous solution of sodium hydroxide with a similar pH to that of the magnesium hydroxide samples.

Results

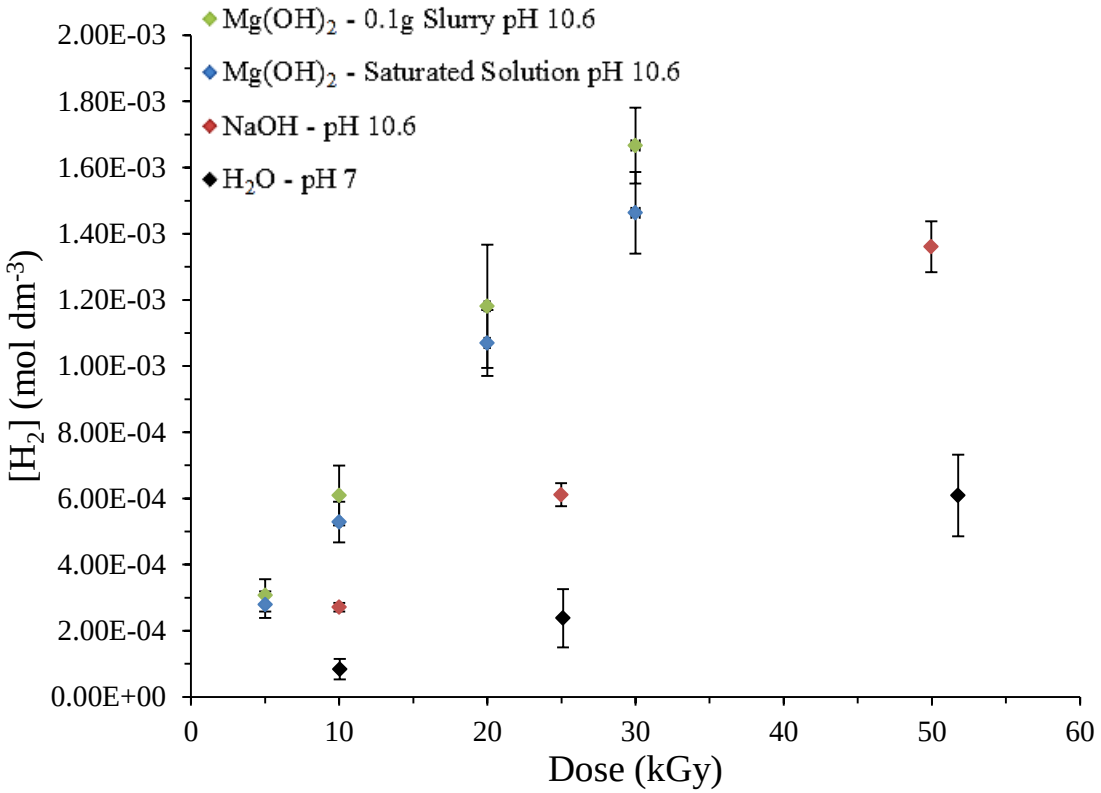

Figure 46: *Measurements of H_2 gas as a function of dose. All samples here are aerated with vertical error bars showing the standard deviation between replicates.*

It should be noted that all the samples used to produce figure 46 are aerated. The chemical yield of hydrogen for each sample set is given in Table 20.

Sample ID	Average Dose Rate for Inverter Rig (Gy min^{-1})	Measured pH	G(H_2) (Molecules 100 eV^{-1})	Error ±
$Mg(OH)_{2(s)}$	281.4	10.62	0.52	0.03
$Mg(OH)_{2(aq)}$	281.4	10.57	0.47	0.02
NaOH	284.5	10.63	0.27	0.02
H_2O	173.2	6.99	0.16	0.01

Table 20: *Obtained results from the measurements of H_2 gas.*

The dose rate for the pure water samples is much lower than the other dose rates quoted; as this measurement was performed before the construction of the inverter rig and so the samples were held further away from the source during irradiation.

This data shows that the presence of magnesium hydroxide appears to increase the hydrogen yield beyond what one would expect if the yield was controlled by pH alone. There is very little difference in hydrogen yield between samples that contain solid magnesium hydroxide and samples that contain only dissolved magnesium hydroxide. This suggests that surface effects contribute to the hydrogen yield only a very small amount or not at all. This data is discussed further in the following section.

A second set of experiments was conducted to measure the concentration of hydrogen peroxide in irradiated saturated solutions of magnesium hydroxide. 10 mL aliquots of aerated saturated solution were transferred in to 20 mL glass headspace vials, the vials were sealed with an aluminium crimp cap and irradiated in the front row of the 4 x 8 rack, the average dose rate was 283.1 Gy min^{-1}. After irradiation the samples were analysed for hydrogen peroxide by the Ghormley tri-iodide method described in Chapter 2. Figure 47 compares the obtained data from this experiment with data obtained from measurements made in pure water.

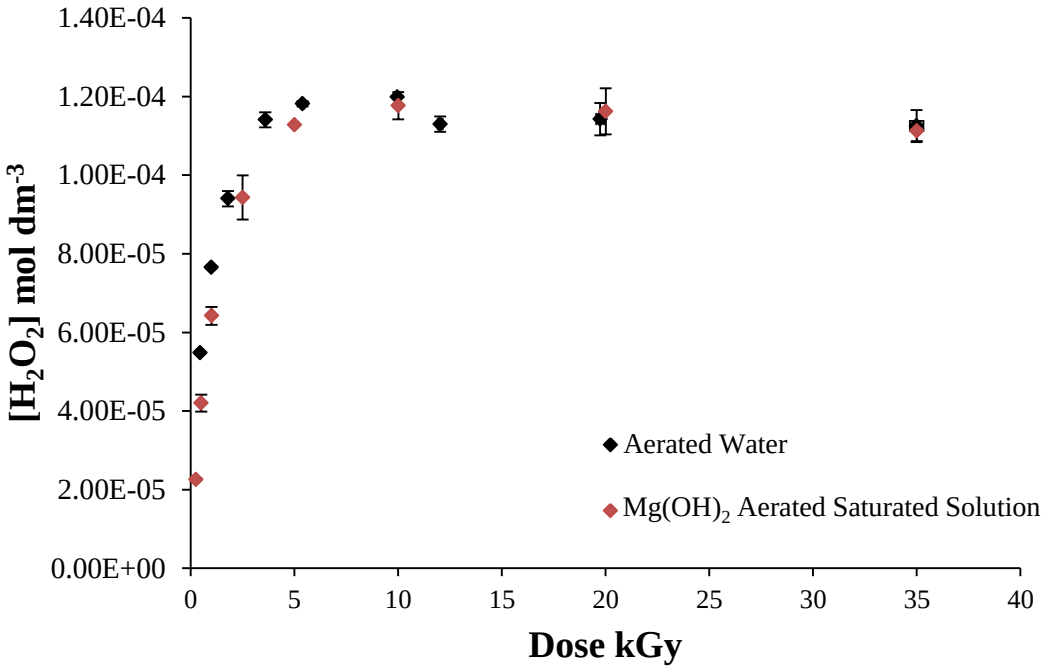

Figure 47: *Measurements of H_2O_2 concentrations in aerated samples of saturated magnesium hydroxide solution as a function of dose.*

The steady state concentration of hydrogen peroxide in a saturated solution of magnesium hydroxide is almost the same as in a neutral sample of pure water, as is expected given the pH of the saturated solution was measured to be 10.6, which is below the 11.8 threshold that is associated with an increased steady state of hydrogen peroxide, observed in the previous chapter.

A further experiment was conducted to investigate the effects of the solid magnesium hydroxide surface on the production of hydrogen. Batches of samples were prepared with various ratios of magnesium hydroxide to water, each sample had a total mass of approximately 2 g, Table 21 summarises the sample ratios used. Samples were irradiated using the inverter rig which was left stationary throughout the irradiation; the average dose rate was 304.2 Gy min^{-1}. All samples were irradiated to approximately 52.5 kGy so that any difference in the amount of hydrogen produced is independent of absorbed dose.

As the dose rate was determined by Fricke dosimetry, which is a liquid phase dosimeter with a density close to that of water, the quoted dose of 52.5 kGy is what was received by the aqueous phase. The solid phase magnesium hydroxide has a slightly higher density and will have received a slightly higher dose. Figure 48 shows the chemical yields of hydrogen as a function of water content percentage. The results have been normalised to reflect the amount of hydrogen produced per gram of water and the yields were calculated based on the radiation dose absorbed by the whole system, this makes the data from samples that contain large quantities of water comparable to those with lower water content.

H2O %	Average $Mg(OH)_2$ Mass (g)	Average H_2O Mass (g)	Average Dose (kGy)
4[a]			53.03 ± 1.11
20	1.61 ± 0.02	0.40 ± 0.01	52.45 ± 1.46
40	1.22 ± 0.02	0.82 ± 0.01	52.55 ± 1.46
60	0.81 ± 0.01	1.22 ± 0.01	52.55 ± 1.45
80	0.40 ± 0.01	1.62 ± 0.02	52.45 ± 1.45
100[b]			52.39 ± 1.45

Table 21: *Conditions of samples containing $Mg(OH)_2$ for measurements of H_2.*
a – Powder sample with no added water, estimated adsorbed water content is based on data from Nelson et al[91]
b – Sample is a saturated solution of $Mg(OH)_2$ i.e. contains no solid.

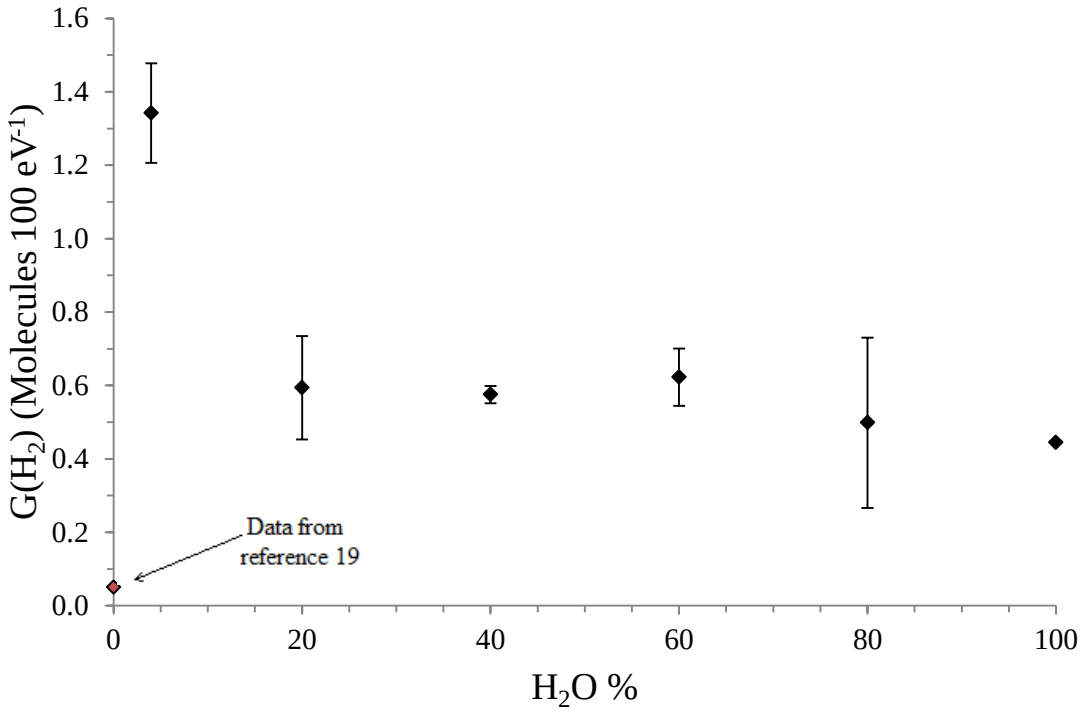

Figure 48: *Measurements of hydrogen yields from magnesium hydroxide samples with various solid – aqueous ratios. All samples were irradiated to a total dose of ~52 kGy to the aqueous phase, at a dose rate of 304.1 Gy min^{-1}.*

Discussion

The data shown in Figure 46 suggests that the presence of dissolved magnesium hydroxide increases the chemical yield of hydrogen significantly more than if pH was the only controlling factor. Data shown in Figure 48 suggests that the presence of the solid surface increases the hydrogen yield slightly above that for saturated solutions, but it would seem that the main contribution to the increased H_2 yields in magnesium hydroxide samples, when compared to a solution of NaOH of equivalent pH, is a factor present in both slurries and saturated solutions of magnesium hydroxide. The yield of H_2 between 20 and 80 percent water content is not affected by changing the solid : solution ratio, suggesting that there is little interaction between the solid magnesium hydroxide and the bulk water.

The yield is significantly higher for samples with 4% water content (adsorbed water), suggesting that any additional hydrogen is produced only in a few water layers away from the solid surface, as has been postulated for oxide surfaces.

Petrik *et al*, showed that oxide water systems consisting of multiple phases, such as the slurry samples measured here, have different hydrogen yields, depending on the oxide.[18] They grouped materials into three categories based on the effects they have on measured hydrogen yields; hydrogen enhancing, hydrogen diminishing, and hydrogen neutral. Though said study did not include magnesium hydroxide, it does categorise magnesium oxide as a material that does not significantly change the yield of hydrogen.

The mechanism by which a solid surface increases the hydrogen yield is largely accredited to an energy transfer process. As solid particles in a sample absorbs energy, a process of energy migration from the bulk of the material to the interface takes place. Energy can then be transferred from the solid phase to the surrounding liquid. The exact mechanism of the energy transfer process is not well understood, but the overall effect is higher dose rates in localised areas of surrounding water.

As the value of 4% water content, is an estimation based on data extrapolation published by Nelson *et al*, in a study of water adsorption on magnesium hydroxide,[91] and may not be entirely accurate. This uncertainty could have a significant effect on the calculated chemical yield if the estimation was even slightly incorrect, for example an estimated water content of just 9 % has the effect of lowering the yield to the same value observed in samples contain 20 % water content. This would be contradictory to an energy transfer process as described previously.

A study by Jay La Verne et al, published measurements of hydrogen yields from the gamma radiolysis of magnesium hydroxide to be 0.051.[19] This measurement was made using magnesium hydroxide that had been dried to remove all excess water while remaining hydroxylated. The difference between the measured yields of saturated magnesium hydroxide solution ($G(H_2) = 0.47$) and a slurry sample ($G(H_2) = 0.52$), given in Table 20, is 0.05.

This value is very close to the quoted value from dry magnesium hydroxide, although it is an average value and errors can be high with small differences between large numbers such as this. Little information is given to explain the mechanism contributing to this yield of hydrogen from dry magnesium hydroxide, other that the radiation induced conversion of magnesium hydroxide to magnesium oxide.[92] A comparison was made to yields obtained from calcium hydroxide and found that the yield of hydrogen was four times higher from calcium hydroxide than from magnesium hydroxide. This was explained in terms of the tendency to form water during radiolysis being greater in magnesium hydroxide than in calcium hydroxide, meaning that a smaller portion of the hydroxide generates hydrogen directly. If the yield measured from the dry powder (0.051) by La Verne *et al*, is the result of direct hydrogen production from magnesium hydroxide converting to the oxide, then it would make sense that the difference in yield between samples containing solid magnesium hydroxide and only aqueous magnesium hydroxide, would be close to this value.

This does not explain why the yields of both samples are far higher than samples of sodium hydroxide at the same pH as the magnesium hydroxide samples. The chemical yield of hydrogen from samples of sodium hydroxide with a pH of 10.63 was 0.27, while yields from both magnesium hydroxide systems were a little less than double this value.

As this can be seen in both aqueous only samples and those containing solid magnesium hydroxide, the cause of this increased yield must be attributed to a factor present in both aqueous only samples and samples containing solid magnesium hydroxide. Magnesium hydroxide is often discussed in literature concerning environmental science for its properties and reactivity towards carbon dioxide.[93,94]

As the samples used in these experiments did not undergo any purification processes prior to use, they were most likely subject to carbonation reactions with atmospheric carbon dioxide and water. Magnesium hydroxide can be carbonated on exposed surfaces, although slow at standard room conditions, it can be increased in the presence of water.[95]

$$Mg(OH)_{2(s)} + CO_{2(g)} \rightarrow MgCO_{3(s)} + H_2O_{(g)}$$

Magnesium hydroxide can also take on intercalated carbon dioxide which can be converted to carbonate either by reaction with water or, if released into solution, with hydroxide to form bicarbonate.[96,97]

$$CO_{2(Air)} \rightleftharpoons CO_{2(interlayer)}$$

$$CO_{2(interlayer)} + H_2O_{(interlayer)} \rightleftharpoons 2H^+_{(interlayer)} + CO^{2-}_{3(interlayer)}$$

$$CO_{2(aq)} + OH^-_{(aq)} \rightleftharpoons HCO^-_{3(aq)}$$

Both carbonate and bicarbonate are known to be hydroxyl radical scavengers in the radiolysis of aqueous solutions.[9,98] Using the Facsimile model described in Chapter 3, it was possible to insert a set of reactions concerning carbonate radiolysis to estimate the effects that small quantities of carbonate might have on hydrogen yields.

The reaction set used is described in Table 22 and represents a simplified reaction scheme of carbonate in aqueous radiolysis. Initial concentrations of carbonate were set ranging from 1.0 μM to 10 mM, a yield of hydrogen was calculated for each initial concentration; these calculations have been graphed in Figure 49.

In each case, the calculated production of hydrogen was linear over the dose range used, which would be a necessary feature if carbonate is to be a valid explanation for the increased yields observed in magnesium hydroxide experiments. The calculated yield of hydrogen increases rapidly with only small quantities of initial carbonate before reaching a plateau at about $G(H_2) = 0.3$ with an initial carbonate concentration of 50 μM. The hydrogen yield did not change much more than this, increasing to just $G(H_2) = 0.36$ with an initial carbonate concentration of 10 mM. The effect is almost the same in calculations for both aerated and deaerated solutions. It should be noted that these calculations were done at pH 7 due to the systematic error of over prediction when the pH is close to 10; it would be unadvisable to trust such calculations without first solving the error (see previous chapter).

Reaction	Rate Constant	Reference
$CO_3^{2-} + {}^{\bullet}OH \rightarrow CO_3^{-} + OH^{-}$	3.9×10^8	9
$CO_3^{2-} + e^{-}_{aq} \rightarrow$ products	3.9×10^5	99
$CO_3^{\bullet-} + {}^{\bullet}OH \rightarrow$ products	3.0×10^9	100
$CO_3^{\bullet-} + H_2O_2 \rightarrow HCO_3^{-} + HO_2^{\bullet}$	4.3×10^5	101
$CO_3^{\bullet-} + HO_2^{-} \rightarrow HCO_3^{-} + O_2^{\bullet-}$	3.0×10^7	101
$CO_3^{\bullet-} + O_2^{\bullet-} \rightarrow O_2 + CO_3^{2-}$	6.5×10^8	102
$HCO_3^{-} + e^{-}_{aq} \rightarrow$ products	1.0×10^6	103
$HCO_3^{-} + {}^{\bullet}OH \rightarrow H_2O + CO_3^{\bullet-}$	8.5×10^6	9
$HCO_3^{-} + H^{\bullet} \rightarrow$ products	4.4×10^4	104

Table 22: *A reaction scheme to estimate the effect of carbonate in water radiolysis.*

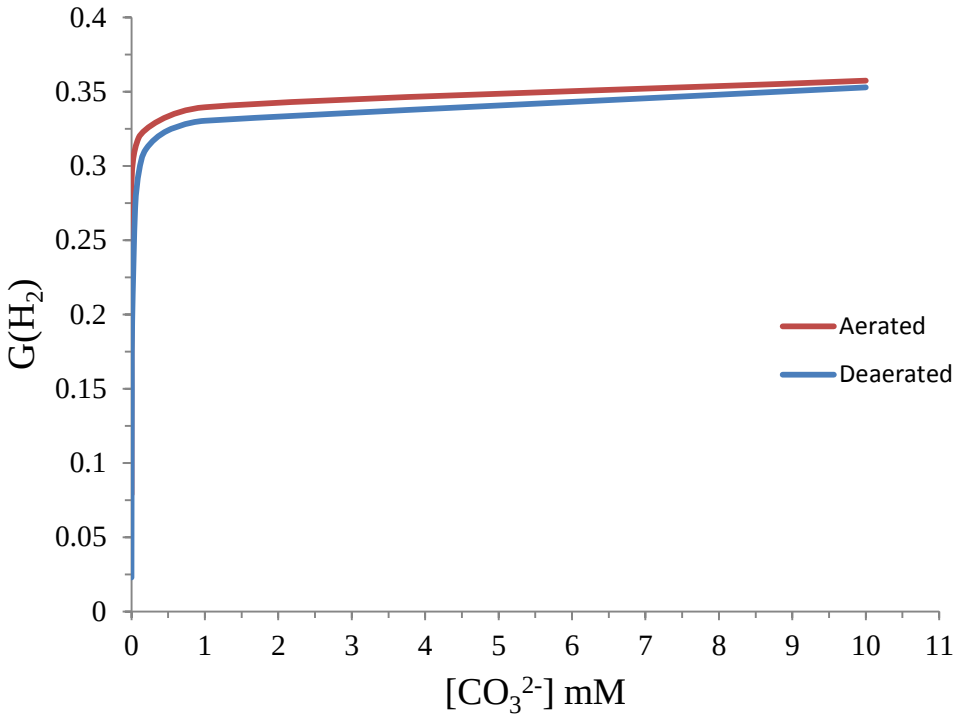

Figure 49: *Model predictions for the yield of H_2 from a solution containing various concentrations of carbonate anions.*

Reaction rate analysis of the calculations reveals that the main mechanism for hydrogen protection is through a cooperative effect of scavenging of the hydroxyl radical to form a carbonate radical. The majority of carbonate radicals are converted back to carbonate by reaction with superoxide. A secondary process of carbonate radical reactions with hydrogen peroxide contributes slightly to regeneration of superoxide as well as forming bicarbonate which itself contributes to hydrogen protection by scavenging hydroxyl radicals, once again forming a carbonate radical. As these calculations were performed at pH 7, it is uncertain what effect an elevated pH would have on the predicted hydrogen yield. It should also be remembered that many of the rate constants used are estimations, and the reaction set is a simplification and is not a comprehensive description.

With these factors in mind, the predicted behaviour of hydrogen production is a reasonable representation of the behaviour observed in experiments. This could easily be investigated further by experiments in a number of ways.

Attempts could be made to measure carbonate directly from the magnesium hydroxide used, either by thermogravimetric analysis (TGA) or by total organic carbon analysis (TOC). Radiolysis experiments of other carbonates could also be carried out to further investigate the effect of carbonate.

Chapter 6: Radiolysis of Methanol Solutions

Context

Many of the waste storage ponds at Sellafield Ltd are open to the air, and are subject to organic matter falling in and decomposing to a range of organic products. One particular group of compounds known as humic acids, and how they might affect radiolysis processes in the ponds, are of particular interest. Humic acids are ill-defined but complex organic acids with several different functional groups which will have many effects on radiolysis. The best approach to investigating this chemistry is to understand the effects of each functional group independently before building up to a full humic acid analogue. This study takes the first steps towards this investigation through experimentation on aqueous solutions of methanol.

Experimental Method

A stock aqueous solution of 1 mM methanol was made and was used to prepare aerated samples of 10 mL, sealed by crimp cap in 20 mL headspace vials so that the liquid to headspace ratio was 1:1. Samples were irradiated in row 2 of the 4x8 irradiation rack for various periods of time. The average dose rate was 163.8 Gy min^{-1}. The samples were analysed for hydrogen peroxide immediately after irradiation using the Ghormley tri-iodide method described in Chapter 2. A separate batch of aerated samples was prepared from the 1 mM methanol stock solution for analysis of hydrogen generation. These were samples of 2 mL of 1 mM methanol and were deaerated using zero grade argon gas before being sealed in glass tubes designed for use by the crush tube analysis method described in Chapter 2. Again the samples had a liquid to headspace ratio of 1:1.

These samples were irradiated in the centre positions of row 2 in the 4x8 rack where the average dose rate was 175.5 Gy min^{-1}.

Results

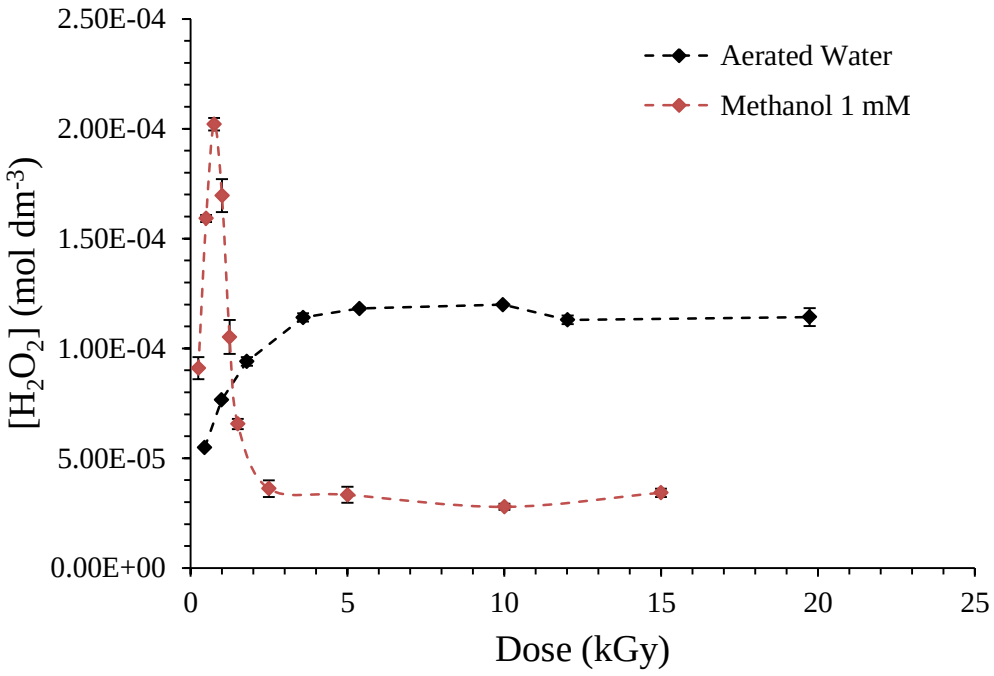

Figure 50: *Measurements of H_2O_2 concentrations as a function of dose in samples containing 1 mM methanol (♦) and water as a control (♦). All samples were aerated and a dashed line is included to highlight the data trend. The dose rate was 163.8 Gy min^{-1} for methanol solutions and 283.9 Gy min^{-1} for the aerated water.*

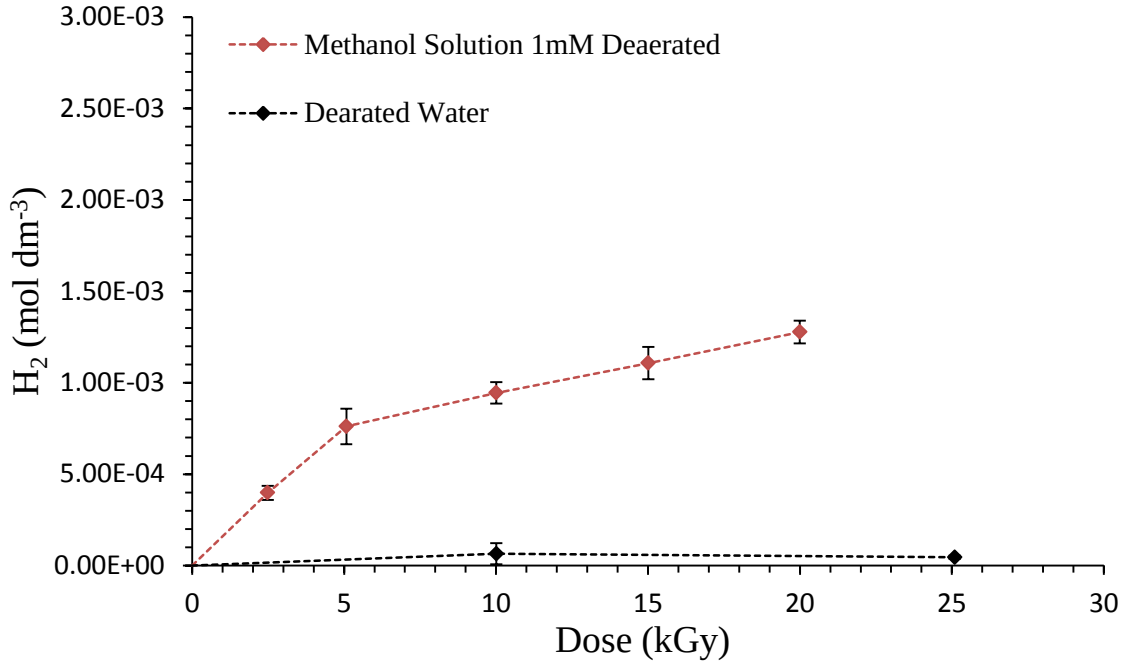

Figure 51: *Measurements of H_2 gas as a function of dose from deaerated samples containing 1 mM methanol, deaerated water is also shown as a control. Dashed lines are included to highlight the data trend. The dose rate was 175.5 Gy min^{-1} for the methanol solutions and 285.1 Gy min^{-1} for the deaerated water.*

Figure 50 shows the measured concentrations of hydrogen peroxide from the 1 mM methanol solution compared with the measured concentrations from pure aerated water. At low doses, the concentration of hydrogen peroxide increases rapidly to approximately 2.0×10^{-4} mol dm^{-3} at approximately 1 kGy, which is almost double the steady state concentration observed in pure water. As the dose increases further, the concentration begins to fall to a steady state value at approximately 3.3×10^{-5} mol dm^{-3}.

Figure 51 shows the measured hydrogen concentrations from the 1 mM methanol solutions; compared with hydrogen measurements from aerated water.

Hydrogen concentrations measured in a deaerated 1 mM methanol solution are significantly higher than those measured in deaerated water: the initial production rate is higher in the methanol solution, but production is not linear and the rate of hydrogen production with dose soon falls. The change in production rate of hydrogen and hydrogen peroxide with dose can be shown by converting the experimental measurements to G-values and plotting them as a function of dose. Figures 52 and 53 show the chemical yields determined by converting the gradients between 0 and each data point to units of molecules 100 eV^{-1}.

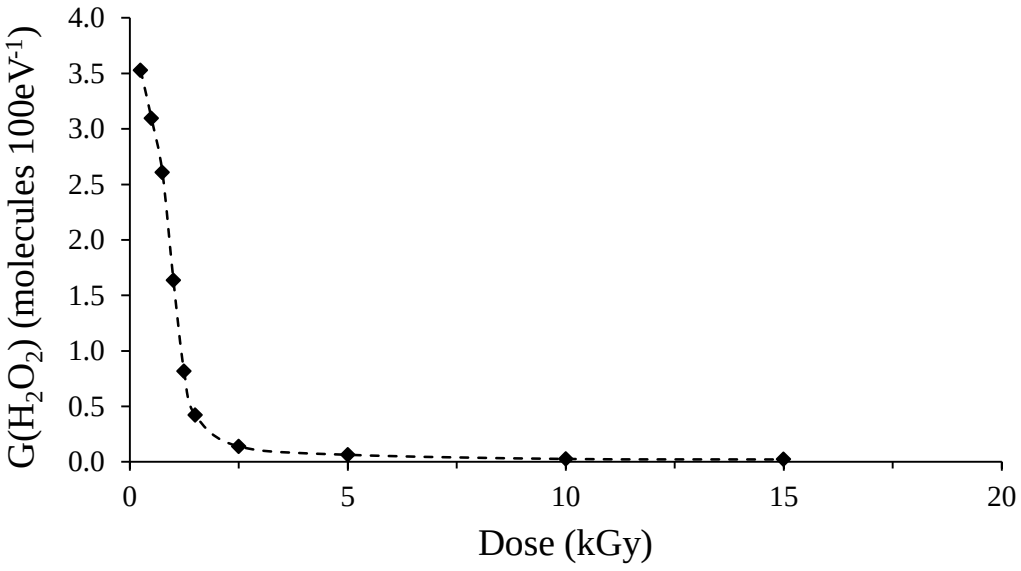

Figure 52: *Chemical yields of hydrogen peroxide measured from an aerated solution of 1 mM methanol as a function of dose.*

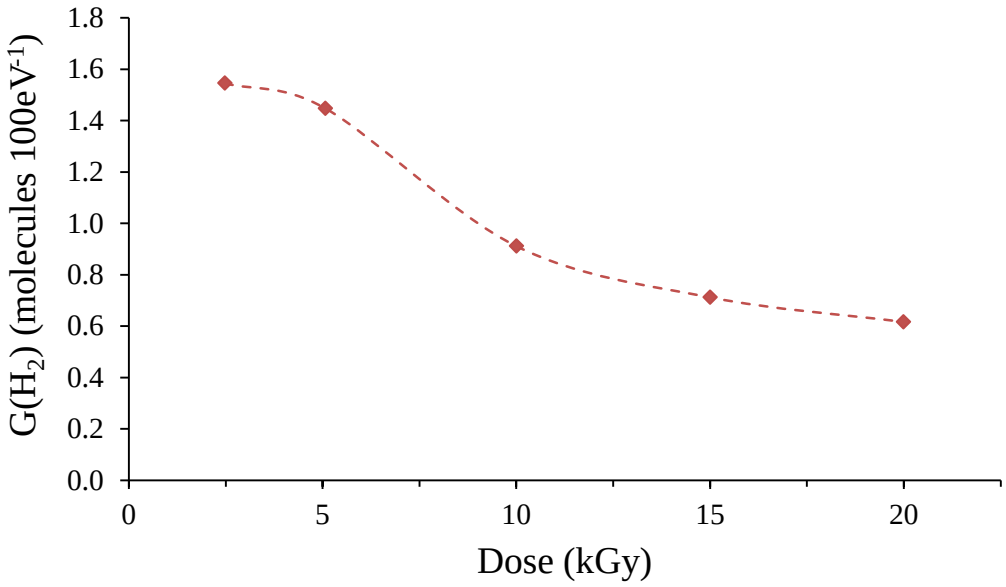

Figure 53: *Chemical yields of hydrogen gas measured from a deaerated solution of 1 mM methanol as a function of dose.*

Discussion

Most alcohols are effective scavengers of hydroxyl radicals and hydrogen atoms. The reactions between methanol and hydroxyl radicals or hydrogen atoms result in hydrogen abstraction from methanol to form water or molecular hydrogen respectively, and in both cases form the hydroxymethyl radical.[105,106]

$$^{\bullet}OH + CH_3OH \rightarrow H_2O + {}^{\bullet}CH_2OH \quad k = 8.3 \times 10^8\ M^{-1}s^{-1}$$

$$H^{\bullet} + CH_3OH \rightarrow H_2 + {}^{\bullet}CH_2OH \quad k = 2.8 \times 10^6\ M^{-1}s^{-1}$$

Although the second order rate constant for the reaction between methanol and the solvated electron is faster than that for the solvated electron and water, the reaction rate does not compete with the rate of reaction between the solvated electron and water until the concentration of methanol is greater than 10^{-2} M.[2,107]

In deaerated water, methanol radicals may dimerise to form ethylene glycol or disproportionate to form formaldehyde and reform methanol.[108] They may also react with hydrogen peroxide to form formaldehyde.

$$2^{\bullet}CH_2OH \rightarrow (CH_2OH)_2$$

$$2^{\bullet}CH_2OH \rightarrow CH_3OH + HCHO$$

$$^{\bullet}CH_2OH + H_2O_2 \rightarrow HCHO + H_2O + {}^{\bullet}OH$$

In solutions that contain dissolved oxygen, such as those used in the measurements of hydrogen peroxide (Figure 50), methanol radicals rapidly react with oxygen to form an organic peroxyl radical which reacts by second-order processes resulting in the formation of formaldehyde, hydrogen peroxide, and oxygen.[109]

$$^{\bullet}CH_2OH + O_2 \rightarrow {}^{\bullet}O_2CH_2OH$$

An additional set of reactions were included in the water radiolysis model described in Chapter 3, in an attempt to model the radiolysis chemistry of an aqueous solution of 1 mM methanol. This reaction scheme is shown in Table 23.

Reaction Number	Reaction	Rate Constant at 25°C (M^{-1} s^{-1})	Ref
M1	$CH_3OH + {}^{\bullet}OH \rightarrow H_2O + {}^{\bullet}CH_2OH$	8.3×10^{8}	110
M2	$CH_3OH + H^{\bullet} \rightarrow H_2 + {}^{\bullet}CH_2OH$	2.8×10^{6}	106
M3	${}^{\bullet}CH_2OH + O_2 \rightarrow {}^{\bullet}O_2CH_2OH$	4.9×10^{9}	111
M4	${}^{\bullet}CH_2OH + H_2O_2 \rightarrow H_2O + H_2CO + {}^{\bullet}OH$	1.8×10^{5}	112
M5	${}^{\bullet}CH_2OH + {}^{\bullet}CH_2OH \rightarrow CH_3OH + H_2CO$	1.2×10^{9}	2,113
M6	${}^{\bullet}CH_2OH + {}^{\bullet}CH_2OH \rightarrow HOCH_2CH_2OH$	1.2×10^{9}	2,113
M7	${}^{\bullet}CH_2OH + {}^{\bullet}OH \rightarrow H_2CO + H_2O$	[a]2.4×10^{10}	114
M8	${}^{\bullet}O_2CH_2OH + {}^{\bullet}O_2CH_2OH \rightarrow 2H_2CO + H_2O_2 + O_2$	7.4×10^{8}	115
M9	${}^{\bullet}O_2CH_2OH + {}^{\bullet}HO_2 \rightarrow H_2CO + H_2O_2 + O_2$	[b]5.0×10^{8}	2
M10	${}^{\bullet}O_2CH_2OH + O_2^{-} \rightarrow H_2CO + HO_2^{-} + O_2$	[b]5.0×10^{7}	2
M11	$HOCH_2CH_2OH + {}^{\bullet}OH \rightarrow {}^{\bullet}HOCHCH_2OH + H_2O$	2.4×10^{9}	116
M12	$HOCH_2CH_2OH + H^{\bullet} \rightarrow {}^{\bullet}HOCHCH_2OH + H_2$	1.4×10^{7}	9
M13	${}^{\bullet}HOCHCH_2OH + O_2 \rightarrow {}^{\bullet}O2HOCHCH2OH$	3.2×10^{9}	111
M14	${}^{\bullet}O2HOCHCH2OH \rightarrow HOCH_2CHO + H^{+} + O_2^{-}$	1.9×10^{2} s^{-1}	117
M15	${}^{\bullet}HOCHCH_2OH + {}^{\bullet}HOCHCH_2OH \rightarrow HOCH_2CH_2OH + HOCH_2CHO$	9.6×10^{8}	118
M16	$HOCH_2CHO + {}^{\bullet}OH \rightarrow H_2O + {}^{\bullet}HOCHCHO$	[c]9.2×10^{6}	119
M17	${}^{\bullet}HOCHCHO + {}^{\bullet}HOCHCHO \rightarrow HOCH_2CHO + OCHCHO$	[d]5.0×10^{4}	-
M18	$OCHCHO + {}^{\bullet}OH \rightarrow H_2O + {}^{\bullet}OCCHO$	1.4×10^{6}	120
M19	${}^{\bullet}OCCHO \rightarrow CO + HCO^{\bullet}$	[a]3.5×10^{7} s^{-1}	121
M20	$H_2CO + e^{-}_{aq} \rightarrow {}^{\bullet}CH_2OH + OH^{-}$	1.0×10^{6}	2
M21	$H_2CO + H^{\bullet} \rightarrow H_2 + HCO^{\bullet}$	5.0×10^{6}	2
M22	$H_2CO + {}^{\bullet}OH \rightarrow H_2O + HCO^{\bullet}$	2.0×10^{9}	2
M23	$HCO^{\bullet} + H^{\bullet} \rightarrow H_2 + CO$	[a]6.8×10^{10}	122
M24	$HCO^{\bullet} + {}^{\bullet}OH \rightarrow CO + H_2O$	[a]1.1×10^{11}	123
M25	$HCO^{\bullet} + O_2 \rightarrow CO + HO_2^{\bullet}$	[a]3.1×10^{9}	124
M26	$HCO^{\bullet} + HCO^{\bullet} \rightarrow 2CO + H_2$	[a]2.2×10^{10}	125

Table 23: *A reaction scheme to estimate the effect of methanol in water radiolysis*
a – Rate constant for gas phase reaction
b – Estimated rate constant
c – Rate constant based on reaction of acetic acid and hydroxyl
d – Assumed reaction

Figure 54 shows the predicted hydrogen peroxide concentration with the above chemistry included in the calculation and compares it with the experimental data. In order to achieve the agreement shown, a modification to the mass transfer routine was required.

The current implementation of the mass transfer routine does not cope with a rapid depletion of dissolved oxygen and responds by increasing the rate of oxygen transfer from the gas phase to the aqueous phase to an unrealistic value. A temporary fix can be made by reducing the mass transfer rate of oxygen (for instance, by a factor of 15), but a more appropriate correction to the routine should be sought in future implementations. Figure 55 shows the original calculation with the un-modified mass transfer routine compared with the modified mass transfer routine.

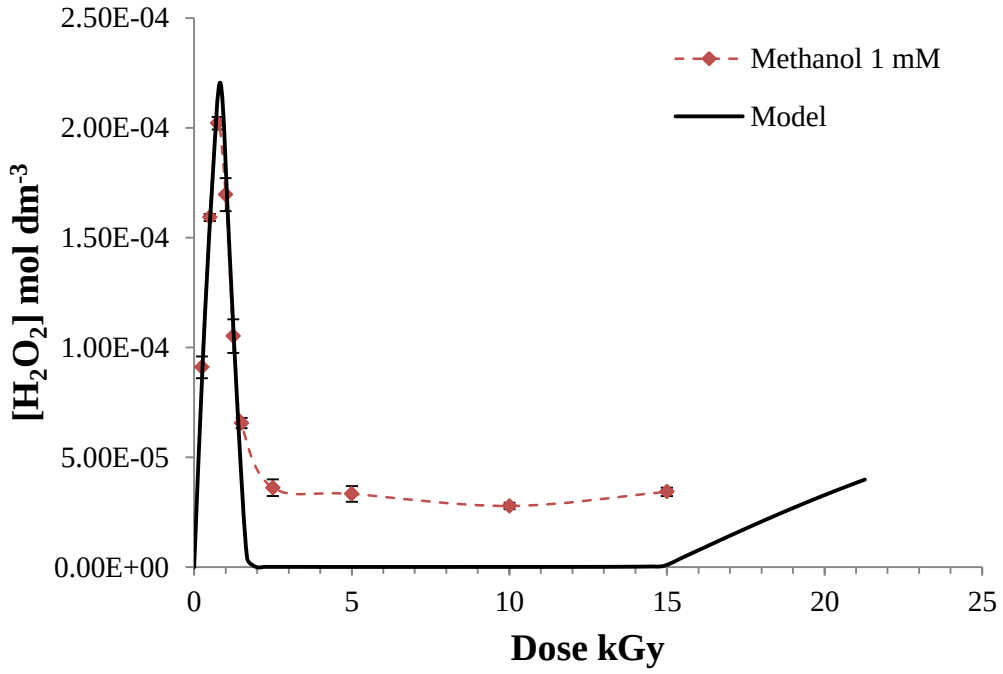

Figure 54: *Model prediction of H_2O_2 concentrations as a function of dose in a solution of 1 mM methanol.*

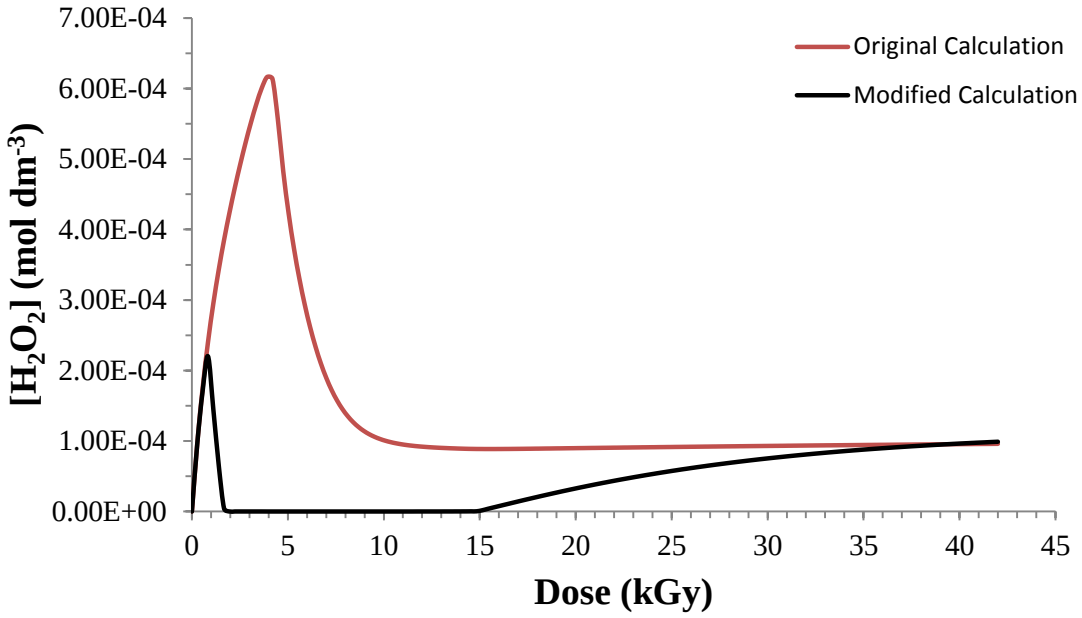

Figure 55: *Calculations of hydrogen peroxide concentrations with and without modification to the mass transfer routine.*

Analyses of the evolution of the calculated reaction rates reveal a possible explanation for the behaviour of hydrogen peroxide in the presence of a low concentration of methanol. Initially, the most important methanol reactions are the formation of the methanol radical by scavenging hydroxyl radicals (M1), and the formation of an organic peroxide by the reaction between the aforementioned methanol radical and oxygen (M3).

$$CH_3OH + {}^{\bullet}OH \rightarrow {}^{\bullet}CH_2OH + H_2O$$

$${}^{\bullet}CH_2OH + O_2 \rightarrow {}^{\bullet}O_2CH_2OH$$

With the formation of the organic peroxide comes an increase in the rate of the formation of formaldehyde, mainly through self-reaction or to a lesser degree, through reaction with superoxide.

$$2^{\bullet}O_2CH_2OH \rightarrow 2H_2CO + H_2O_2 + O_2$$

$$^{\bullet}O_2CH_2OH + O_2^{\bullet -} \rightarrow H_2CO + HO_2^- + O_2$$

These reactions not only contribute to the production of hydrogen peroxide, but also return oxygen to the system which can scavenge solvated electrons and protect hydrogen peroxide from the rapid reaction between the solvated electron and hydrogen peroxide (R4, $k = 1.36\times10^{10}\ M^{-1}\ s^{-1}$). The total rate of oxygen consumption by methanol radicals and solvated electrons is still greater than the rate of return from the reactions of the organic peroxide. After about 1.1 kGy oxygen concentrations are reduced to an insignificant value. As the concentration of oxygen falls, the reaction rate between hydrogen peroxide and the solvated electron increases. As mentioned in Chapter 4, oxygen plays a vital role in the formation and protection of hydrogen peroxide. The model prediction shows the concentration of hydrogen peroxide beginning to rise again after about 8 kGy, this is due to the mass transfer of oxygen gas into the aqueous phase, slowly re-establishing equilibrium and effectively allowing a build-up of hydrogen peroxide. As mentioned earlier, the mass transfer routine has been modified for this calculation and is non-representative of the real mass transfer flux, nevertheless it is reasonable to assume that after the depletion of dissolved oxygen and the methanol has been converted to glycol or formaldehyde, equilibrium of aqueous and gaseous oxygen would eventually be re-established. This could be supported by further analysis at higher doses which may show an increase in hydrogen peroxide concentrations.

The formation of hydrogen gas is enhanced by the presence of methanol; however hydrogen gas production is not linear with dose. Figure 56 shows the model predictions for hydrogen gas production compared to the experimentally obtained data.

The calculations show a higher production rate of hydrogen gas can be attributed to the scavenging of hydroxyl radicals by methanol and a number of methanol radiolysis products.

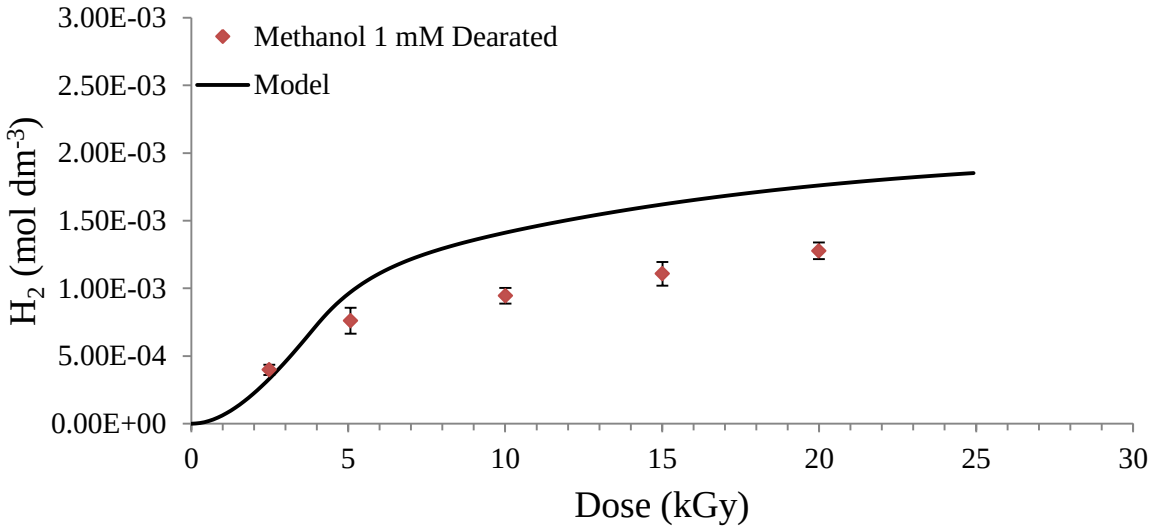

Figure 56: *Model prediction of H_2 gas as a function of dose in a solution of 1 mM methanol.*

Although the model prediction somewhat overestimates the quantity of hydrogen formed, the slope is close to what is observed experimentally. Many of the rate constants used in the reaction scheme could not be found in the literature and are therefore estimations. The reaction scheme used protects molecular hydrogen from reacting with the hydroxyl radical in a number of reactions. Throughout the radiolysis of methanol a number of intermediary organic products are formed such as ethylene glycol and formaldehyde, each of which is an effective hydroxyl scavenger.

After reacting with the hydroxyl radical, the newly formed organic radical will usually form an organic peroxide, however in the absence of oxygen the radicals will tend towards disproportionation to reform the original organic product at well as a new stable organic, usually an aldehyde. Eventually the only stable product is carbon monoxide which does not have any further reactions within this scheme. Figure 57 shows the calculated concentrations of each of the stable organic products as a function of dose in an aerated system.

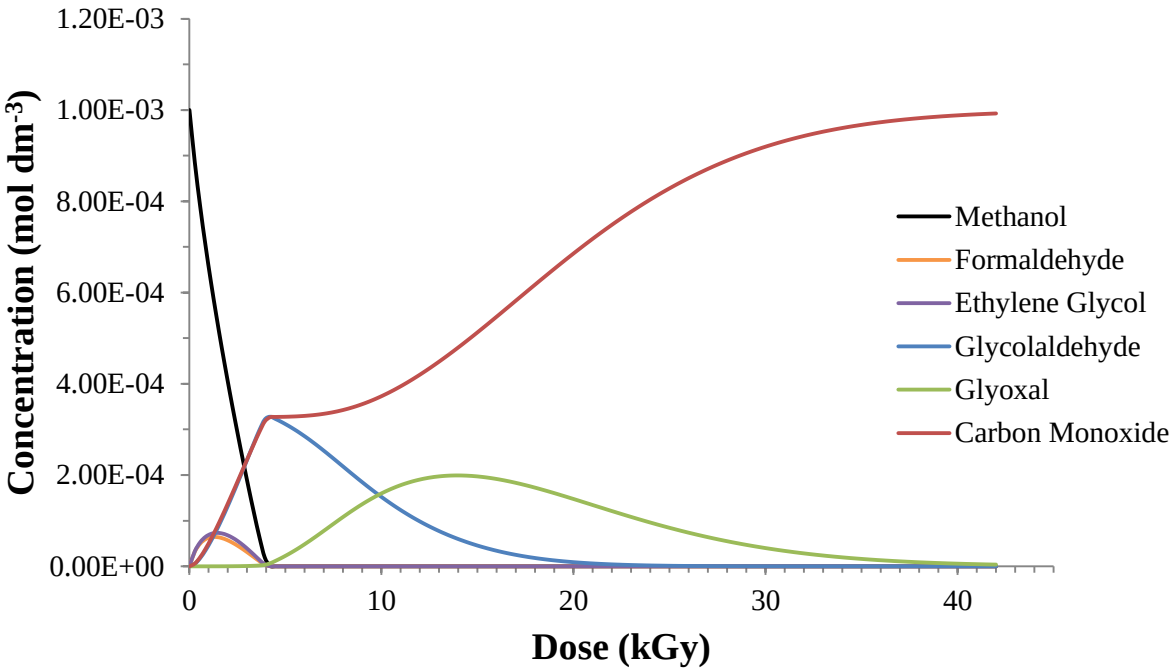

Figure 57: *Model predictions of the concentrations of various stable organic products formed as a result of using the proposed reaction scheme in Table 23.*

Kinetic models of aqueous methanol have previously been presented in literature, one such model by Sunaryo and Domae[126] was developed for calculating the effects of aqueous methanol in light water reactors.

The reaction scheme for methanol radiolysis used in that publication is not a complete scheme, in that "imaginary products" are implemented to terminate certain reaction pathways. This is still a valid approach, as their interest was focused on the initial reaction paths when delivering a maximum dose of 500 Gy, and not the long term radiolysis of methanol over several kGy.

It was noted that an understanding of the radiolysis of the transient organic products is needed; they concluded that methanol is converted into ethylene glycol which may have the same effect as methanol itself. The formation of ethylene glycol and formaldehyde from methanol radiolysis is well known and has been measured in previous studies.[127] The radiolysis of ethylene glycol has also been discussed in literature[128] and it has been described, that under aerated conditions the main organic product of radiolysis is glycolaldehyde.[129] The reaction scheme for methanol radiolysis in this work assumes the formation of a radical species by the reaction between glycolaldehyde and the hydroxyl radical, however this is most likely not the major radiolysis path for glycolaldehyde. In aqueous solutions glycolaldehyde exists in a number of different forms, with the aldehyde form usually being the minor component.[130] The existence of multiple forms of glycolaldehyde in solution and the large number of unknown rate constants makes creating a complete reaction scheme for methanol radiolysis difficult. Furthermore, the publications mentioned above also report the formation of small amounts of methane along with carbon monoxide. The radiolysis of ethylene glycol under deaerated conditions can also lead to the production of ethyl aldehyde. Both of these points highlight gaps in the reaction scheme that should be included in a comprehensive description of methanol radiolysis. Suggestions for an improved radiolysis scheme are given in Chapter 8.

Chapter 7: Radiolysis of Iron Oxide-Water Systems

Context

Large quantities of iron oxide have been reported to be present in the First Generation Magnox Storage Pond, where iron skips containing spent fuel have corroded to form a layer of haematite (Fe_2O_3) and magnetite (Fe_3O_4) several meters below the water level. Documented investigations into the effects of iron oxide on water radiolysis are sparse; the most recent of which focusing on the formation of molecular hydrogen from the radiolysis of water-iron oxide systems.[131] Preliminary experiments have been carried out to investigate the effects iron oxide may have on radiolytic production of hydrogen peroxide from water-oxide slurries.

Method

Iron oxide powders were washed with ultra-pure water to remove any soluble contamination. Excess water was decanted before the powders were washed a further two times. After the third decanting, the powders were dried in a vacuum oven at 40°C overnight. Haematite samples were prepared by weighing 0.5 g quantities of haematite into 20 mL headspace vials, to which 10 mL of ultra-pure water was added before sealing with a crimp cap. Samples of magnetite were prepared in the same way. Samples were agitated and then left to settle before irradiation. The irradiations of haematite samples were carried out in row 1 of the 4x8 irradiation rack with an average dose rate of 305.18 Gy min^{-1} while irradiations of magnetite samples were carried out in row 2 of the 4x8 rack with an average dose rate of 162.52 Gy min^{-1}. After irradiation, aliquots of the water from the samples were removed by syringe and pushed through a syringe filter to remove any solid particles.

The filtered aliquot was then analysed for hydrogen peroxide using the Ghormley tri-iodide method described in Chapter 2.

Results

Figure 58 shows the obtained results for the haematite system compared to concentrations of hydrogen peroxide measured in aerated water. Figure 59 shows the obtained results from magnetite samples, again they are compared with measurements obtained from pure water.

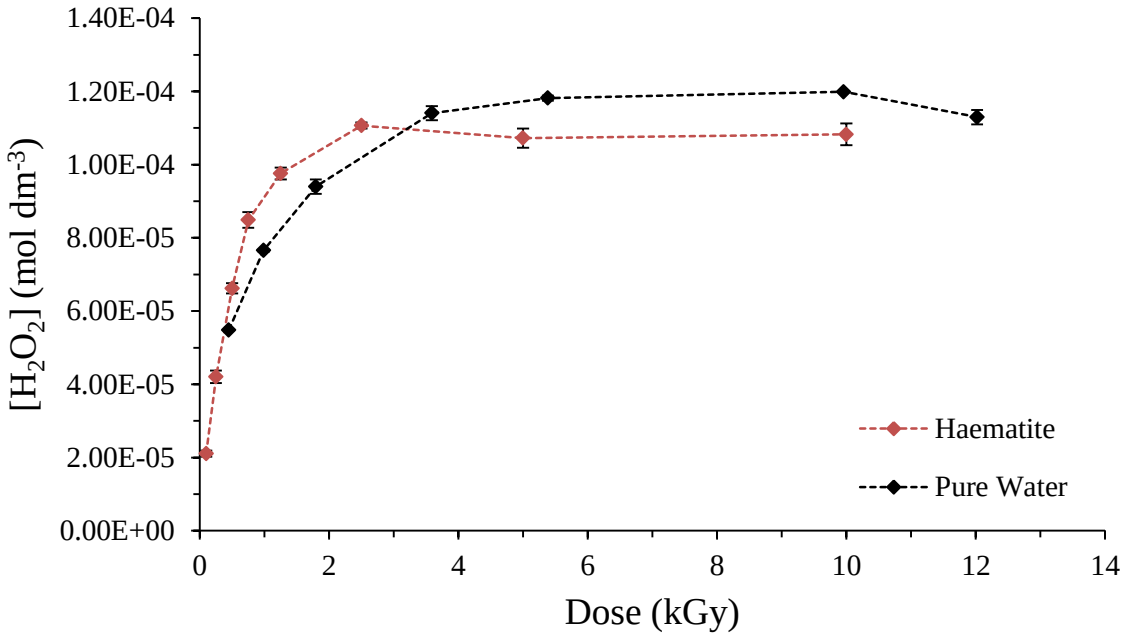

Figure 58: *Measurements of H_2O_2 concentrations from heterogeneous samples of 0.5g Fe_2O_3 and 10 mL aerated water. The dose rate for the haematite samples was 305.2 Gy min^{-1} and for the aerated water the dose rate was 283.9 Gy min^{-1}.*

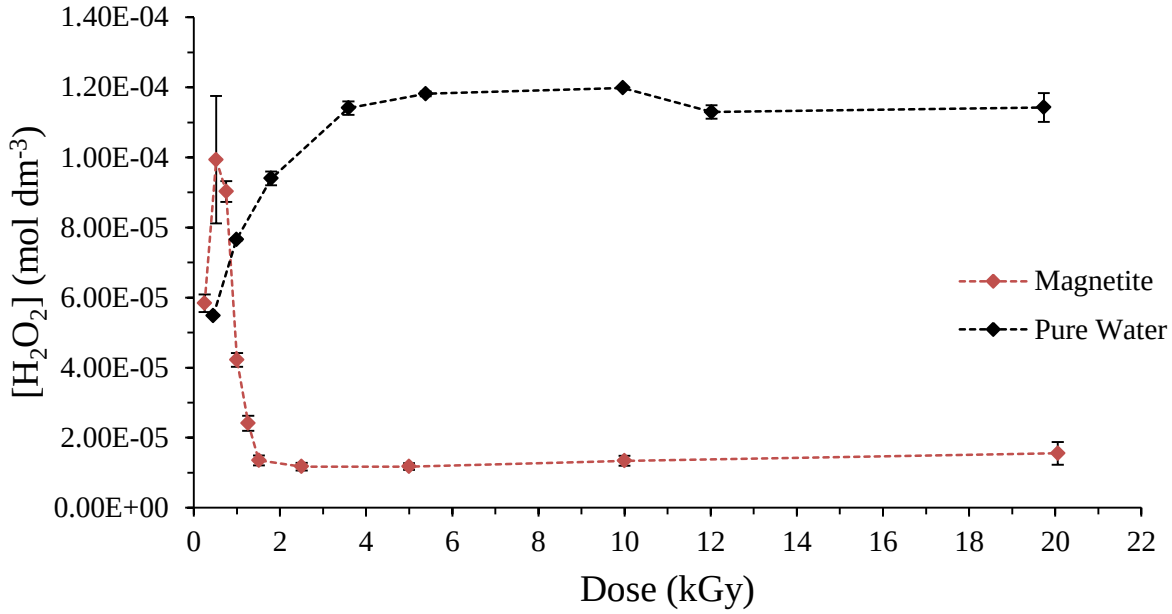

Figure 59: *Measurements of H_2O_2 concentrations from heterogeneous samples of 0.5g Fe_3O_4 and 10 mL aerated water. The dose rate for the magnetite samples was 162.5 Gy min^{-1} and for the aerated water the dose rate was 283.9 Gy min^{-1}.*

The steady state concentration of hydrogen peroxide achieved in the presence of haematite is close to that of pure water; however the initial production rate is slightly higher. An increased initial production rate is also observed in samples containing magnetite but after approximately 500 Gy the concentration of hydrogen peroxide falls dramatically and achieves a low steady state of approximately 1.5×10^{-5} mol dm^{-3}.

Discussion

Hydrogen peroxide undergoes surface decomposition over both haematite and magnetite.[28,132] The estimated second-order rate constants for the surface decomposition of hydrogen peroxide are quoted as 3.0×10^{-9} M^{-1} s^{-1} for haematite[132] and 4.5×10^{-10} M^{-1} s^{-1} for magnetite.[28] Calculations using the water radiolysis model including a hypothetical reaction that removes hydrogen peroxide at these rates makes no significant difference to the predicted concentrations of hydrogen peroxide in water, over the time scale of the experiment. However, as the aforementioned rate constants are second-order, they not only depend on the concentration of hydrogen peroxide but the surface area of the metal oxide as well, which is unknown for the metal oxides used in this study.

Furthermore, the experiments carried out in the aforementioned publications to determine these rate constants were well mixed throughout the reaction time, while in this work the samples were static; with the iron powder settled at the bottom of the reaction vessel. This means that the rate of surface decomposition is greatly hindered due to the need for hydrogen peroxide to diffuse a large distance to the iron oxide surface; nevertheless a significant difference in hydrogen peroxide concentrations were observed in samples containing magnetite. The behaviour of hydrogen peroxide observed in samples containing magnetite is most likely due to homogeneous chemistry initiated by dissolved iron ions. The chemistry initiated by dissolved iron could serve to remove hydrogen peroxide through a Haber-Weiss mechanism.[133]

$$Fe^{3+} + O_2^{\bullet-} \rightarrow Fe^{2+} + O_2 \qquad \text{k = Unknown}$$

$$Fe^{2+} + H_2O_2 \rightarrow Fe^{3+} + OH^- + {}^{\bullet}OH \qquad \text{k = } 1.0 \times 10^{7}\ M^{-1}\ s^{-1}$$

$$Fe^{2+} + {}^{\bullet}OH \rightarrow Fe^{3+} + OH^- \qquad \text{k = } 3.2 \times 10^{8}\ M^{-1}\ s^{-1}$$

$$Fe^{2+} + HO_2^{\bullet} \rightarrow Fe^{3+} + HO_2^- \qquad \text{k = } 1.2 \times 10^{6}\ M^{-1}\ s^{-1}$$

Experiments discussed in publications by Mats Jonsson[28] focus largely on the reactivity of hydrogen peroxide and various metal oxides, including iron oxide. It was found that many metal oxide surfaces show reactivity towards hydrogen peroxide and that rate of removal of hydrogen peroxide can be calculated in heterogeneous systems based on properties such as particle size. As mentioned previously, the model suggests that the rate of this surface reactivity does not seem to be able to compete with the rate of radiolytic hydrogen peroxide production. The studies by Jonsson, concerning iron oxide were met with difficulty in discriminating between surface reactions and aqueous chemistry initiated by dissolved iron. Through the use of ICP-AES, it was shown that iron can be found in water with a concentration of 2.3×10^{-6} mol dm^{-3} after just 30 minutes of mixing magnetite with distilled water.[28]

Even with this measurement by Jonsson, the quantity of dissolved iron is difficult to estimate for samples used in this work as they were washed with water, whereas the literature measurements were made with unwashed or EDTA treated samples. More information about the dissolution of iron from magnetite could be used to attempt to model this behaviour using the reaction scheme in table 24. In addition to this, it would also be useful to investigate the dissolution of iron as a function of radiation dose to see what effect, if any, radiation has on dissolution rates. Analysis techniques such as inductively coupled plasma mass spectroscopy (ICP-MS) can be used to determine concentrations of dissolved iron in very low concentrations, however due to the nature of the plasma used it can often be difficult to distinguish between Fe^{2+} and Fe^{3+} as further ionization may cause interference. It is possible to chemically separate the two oxidation states of iron by solvent extraction with *n*-heptane containing 0.1 M Di-(2-ethylhexyl)phosphoric acid (HDEHP) before performing an analysis for iron.[134]

This reaction scheme would be initiated by a production of aqueous iron based on the dissolution behaviour observed from future experiments. As mentioned earlier, the experiments conducted in this work are only preliminary and there is much more work to be done on the subject.

If a computational model could be made to accurately simulate the aqueous iron chemistry, coupled with a more detailed understanding of radiation induced iron dissolution, it may be possible to determine the surface effects of iron oxide by comparison of experimental and calculated data and effectively subtracting the difference.

Reaction Number	Reaction	Rate Constant at 25°C (M^{-1} s^{-1})	Ref
F1	$Fe^{2+} + H_2O_2 \rightarrow Fe^{3+} + OH^- + {}^{\bullet}OH$	1.00×10^7	135
F2	$Fe^{2+} + {}^{\bullet}OH \rightarrow Fe^{3+} + OH^-$	3.2×10^8	136
F3	$Fe^{2+} + {}^{\bullet}HO_2 \rightarrow Fe^{3+}HO_2^-$	1.2×10^6	133
F4/5	$Fe^{3+}HO_2^- + Fe^{2+} \rightleftharpoons Fe^{3+}HO_2^-Fe^{2+}$	$K = 27\ M^{-1}$	133
F6	$Fe^{3+}HO_2^- \rightarrow Fe^{3+} + HO_2^-$	$1.8 \times 10^3\ s^{-1}$	133
F7	$Fe^{3+}HO_2^-Fe^{2+} \rightarrow Fe^{3+} + Fe^{2+}HO_2^-$	2.5×10^4	133
F8	$Fe^{2+}HO_2^- + H^+_{(aq)} \rightarrow Fe^{2+} + H_2O_2$	Unknown	133
F9	$Fe^{3+} + O_2^- \rightarrow Fe^{2+} + O_2$	Unknown	137
F10	$Fe^{2+} + O_2^- + H_2O \rightarrow HO_2^- + Fe^{3+} + OH^-$	1.0×10^7	133
F11	$Fe^{3+} + H^{\bullet} \rightarrow Fe^{2+} + H^+_{(aq)}$	2.0×10^6	138
F12	$Fe^{3+} + e^-_{aq} \rightarrow Fe^{2+}$	6.0×10^{10}	139
F13	$Fe^{2+} + H^{\bullet} + H^+_{(aq)} \rightarrow Fe^{3+} + H_2$	7.5×10^6	10

Table 24: *A reaction scheme to estimate the effects of dissolved iron in water radiolysis.*

Chapter 8: Conclusions and Further Work

Further High pH Investigations

Experiments have shown that the radiolytic production of hydrogen gas and hydrogen peroxide is strongly influenced by high pH. Hydrogen peroxide tends to reach higher steady state concentrations with increasing pH as well as taking longer to reach this steady state. Hydrogen gas production rates appear to also increase with increasing pH up to approximately pH 11 where thereafter, they decrease. The development of a computational model for water radiolysis has provided a mechanistic understanding to explain the observed effects of high pH on water radiolysis. Calculations suggest that an increase in radiolytically produced oxygen could explain the behaviour of hydrogen gas at high pH. Dissolved oxygen acts as a poison to the Allen chain which normally serves to remove dissolved hydrogen through reactions with the hydroxyl radical or, the alkali equivalent, the oxide radical anion. The steady state concentration of dissolved oxygen increases with pH up to approximately pH 11.5. This can be attributed to the decline in the rate at which dissolved oxygen is reduced by hydrogen atoms as the equilibrium between the hydrogen atom and the solvated electron shifts to favour the solvated electron. The reaction rate of the equivalent alkali reaction to remove dissolved oxygen through reduction by the solvated electron does not increase to compensate, resulting in a net increase in the steady state concentration of dissolved oxygen. The model calculations also show that increasing the pH further results in a decline in the hydrogen gas production rate. This is due to the shift in the equilibrium between the hydroxyl radical and the oxide radical anion (R63/64) which has a pK_a of 11.9. The main pathway for the radiolytic production of dissolved oxygen is the reaction between the hydroxyl radical and super oxide (R21).

The rate of this reaction falls at high pH as the hydroxyl radical is converted to the oxide radical anion. The alkali equivalent of this reaction (R50) has a much lower rate constant and is out competed by the solvated electron (R8). Further experiments to measure the concentration of radiolytically produced oxygen at high pH could help to support the model predictions or confirm a misunderstanding in the model. An inline gas chromatography technique similar to the "crush tube" described in Chapter 2 may be used, only instead of crushing a sealed glass vial within the carrier gas flow, a specially designed cell is connected to the in and out ports of the carrier gas flow. This cell would contain a high pH solution and would sit inside the irradiator; from here multiple analyses can be run on a single sample. The carrier gas would have to be changed from argon to helium to increase the sensitivity towards oxygen; running the carrier gas through the cell prior to irradiation will serve to remove the initial dissolved oxygen from the sample; from this point onward any measurements of oxygen would be radiolytically produced.

These experiments would help to better understand high pH water radiolysis and hopefully help to improve the radiolysis model and understand why there is an over prediction at pH 10.6. A comprehensive water radiolysis model that can accurately predict concentrations of radiolysis products under a wide range of conditions is of high importance to the nuclear industry and would have applications in decommissioning, maintenance of current nuclear systems, and designing new nuclear technology.

Further Methanol Radiolysis Investigations

The reaction scheme used to model the radiolysis of aqueous methanol results in the temporary formation of several stable organic species before they themselves are oxidised by hydroxyl radicals. This scheme eventually converts all organic substances to carbon monoxide, however in reality this is not the case. It has been reported in literature that one of the stable products formed is methane gas, a substance not included in the current reaction scheme. The gas chromatography techniques used in this work are not suitable for the detection of small quantities of carbon monoxide or indeed other potential radiolysis products such as methane. A more sophisticated approach would be to use a gas chromatography mass spectroscopy technique (GC-MS). This technique would allow for the detection of carbon monoxide, carbon dioxide, methane, and any other volatile hydrocarbons that may be formed during radiolysis. Other transient products of methanol radiolysis such as formaldehyde, ethylene glycol, glycolaldehyde, and glyoxal may be analysed by high performance liquid chromatography (HPLC). It was mentioned in Chapter 6 that the reaction scheme does not accurately represent the radiolysis of the transient product, glycolaldehyde. A publication by Yaylayan et al[130] discusses some measurements made by nuclear magnetic resonance spectroscopy, of glycolaldehyde in deuterated water and it was found that it exists mostly as the hydrated aldehyde, 1,1,2-ethanetriol (~70%). A complete reaction scheme for the radiolysis of methanol should include the radiolysis reactions of all the transient species, of which there are potentially many.

However if the major component of a glycolaldehyde solution is 1,1,2-ethanetriol, an acceptable compromise may be to include only the radiolysis reactions of this species and ignore the radiolysis paths of minor products.

Experimental analysis of aqueous methanol to determine the major transient species would be valuable for determining which radiolysis paths have the most significant roles in methanol radiolysis.

Future Development of a Multi-Scale Radiolysis Model

As discussed in Chapter 3 the model developed in this work is a deterministic model for the calculation of long term homogeneous phase radiolysis. This calculation depends on a series of primary values that represent the production rates of the primary species of water radiolysis, which in turn depend on a number of physical and chemical factors. It is possible to calculate these primary yields using stochastic methods which can then be fed into the deterministic calculation to obtain predictions of chemical species concentrations. This technique has been successfully used recently to demonstrate some of the effects of high capacity scavengers.[47] This technique assumes that there are no changes to the physiochemical conditions during the radiolysis period, for example if a calculation was to be performed where the temperature were to change, the primary yields would need to be recalculated at the new temperature. The model developed in this work attempts to overcome this by estimating primary yields as a multiple regression fit of temperature and pH, however this estimation is not adequately accurate and does not include any effects that linear energy transfer has on the primary yields. A more suitable approach to the development of a comprehensive multi-scale radiolysis model may be to utilise a stochastic calculation of the primary yields that includes the effects of temperature, pH, LET, and chemical scavengers which can be called from within the deterministic calculation whenever a significant change to one of these factors is initiated.

Further work concerning the deterministic model, presented in this work, include an investigation into the partitioning of gaseous species. The method used is one that has been successfully used by other research groups to model the radiolysis of water and the effect of available headspace. This implementation of the stagnant two-film model was never intended to cope with rapid changes in aqueous oxygen concentrations. Further efforts should be made to better incorporate this gas partitioning method in a way that can more realistically represent oxygen partitioning during the radiolysis of aqueous methanol.

Closing Remarks Relevant to Sellafield Ltd

The experimental data presented in Chapters 4 and 5 are pertinent to the situations and conditions currently found within the Magnox Swarf Storage Silos at Sellafield. In the case of elevated pH due to sodium hydroxide, both the experimental and computational data show increased rates of hydrogen gas production and an increased steady-state concentration of hydrogen peroxide. Despite some minor quantitative disagreements between the experimental data and the computational data, the qualitative trend is in general agreement. One could therefore expect to observe increased production of hydrogen gas in the MSSS with increasing pH, especially within the pH region of approximately 10.5 to 12.5. An important aspect of the situation at the MSSS is the aerated nature of the system. The obvious consideration being the increased amounts of dissolved oxygen present, which, although such effects were also discussed in Chapter 4, the experimental data shown was only for water at neutral pH. Nevertheless, it was discussed in Chapter 4 that dissolved oxygen acts a poison to the chain reaction that normally removes molecular hydrogen. A less obvious consideration, and one that was largely overlooked in Chapter 4, is the inclusion of gas to liquid carbon dioxide exchange and its aqueous conversion to carbonate.

At high pH the concentration of aqueous CO_2, and therefore CO_3^{2-} , becomes significant. With CO_3^{2-} being known to react with the hydroxyl radical, and given the difficulty in its removal, future research and industrial models involving high pH aqueous radiolysis would benefit from including a description of the radiolysis chemistry of aqueous carbonate systems. Chapter 5 begins to address the concept of including carbonate chemistry into a radiolysis model. This came about from the realisation that magnesium hydroxide can be easily carbonated on contact with CO_2 and is also known to be an effective carbon trapping material. In this case, not only the additional chemistry brought about carbonate should be considered, but also the effects of the magnesium compounds that can be formed, for example, magnesium carbonate, magnesium bicarbonate, magnesium oxide, and magnesium hydroxide. Similarly, consideration should be given to the multitude of iron phases that can exist in conditions comparable to those of the First Generation Magnox Storage Ponds. Although it was not considered in Chapter 7, it is likely that the corroded iron found in the FGMSP also exists as a number of iron hydroxides and hydrated oxides. Given the open air nature of the FGMSP, hydrogen gas build-up is not a major concern; however, the interactions of the various iron oxide phases in a radiolysis system may affect concentrations of oxidising species such as H_2O_2 which may alter corrosion rates. The results shown in Chapter 7 suggest little effect on H_2O_2 concentration in the presence of haematite, but the presence of magnetite had a significant effect in removing H_2O_2. To gain a better understanding, further work would need to be done that also investigated the other possible phases of iron oxide and also gives consideration to the proportions in which they can be found in the FGMSP.

References

1 Pitois A., Ivanov P. I., Abrahamsen L. G., Bryan N. D., Taylor R. J. & Sims H. E. Magnesium Hydroxide Bulk and Colloid-Associated ^{152}Eu in an Alkaline Environment: Colloid Characterisation and Sorption Properties in the Presence and Absence of Carbonate. *J. Environ. Monit.* **10**, 315-324, (2008).

2 Spinks J. W. T. & Woods R. J. *An Introduction to Radiation Chemistry*. (1990).

3 Loveland W. D., Morrissey D. J. & Seaborg G. T. *Modern Nuclear Chemistry*. (2005).

4 Allen A. O. *The Radiation Chemistry of Water and Aqueous Solutions*. (1961).

5 Draganić I. G. & Draganić Z. D. *The Radiation Chemistry of Water*. (1971).

6 Schwarz H. A., Losee J. P. & Allen A. O. Hydrogen Yields in the Radiolysis of Aqueous Solutions. *Journal of the American Chemical Society* **76**, 4693-4694, (1954).

7 Swallow A. J. *Radiation Chemistry: An Introduction*. (1973).

8 Schwarz H. A. Free Radicals Generated by Radiolysis of Aqueous Solutions. *Journal of Chemical Education* **58**, 101, (1981).

9 Buxton G. V., Clive L., Greenstock W., Helman P. & Ross A. B. Critical Review of Rate Constants for Reactions of Hydrated Electrons, Hydrogen Atoms and Hydroxyl Radicals ($^{\cdot}$OH/O$^{\cdot-}$) in Aqueous Solution. *J. Phys. Chem. Ref. Data* **17**, 513-886, (1988).

10 Jayson G. G., Keene J. P., Stirling D. A. & Swallow A. J. Pulse-Radiolysis Study of Some Unstable Complexes of Iron. *Transactions of the Faraday Society* **65**, 2453-2464, (1969).

11 Koppenol W. H. & Liebman J. F. The Oxidizing Nature of the Hydroxyl Radical. A Comparison with the Ferryl Ion (FeO^{2+}). *The Journal of Physical Chemistry* **88**, 99-101, (1984).

12 Meyerstein D. Complexes of Cations in Unstable Oxidation States in Aqueous Solutions as Studied by Pulse Radiolysis. *Accounts of Chemical Research* **11**, 43-48, (1978).

13 Schwarz H. A. Applications of the spur diffusion model to the radiation chemistry of aqueous solutions. *The Journal of Physical Chemistry* **73**, 1928-1937, (1969).

14 Dyne P. J. & Kennedy J. M. The Kinetics of Radical Reactions in the Tracks of Fast Electrons. A Detailed Study of the Samuel–Magee Model for the Radiation Chemisty of Water. *Canadian Journal of Chemistry* **36**, 1518-1536, (1958).

15 Burns W. G., Sims H. E. & Goodall J. A. B. Special Issue Dedicated to The Memory of the Late John Hodson Baxendale Radiation chemical diffusion kinetic calculations with prescribed and non-prescribed diffusion—I. *Radiation Physics and Chemistry (1977)* **23**, 143-180, (1984).

16 Pimblott S. M. & LaVerne J. A. Comparison of Stochastic and Deterministic Methods for Modeling Spur Kinetics. *Radiation Research* **122**, 12-23, (1990).

17 Tapping R. L. Corrosion Issues in Pressurized Heavy Water Reactor (PHWR/CANDU®) Systems A2 in *Nuclear Corrosion Science and Engineering* 581-633 (2012).

18 Petrik N. G., Alexandrov A. B. & Vall A. I. Interfacial Energy Transfer During Gamma Radiolysis of Water on the Surface of ZrO_2 and Some Other Oxides. *The Journal of Physical Chemistry B* **105**, 5935-5944, (2001).

19 LaVerne J. A. & Tandon L. H_2 and Cl_2 Production in the Radiolysis of Calcium and Magnesium Chlorides and Hydroxides. *The Journal of Physical Chemistry A* **109**, 2861-2865, (2005).

20 Slack J., Norton J. L. & Malkoske G. R. Cobalt-60 Production in CANDU Power Reactors.

21 Unterweger M. P., Hoppes D. D. & Schima F. J. New and Revised Half-Life Measurements Results. *Nuclear Instruments and Methods in Physics Research Section A: Accelerators, Spectrometers, Detectors and Associated Equipment* **312**, 349-352, (1992).

22 Weiss J. A Survey of Chemical Dosimetric Systems. *The International Journal of Applied Radiation and Isotopes* **4**, 89-95, (1958).

23 Fricke H. & Morse S. The Chemical Action of Röntgen Rays on Dilute Ferrosulfate Solutions as a Measure of Dose. *Am. J. Roentgenology and Radium Therapy* **18**, 430-432, (1927).

24 Weiss J., Allen A. O. & Schwarz H. A. Fricke Ferrous Sulfate Dosimeter for γ-rays in the Range 4 to 40 Kiloröntgens. *Proceedings of the International Conference on the Peaceful Uses of Atomic Energy* **14**, 179-181, (1956).

25 Allen A. O., Hochanadel C. J., Ghormley J. A. & Davis T. W. Decomposition of Water and Aqueous Solutions under Mixed Fast Neutron and Gamma Radiation. *American Chemical Society*, (1952).

26 Hiroki A., Pimblott S. M. & LaVerne J. A. Hydrogen Peroxide Production in the Radiolysis of Water with High Radical Scavenger Concentrations. *The Journal of Physical Chemistry A* **106**, 9352-9358, (2002).

27 Yakabuskie P. A., Joseph J. M. & Wren C. J. The Effect of Interfacial Mass Transfer on Steady-State Water Radiolysis. *Radiation Physics and Chemistry* **79**, 777-785, (2010).

28 Nejad M. A. & Jonsson M. Reactivity of Hydrogen Peroxide towards Fe_3O_4, Fe_2CoO_4 and Fe_2NiO_4. *Journal of Nuclear Materials* **334**, 28-34, (2004).

29 Pastina B. & LaVerne J. A. Effect of Molecular Hydrogen on Hydrogen Peroxide in Water Radiolysis. *The Journal of Physical Chemistry A* **105**, 9316-9322, (2001).

30 Klassen N. V., Marchington D. & McGowan H. C. E. H_2O_2 Determination by the I_3^- Method and by $KMnO_4$ Titration. *Analytical Chemistry* **66**, 2921-2925, (1994).

31 Roth O. & LaVerne J. A. Effect of pH on H_2O_2 Production in the Radiolysis of Water. *J. Phys. Chem. A* **115**, 700-708, (2011).

32 Wasselin-Trupin V., Baldacchino G., Bouffard S. & Hickel B. Hydrogen Peroxide Yields in Water Radiolysis by High-Energy Ion Beams at Constant LET. *Radiation Physics and Chemistry* **65**, 53-61, (2002).

33 Essehli R., Crumière F., Blain G., Vandenborre J., Pottier F., Grambow B. *et al.* H_2 Production by γ and He Ions Water Radiolysis, Effect of Presence TiO_2 Nanoparticles. *International Journal of Hydrogen Energy* **36**, 14342-14348, (2011).

34 Faraggi M., Zehavi D. & Anbar M. Effect of Thallous Ions on the Yields of Hydrogen and Hydrogen Peroxide in Radiolyzed Aqueous Solutions. *Transactions of the Faraday Society* **67**, 2057-2067, (1971).

35 Lousada C. M., LaVerne J. A. & Jonsson M. Enhanced Hydrogen Formation During the Catalytic Decomposition of H_2O_2 on Metal Oxide Surfaces in the Presence of $^{\cdot}OH$ Radical Scavengers. *Phys. Chem. Chem. Phys.* **15**, 12674-12679, (2013).

36 Schofield J., Reiff S. C., Pimblott S. M. & LaVerne J. A. Radiolytic Hydrogen Generation at Silicon Carbide–Water Interfaces. *Journal of Nuclear Materials* **469**, 43-50, (2016).

37 LaVerne J. A., Ryan M. R. & Mu T. Hydrogen Production in the Radiolysis of Bromide Solutions. *Radiation Physics and Chemistry* **78**, 1148-1152, (2009).

38 Draganic I., Nenadovic M. T. & Draganic Z. D. Radiolysis of HCOOH + O_2 at pH 1.3-13 and the Yields of Primary Products in γ Radiolysis of Water. *Journal of Physical Chemistry* **73**, 2564-2571, (1969).

39 Hart E. J. γ-Ray Induced Oxidation of Aqueous Formic Acid-Oxygen Solutions. Effect of pH. *Journal of the American Chemical Society* **76**, 4198-4201, (1954).

40 Flanders D. A. & Fricke H. Application of a High-Speed Electronic Computer in Diffusion Kinetics. *The Journal of Chemical Physics* **28**, 1126-1129, (1958).

41 Burns W. G., Sims H. E. & Goodall J. A. B. Radiation Chemical Diffusion Kinetic Calculations with Prescribed and Non-Prescribed Diffusion—I: Spherical and Cylindrical Cases. *Radiation Physics and Chemistry* **23**, 143-180, (1984).

42 Green N. J. B., Pilling M. J., Pimblott S. M. & Clifford P. Stochastic Modeling of Fast Kinetics in a Radiation Track. *The Journal of Physical Chemistry* **94**, 251-258, (1990).

43 Bouniol P. & Bjergbakke E. A Comprehensive Model to Describe Radiolytic Processes in Cement Medium. *Journal of Nuclear Materials* **372**, 1-15, (2008).

44 Ershov B. G. & Gordeev A. V. A Model for Radiolysis of Water and Aqueous Solutions of H_2, H_2O_2 and O_2. *Radiation Physics and Chemistry* **77**, 928-935, (2008).

45 Elliot A. J. & Bartels D. M. The Reaction Set, Rate Constants and g-Values for the Simulation of the Radiolysis of Light Water over the range 20°C to 350°C Based on Information Available in 2008. (Atomic Energy of Canada Limited, Mississauga, Ontario (Canada), 2009).

46 Wren J. C. & Ball J. M. LIRIC 3.2 an Updated Model for Iodine Behaviour in the Presence of Organic Impurities. *Radiation Physics and Chemistry* **60**, 577-596, (2001).

47 Gregory P. Horne, Thomas A. Donoclift, Howard E. Sims, Robin M. Orr & Simon M Pimblott. Multi-Scale Modelling of the Radiolysis of Nitrate Solutions. *The Journal of Physical Chemistry B* **120 (45)**, 11781 - 11789, (2016).

48 Chance E. M., Curtis A. R., Jones I. P. & Kirby C. R. FACSIMILE: A Computer Program for Flow and Chemistry Simulation, and General Initial Value Problems. Report No. 0436-9734, 148 pp. (Univ. Coll., 1977).

49 Elliot A. J. Rate Constants and G-Values for the Simulation of the Radiolysis of Light Water Over the Range 0 - 300°C. *AECL-11073* **COG-94-167**, (1994).

50 Hochanadel C. J. & Ghormley J. A. Effect of Temperature on the Decomposition of Water by γ-Rays. *Radiat. Res.* **16**, 635-660, (1962).

51 Janik D., Janik I. & Bartels D. M. Neutron and β/γ Radiolysis of Water up to Supercritical Conditions. β/γ Yields for H_2, $H^{\bullet}$ Atom, and Hydrated Electron. *The Journal of Physical Chemistry A* **111**, 7777-7786, (2007).

52 Jha K. N., Ryan T. G. & Freeman G. R. Radiolysis of H_2O and D_2O between 0 and 300°C *J. Phys. Chem.* **79**, 868-870, (1974).

53 Elliot A. J., Chenier M. P. & Ouellette D. C. Temperature Dependence of g Values for H_2O and D_2O Irradiated with Low Linear Energy Transfer Radiation. *Journal of the Chemical Society, Faraday Transactions* **89**, 1193-1197, (1993).

54 Kent M. C. & Sims H. E. The Yield of γ-Radiolysis Products from Water at Temperatures up to 270°C. *Harwell Report AEA-RS-2301*, (1992).

55 Lin M., Katsumura Y., Muroya Y., He H., Wu G., Han Z. *et al.* Pulse Radiolysis Study on the Estimation of Radiolytic Yields of Water Decomposition Products in High-Temperature and Supercritical Water: Use of Methyl Viologen as a Scavenger. *The Journal of Physical Chemistry A* **108**, 8287-8295, (2004).

56 Štefanić I. & LaVerne J. A. Temperature Dependence of the Hydrogen Peroxide Production in the γ-Radiolysis of Water. *The Journal of Physical Chemistry A* **106**, 447-452, (2002).

57 Ferradini C. & Jay-Gerin J.-P. The Effect of pH on Water Radiolysis: A Still Open Question — A Minireview. *Research on Chemical Intermediates* **26**, 549-565, (2000).

58 Ferradini C. Kinetic Behavior of the Radiolysis Products of Water in *Advances in Inorganic Chemistry and Radiochemistry* Vol. Volume 3 (eds H. J. Emeleus & A. G. Sharpe) 171-205 (1961).

59 Lefort M. Radiation Chemistry. *Annual Review of Physical Chemistry* **9**, 123-156, (1958).

60 Sworski T. J. Yields of Hydrogen Peroxide in the Decomposition of Water by Cobalt γ-Rradiation I. Effect of Bromide Ion. *Journal of the American Chemical Society* **76**, 4687, (1954).

61 Hochanadel C. J. & Lind S. C. Radiation Chemistry. *Annual Review of Physical Chemistry* **7**, 83-106, (1956).

62 Mahlman H. A. & Boyle J. W. Primary Cobalt-60 Radiolysis Yields in Heavy Water. *Journal of the American Chemical Society* **80**, 773, (1958).

63 Hayon E. & Stein G. *Radiation Chemistry of Aqueous Systems*. (1968).

64 Hayon E. Effect of Solute Concentration on the Recombination of $H^{\cdot}$ and $^{\cdot}OH$ in γ-Irradiated Aqueous Solutions. *Journal of Physical Chemistry* **65**, 1502-1505, (1961).

65 Sehested K., Bjergbakke E. & Fricke H. The Primary Species Yields in the ^{60}Co γ-Ray Radiolysis of Aqueous Solutions of H_2SO_4 between pH 7 and 0.46. *Radiation Research* **56**, 385-399, (1973).

66 Hayon E. Radiolysis of Heavy Water in the pD Range 0-14. *Journal of Physical Chemistry* **69**, 2628-2632, (1965).

67 Haissinsky M. γ-Radiolysis of Alkaline and Neutral Solutions. I. Alkaline Solutions of Sodium Phosphite. *Journal de Chimie Physique et de Physico-Chimie* **62**, 1141-1148, (1965).

68 Dainton F. S. & Watt W. S. The Effect of pH on the Radical Yields in the γ-Radiolysis of Aqueous Systems. *Nature* **195**, 1294-1296, (1962).

69 Dainton F. S. & Rumfeldt R. Radical and Molecular Yields in the γ-Radiolysis of Water. III. The Nitrous Oxide-Sodium Tellurite System. *Proceedings of the Royal Society of London A: Mathematical, Physical and Engineering Sciences* **287**, 444-456, (1965).

70 Cheek C. H. & Linnenbom V. J. The Radiation Chemistry of Alkaline Hypobromite Solutions *The Journal of Physical Chemistry* **67**, 1856-1860, (1963).

71 Fielden E. M. & Hart E. J. Primary Radical Yields in Pulse-Irradiated Alkaline Aqueous Solution. *Radiation Research* **32**, 564-580, (1967).

72 Czapski G. & Peled E. On the pH-Dependence of Greducing in the Radiation Chemistry of Aqueous Solutions. *Israel Journal of Chemistry* **6**, 421-436, (1968).

73 Balkas T., Dainton F. S., Dishman J. K. & Smithies D. Radiation Chemistry of Aqueous Solutions Containing Carbon Monoxide and Oxygen Between pH 0.4 and 12. *Transactions of the Faraday Society* **62**, 81-87, (1966).

74 Pimblott S. M., Pilling M. J. & Green N. J. B. Stochastic Models of Spur Kinetics in Water. *International Journal of Radiation Applications and Instrumentation. Part C. Radiation Physics and Chemistry* **37**, 377-388, (1991).

75 Hayon E. Radical and Molecular Yields in the Radiolysis of Alkaline Aqueous Solutions. *Transactions of the Faraday Society* **61**, 734-743, (1965).

76 Gordon S. & Hart E. J. Chemical Yields of Ionizing Radiations in Aqueous Solutions: Effect of Energy of Alpha Particles. *Radiation Research* **15**, 440-451, (1961).

77 Kochanny G. L., Timnick A., Hochanadel C. J. & Goodman C. D. Radiation Chemistry Studies of Water as Related to the Initial Linear Energy Transfer of 11-MeV to 23-MeV Protons. *Radiation Research* **19**, 462-473, (1963).

78 ICRU Report 16 - Linear Energy Transfer. (ICRU, Washington U.S.A., 1970).

79 Schwarzenbach R. P., Gschwend P. M. & Imboden D. M. *Environmental Organic Chemistry*. (Wiley, 2005).

80 Ferrell R. T. & Himmelblau D. M. Diffusion Coefficients of Hydrogen and Helium in Water. *American Institute of Chemical Engineers* **13**, 702-708, (1967).

81 Han P. & Bartels D. M. Temperature Dependence of Oxygen Diffusion in H_2O and D_2O. *The Journal of Physical Chemistry* **100**, 5597-5602, (1996).

82 Marrero T. R. & Mason E. A. Gaseous Diffusion Coefficients. *Journal of Physical and Chemical Reference Data* **1**, 3-118, (1972).

83 Kestin J., Knierim K., Mason E. A., Najafi B., Ro S. T. & Waldman M. Equilibrium and Transport Properties of the Noble Gases and Their Mixtures at Low Density. *Journal of Physical and Chemical Reference Data* **13**, 229-303, (1984).

84 Sander R. Compilation of Henry's Law Constants for Inorganic and Organic Species of Potential Importance in Environmental Chemistry. (1999).

85 Mezyk Stephen P. & Bartels David M. Direct EPR Measurement of Arrhenius Parameters for the Reactions of $H^{\cdot}$ Atoms with H_2O_2 and $D^{\cdot}$ Atoms with D_2O_2 in Aqueous Solution. *Journal of the Chemical Society, Faraday Transactions* **91**, 3127-3132, (1995).

86 Joseph Jiju M., Seon Choi Byung, Yakabuskie Pam & Wren Clara J. A Combined Experimental and Model Analysis on the Effect of pH and $O_{2(aq)}$ on γ-Radiolytically Produced H_2 and H_2O_2. *Radiation Physics and Chemistry* **77**, 1009-1020, (2008).

87 Allen A. O. The Yields of Free $H^{\cdot}$ and $^{\cdot}OH$ in the Irradiation of Water. *Radiation Research* **1**, 85-96, (1954).

88 Jortner J. & Noyes R. M. Some Thermodynamic Properties of the Hydrated Electron. *The Journal of Physical Chemistry* **70**, 770-774, (1966).

89 Sehested K., Holcman J., Bjergbakke E. & Hart Edwin J. Ultraviolet Spectrum and Decay of the Ozonide Ion Radical, O_3^-, in Strong Alkaline Solution. *Journal of Physical Chemistry* **86**, 2066-2069, (1982).

90 Jones T. Development of an Effluent Treatment Process for the Silos Direct Encapsulation Plant. *IChemE Sustainable Nuclear Energy Conference*, (2014).

91 Nelson S. M., Newman A. C. D., Tomlinson T. E. & Sutton L. E. A Dielectric Study of the Adsorption of Water by Magnesium Hydroxide. *Transactions of the Faraday Society* **55**, 2186-2202, (1959).

92 Shpak P. A., Kalinichenko A. E., Lytovchenko S. A., Kalinichenko A. I., Legkova V. G. & Bagmut N. N. The Effect of γ-Irradiation on the Structure and Subsequent Thermal Decomposition of Brucite. *Physics and Chemistry of Minerals* **30**, 59-68, (2003).

93 Maroto-Valer M. M. *Developments and Innovation in Carbon Dioxide (CO_2) Capture and Storage Technology, Volume One: Carbon Dioxide (CO_2) Capture, Transport and Industrial Applications*. (Woodhead Publishing, 2010).

94 Siriwardane R. V. & Stevens R. W. Novel Regenerable Magnesium Hydroxide Sorbents for CO_2 Capture at Warm Gas Temperatures. *Industrial & Engineering Chemistry Research* **48**, 2135-2141, (2009).

95 Fricker Kyle J. & Park A. Alissa. Effect of H_2O on $Mg(OH)_2$ Carbonation Pathways for Combined CO_2 Capture and Storage. *Chemical Engineering Science* **100**, 332-341, (2013).

96 Sahoo P., Ishihara S., Yamada K., Deguchi K., Ohki S., Tansho M. *et al.* Rapid Exchange between Atmospheric CO_2 and Carbonate Anion Intercalated within Magnesium Rich Layered Double Hydroxide. *ACS Applied Materials & Interfaces* **6**, 18352-18359, (2014).

97 Stirling A. HCO_3^- Formation from CO_2 at High pH: Ab Initio Molecular Dynamics Study. *The Journal of Physical Chemistry B* **115**, 14683-14687, (2011).

98 Shah Noor S., Khan Javed Ali, Al-Muhtaseb Ala'a H., Sayed Murtaza & Khan Hasan M. Gamma Radiolytic Decomposition of Endosulfan in Aerated Solution: The Role of Carbonate Radical. *Environmental Science and Pollution Research*, 1-10, (2016).

99 Nash K., Mulac W., Noon M., Fried S. & Sullivan J. C. Pulse Radiolysis Studies of U(VI) Complexes in Aqueous Media. *Journal of Inorganic and Nuclear Chemistry* **43**, 897-899, (1981).

100 Holcman J., Bjergbakke E. & Sehested K. The Importance of Radical-Rradical Reactions in Pulse Radiolysis of Aqueous Carbonate/Bicarbonate. *Proceedings of the Tihany Symposium on Radiation Chemistry* **6**, 149-153, (1987).

101 Draganic Z. D., Negron-Mendoza A., Sehested K., Vujosevic S. I., Navarro-Gonzales R., Albarran-Sanchez M. G. *et al.* Radiolysis of Aqueous Solutions of Ammonium Bicarbonate Over a Large Dose Range. *Radiation Physics and Chemistry* **38**, 317-321, (1991).

102 Eriksen T. E., Lind J. & Merényi G. On the Acid-Base Equilibrium of the Carbonate Radical. *Radiation Physics and Chemistry* **26**, 197-199, (1985).

103 Thomas J. K., Gordon Sheffield & Hart Edwin J. The Rates of Reaction of the Hydrated Electron in Aqueous Inorganic Solutions. *Journal of Physical Chemistry* **68**, 1524-1527, (1964).

104 Nehari Shlomo & Rabani Joseph. The Reaction of $H^{\cdot}$ Atoms with OH^{-} in the Radiation Chemistry of Aqueous Solutions. *Journal of Physical Chemistry* **67**, 1609-1613, (1963).

105 Neta P. & Dorfman L. M. Pulse Radiolysis Studies. XIII. Rate Constants for the Reaction of Hydroxyl Radicals with Aromatic Compounds in Aqueous Solutions in *Radiation Chemistry* Vol. 81 *Advances in Chemistry* Ch. 15, 222-230 (American Chemical Society, 1968).

106 Mezyk S. P. & Bartels D. M. Rate Constant and Activation Energy Measurement for the Reaction of Atomic Hydrogen with Methanol, Iodomethane, Iodoethane, and 1-Iodopropane in Aqueous Solution. *The Journal of Physical Chemistry* **98**, 10578-10583, (1994).

107 Anbar M. & Hart E. J. The Reactivity of Aromatic Compounds toward Hydrated Electrons. *Journal of the American Chemical Society* **86**, 5633-5637, (1964).

108 Theard Leslie M. & Burton Milton. Radiolysis of Liquid Methanol and some Methanolic Salt Solutions. *Journal of Physical Chemistry* **67**, 59-64, (1963).

109 Porter Raymond P., Noyes W. & Albert Jr. Photochemical Studies. LIV. Methanol Vapor. *Journal of the American Chemical Society* **81**, 2307-2311, (1959).

110 Motohashi N. & Saito Y. Competitive Measurement of Rate Constants for Hydroxyl Radical Reactions Using Radiolytic Hydroxylation of Benzoate. *Chemical & pharmaceutical bulletin* **41**, 1842-1845, (1993).

111 Adams G. E. & Willson R. L. Pulse Radiolysis Studies on the Oxidation of Organic Radicals in Aqueous Solution. *Transactions of the Faraday Society* **65**, 2981-2987, (1969).

112 Kishore K., Moorthy P. N. & Rao K. N. Reactivity of H_2O_2 with Radiation Produced Free Radicals: Steady State Radiolysis Methods for Estimating the Rate Constants. *International Journal of Radiation Applications and Instrumentation. Part C. Radiation Physics and Chemistry* **29**, 309-313, (1987).

113 Simic M., Neta P. & Hayon E. Pulse Radiolysis Study of Alcohols in Aqueous Solution. *The Journal of Physical Chemistry* **73**, 3794-3800, (1969).

114 Tsang W. Chemical Kinetic Data Base for Combustion Chemistry. Part 2. Methanol. *Journal of Physical and Chemical Reference Data* **16**, 471-508, (1987).

115 Huie R. E. & Clifton C. L. Kinetics of the Self-Reaction of Hydroxymethylperoxyl Radicals. *Chemical Physics Letters* **205**, 163-167, (1993).

116 Schuchmann M. N. & Von Sonntag C. The Rapid Hydration of the Acetyl Radical. A Pulse Radiolysis Study of Acetaldehyde in Aqueous Solution. *Journal of the American Chemical Society* **110**, 5698-5701, (1988).

117 Bothe E., Schulte-Frohlinde D. & von Sonntag C. Radiation Chemistry of Carbohydrates. Part 16. Kinetics of $HO_2^{\cdot}$ Elimination from Peroxyl Radicals Derived from Glucose and Polyhydric Alcohols. *Journal of the Chemical Society, Perkin Transactions 2*, 416-420, (1978).

118 Zimina G.M. & Bakh N.A. Pulse Radiolysis of Ethylene Glycol. Absorption Spectra of the Short-Lived Radicals. *High Energy Chem.* **13**, 187-190, (1979).

119 Thomas J. K. Rates of Reaction of the Hydroxyl Radical. *Transactions of the Faraday Society* **61**, 702-707, (1965).

120 Draganic I. & Marcovic V. Unpublished data (NIST Squib: 1968DRA/MARB). (1968).

121 Orlando J. J. & Tyndall G. S. The Atmospheric Chemistry of the HC(O)CO Radical. *International Journal of Chemical Kinetics* **33**, 149-156, (2001).

122 Ziemer H., Dóbé S., Wagner H. G., Olzman M., Viskolcz B. & Temps F. Kinetics of the Reactions of HCO with H˙ and D˙ Atoms. *Berichte der Bunsengesellschaft für physikalische Chemie* **102**, 897-905, (1998).

123 Temps F. & Wagner H. G. Rate Constants for the Reactions of ˙OH Radicals with CH_2O˙ and HCO˙. *Berichte der Bunsengesellschaft für physikalische Chemie* **88**, 415-418, (1984).

124 Atkinson R., Baulch D. L., Cox R. A., Hampson R. F., Kerr J. A., Rossi M. J. *et al.* Evaluated Kinetic and Photochemical Data for Atmospheric Chemistry: Supplement VI. IUPAC Subcommittee on Gas Kinetic Data Evaluation for Atmospheric Chemistry. *Journal of Physical and Chemical Reference Data* **26**, 1329-1499, (1997).

125 Yee Quee M. J. & Thynne J. C. J. The Photolysis of Organic Esters. *Berichte der Bunsengesellschaft für physikalische Chemie* **72**, 211-217, (1968).

126 Sunaryoy G. R. & Domae M. Numerical Simulation on Effect of Methanol Addition on Coolant Radiolysis in Pressurized Water Reactor. *Journal of Nuclear Science and Technology* **45**, 1261-1274, (2008).

127 Baxendale J. H. & Mellows F. W. The γ-Radiolysis of Methanol and Methanol Solutions. *Journal of the American Chemical Society* **83**, 4720-4726, (1961).

128 Pikaev A. K. & Kartasheva L. I. Radiolysis of Aqueous Solutions of Ethylene Glycol. *International Journal for Radiation Physics and Chemistry* **7**, 395-415, (1975).

129 Ahmad M., Awan M. H. & Mohammad D. γ-Radiolysis of Ethylene Glycol Aqueous Solutions. *Journal of the Chemical Society B: Physical Organic*, 945-946, (1968).

130 Yaylayan V. A., Harty-Majors S. & Ismail A. A. Investigation of the Mechanism of Dissociation of Glycolaldehyde Dimer (2,5-dihydroxy-1,4-dioxane) by FTIR Spectroscopy. *Carbohydrate Research* **309**, 31-38, (1998).

131 Reiff S. C. & LaVerne J. A. Radiation-Induced Chemical Changes to Iron Oxides. *The Journal of Physical Chemistry B* **119**, 7358-7365, (2015).

132 Lousada C. M., Yang M., Nilsson K. & Jonsson M. Catalytic Decomposition of Hydrogen Peroxide on Transition Metal and Lanthanide Oxides. *Journal of Molecular Catalysis A: Chemical* **379**, 178-184, (2013).

133 Rush J. D. B., Benon H. J. Pulse Radiolytic Studies of the Reaction of Perhydroxyl /Superoxide O_2^- with Iron(II)/Iron(III) Ions. The Reactivity of HO_2/O_2^- with Ferric Ions and its Implication on the Occurrence of the Haber-Weiss Reaction. *Journal of Physical Chemistry* **89**, 5062-5066, (1985).

134 Pepper S. E., Borkowski M., Richmann M. K. & Reed D. T. Determination of Ferrous and Ferric Iron in Aqueous Biological Solutions. *Analytica Chimica Acta* **663**, 172-177, (2010).

135 Barb W. G., Baxendale J. H., George P. & Hargrave K. R. Reactions of Ferrous and Ferric Ions with Hydrogen Peroxide. Part II.-The Ferric Ion Reaction. *Transactions of the Faraday Society* **47**, 591-616, (1951).

136 Stuglik Z. & PawełZagórski Z. Pulse Radiolysis of Neutral Iron(II) Solutions: Oxidation of Ferrous Ions by $^{\cdot}OH$ Radicals. *Radiation Physics and Chemistry (1977)* **17**, 229-233, (1981).

137 Fong K.-L., McCay P. B., Poyer J. L., Misra H. P. & Keele B. B. Evidence for Superoxide-Dependent Reduction of Fe^{3+} and its role in Enzyme-Generated Hydroxyl Radical Formation. *Chemico-Biological Interactions* **15**, 77-89, (1976).

138 Baxendale J. H., Dixon R. S. & Stott D. A. Reactivity of Hydrogen Atoms with Fe^{3+}, $FeOH^{2+}$ and Cu^{2+} in Aqueous Solutions. *Transactions of the Faraday Society* **64**, 2398-2401, (1968).

139 Jonah C. D. M., John R.; Matheson, Max S. The Reaction of the Precursor of the Hydrated Electron with Electron Scavengers. *Journal of Physical Chemistry* **81**, 1618-1622, (1977).

Appendix

Radiolysis Model Code

All computational calculations were performed with the software package Facsimile by MCPA Software. The following is a print out of the core water radiolysis model and only includes the reactions of water; other reaction schemes documented in this work can be found on the included CD, as well as the setup files containing initial parameters and associated Python scripts used to manage output data.

```
*-----------------------------------------------------------------------;
*  _    _ ____  _____   _____                 _ _          _            _     ;
* | |  | |__ \ / ____\ |  __ \               | (_)        | |          (_)    ;
* | |__| |  ) | |    | | |__) |__ _  __| | |_  ___ | |_   _ ___ _ ___  ;
* |  __  | / /| |    | |  _  // _` |/ _` | | |/ _ \| | | | / __| / __| ;
* | |  | |/ /_| |____| | | \ | (_| | (_| | | | (_) | | |_| \__ | \__ \ ;
* |_|  |_|____|\_____/  |_|  \_\__,_|\__,_|_|_|\___/|_|\__, |___|_|___/ ;
*                                                        __/ |           ;
*                                                       |___/            ;
*-----------------------------------------------------------------------;
*-----Radiolysis Model for the Radiolysis of Pure Water--------------;
*----------------------Thomas Donoclift-------------------------------;

*Rate constants mainly are from:
 A J Elliot, "Rate constants and G-values
  for the simulation of the radiolysis of
  light water over the range 0 - 300 C"
  AECL-11073, COG-94-167, 1994/2008

 P. Bouniol & E. Bjergbakke "A Comprehensive
  Model to Describe Radiolytic processes
  in Cement Medium" J Nuclear Materials 372 1-15 2008

J.C. Wren, J.M. Ball "LIRIC 3.2 an Updated model for
  Iodine behaviour in the presence of organic impurities"
  Radiation Physics and Chemistry 60 577-596 2001;

EXECUTE OPEN 1 "RadM.out" UNKNOWN;
EXECUTE OPEN 2 "Report.out" UNKNOWN;
EXECUTE OPEN 3 "SetUp.txt" OLD;

EXECUTE OPEN 4 "Flux_A.txt" UNKNOWN;
EXECUTE OPEN 7 "Flux_B.txt" UNKNOWN;
EXECUTE OPEN 8 "Flux_C.txt" UNKNOWN;
EXECUTE OPEN 9 "Flux_D.txt" UNKNOWN;
EXECUTE OPEN 10 "Flux_E.txt" UNKNOWN;
EXECUTE OPEN 11 "FireCount_A.txt" UNKNOWN;
EXECUTE OPEN 12 "FireCount_B.txt" UNKNOWN;
EXECUTE OPEN 14 "TIME.txt" UNKNOWN;
EXECUTE OPEN 15 "FireCount_C.txt" UNKNOWN;
EXECUTE OPEN 16 "FireCount_D.txt" UNKNOWN;
EXECUTE OPEN 17 "FireCount_E.txt" UNKNOWN;
EXECUTE OPEN 19 "TRACE.txt" UNKNOWN;

PERMIT +- ;

*------------------------;
```

```
*These variables are the concentrations of radiolysis
species. Edit initial values in COMPILE INSTANT and
COMPILE INITIAL routines or SetUp.txt;
*---------DEFINE-VARIABLES-------------;
*----CHEMICAL-SPECIES-FOR-H2O-RADIOLYSIS---------------;
VARIABLE
H2O H2O+ H3O+ OH H H2 H2g H2O2 H2O2+ O2 O2g H+
OH- Eaq- O2- O2-- HO2 HO2- O- O-- O3- O Rx O3;

*---------------------------------------;
*------REACTION-COUNTERS-----------------------;
VARIABLE
R0 R1 R2 R3 R4 R5 R6 R7 R8 R9 R10 R11 R12 R13 R14 R15 R16
R17 R18 R19 R20 R21 R22 R23 R24 R25 R26 R27 R28 R29 R30
R31 R32 R33 R34 R35 R36 R37 R38 R39 R40 R41 R42 R43 R44
R45 R46 R47 R48 R49 R50 R51 R52 R53 R54 R55 R56 R57 R58
R59 R60 R61 R62 R63 R64 R65 R66 R67 R68 R69 R70 R71 R72
R73 R74 R75 R76 R77 R78 R79 R80 R81 R82 R83
G0 G1 G2 G3 G4 G5 G6 G7 G8;

*---------DEFINE-PARAMETERS-------------;
PARAMETER
T TK RT TAB DOSER ADOSE
DOSE EVDOSE GEaq- GH GH2 GOH GH2O2 GH+ GOH- G-H2O G+H2O GO2 GO2-
kappH2 kappO2 GHO2 GHO2-
kappO2g H2tot EA MB1 MB2 H2O2T;

INTEGER #RUNt;

*-------------------------;
*This set of perameters concerns radiolysis rates.
G-Values are converted to rates in COMPILE INITIAL.
Rate constants are given the prefix "K"
Arrhenius Pre-exponentials are given the prefix "A"
Activation Energies (-Ea/R) are given the prefix "E"
followed by letters representing reacting species i.e.
KAB = Rate constant of A+B;
*-------------------------;
*A=Eaq-  B=H   C=OH    D=O-
 E=O3-   F=HO2 G=H2O2  H=H2O2+
 I=H2O   J=H+  K=OH-   L=HO2-
 M=O2    N=O2- O=O2--  P=H2O+
 Q=O3    R=H2  S=O;
*-------------------------;

PARAMETER
DW GREaq- GRH GRH2 GROH GRH2O2 GRH+ GROH- GR-H2O GR+H2O
GRO2 GRO2- GRHO2 GRHO2- KAA KAB KAC KAD KAG KAF KAL KAM KAN KBB KBC
KBG KBM KBN KBF KBF2 KBL KCC KCD KCG KCL KCF KCN KDR KDG KDL
KDN KEG KEL KER KEC KED KNN KFN KFNI KFF KFG KI KJK KG
KJL KGK KLI KC KJD KCK KDI KDM KE KF KJN KFK KNI KB KJA
KBK KAI KBI KRC KJNb KCKb KLK KLKb KDD KEJ KBQ KDQ
KCL2 KCQ KNQ KFQ KNG KNE KKQ KLQ KGQ KLG KLN KEC2 KAN2 KAN3;
*-------------------------;
```

```
*----PRE-EXPONENTIAL-FACTORS-------------------;
PARAMETER AAB AAF AAG AAM AAN ABB ABC ABG
ABN ABF ACG ACF ACN ACL ADR ADL AFNI
AFF ADM AE AG AAN2 AGQ AFN ANN ACL2 ABF2
ABL AAD AAL ADG AEG AEL AER AFG AAN3 ACD ALKb;
*-----------------------------------;
*-------ACTIVATION-ENERGIES--------------;
PARAMETER EAB EAF EAG EAM EAN EBB EBC EBG
EBN EBF ECG ECF ECN ECL EDR EDL EFNI
EFF EDM EE EG EAN2 EGQ EFN ENN ECL2 EBF2
EBL EAD EAL EDG EEG EEL EER EFG EAN3 ECD ELKb;
*-------------------------------------;

PARAMETER
pH pHreal pKw pKH2O2 pKOH pKHO2 pKH pKH2O pKHO2- KpH KpO
KfH KrH KfO KrO CONV PcH PcO O2in xO2 Kprot Khydx
TPrint pHsweep Tstart Tend DecTime;
*-----------------------------------------------------------
Below are arrays for storing reaction flux. These are limited to 20
as the output length max is 250 characters. To overcome this clunky
artefact of Facsimile, the arrays can be fed into Facssemble.py to
concatenate them into a single output file.
-----------------------------------------------------------;
PARAMETER <20> Ra; Stores Water Reaction Flux Part A
PARAMETER <20> Rb; Stores Water Reaction Flux Part B
PARAMETER <20> Rc; Stores Water Reaction Flux Part C
PARAMETER <20> Rd; Stores Water Reaction Flux Part D
PARAMETER <10> Re; Stores Water Reaction Flux Part E
PARAMETER <2> GR; Stores Gas Partition Flux

*-------------------------;
*--PARAMETERS-FOR-GAS-PARTITION--------------;

PARAMETER
DaqH2 DgH2 DaqO2 DgO2 daq dg
vaqH2 vgH2 vaqO2 vgO2 vintH2 vintO2
KpH2 KpO2 vtot
Aint Vl Vg Vr Dose EqR ;

*---------------INITIALISE-PARAMETERS--------              ;
*Concentrations of specis are given as Mol/l.              ;
*T is Temp in C - TK is Temp in K                          ;
*pHin is the initial pH, xO2 is the fraction of O2         ;
*pHreal is the calculated pH at any given time            ;
*DW is density of water depending on temperature.         ;
*DS is the density of the whole solution                  ;
*Vl and Vg is the Volume of liqud and gas phases in L     ;
*DOSER is the dose rate in Gy/min                         ;
*ADOSE is the conversion of dose rate to sets of 100eV/l/s;
```

```
COMPILE INSTANT;
*----PARAMETERS-FROM-SETUP-FILE-----;
READ 3 DOSER;
READ 3 #RUNt;
READ 3 Tstart;
READ 3 Tend;
READ 3 pH;
READ 3 xO2;
READ 3 Vl;
READ 3 Vg;
READ 3 Aint;
READ 3 DaqH2;
READ 3 DgH2;
READ 3 DaqO2;
READ 3 DgO2;
READ 3 daq;
READ 3 dg;
READ 3 KpH2;
READ 3 KpO2;
*---ADDITIONAL-PARAMETERS----;
T = Tstart;
TK = T + 273.15;
TAB = 1/TK;
RT = 8.314*TK;
DW = (0.999 + 1.094E-4 * T - 7.397E-6 * T@2
+ 2.693E-8 * T@3 - 4.714E-11 * T@4);
ADOSE = ((DOSER * 6.2415E16) / 60) * DW ; 100 eV/s/l for use with Gy/min
TPrint = (FLOAT(#RUNt) - 1) * 60;
EA = EXP(18800*((1/298.15-1/TK)/8.314));
WRITE 2 = 4,%;
WRITE 3 = 7,%;
WRITE 4 = 8,%;
WRITE 7 = 10,%;
WRITE 8 = 9,%;
WRITE 12 = 14,%;
WRITE 1 = 2, "WATER RADIOLYSIS MODEL - DEBUG REPORT" % ;
*------INITIAL-SPECIES-CONCENTRATIONS-----;
READ 3 Eaq-;
READ 3 H2;
READ 3 O2;
READ 3 H2O2;
H2O = 55.3*DW;
O2g = 101320 * xO2 / (1000 * RT);
H2g = 1E-22; mass transfer - zero will cause floating point overflow

H+ = 10@(-1*pH); H+ Activity (Effective concentration)
OH- = 10@(-1*(14-pH));
```

```
*------------ARRHENIUS-PARAMETERS-----------------------------;

*----PRE-EXPONENTIAL-FACTORS-------------------;
AAB = 1.14E13;
AAF = 2.4636E12;
AAG = 7.7E12;
AAM = 2.479E12;
AAN = 2.4636E12;
ABB = 2.7E12;
ABC = 4.26E11;
ABG = 1.79E11;
ABN = 5.17E12;
ABF = 5.17E12;
ACG = 7.68E9;
ACF = 1.29E11;
ACN = 8.77E11;
ACL = 1.00E12;
ADR = 2.32E10;
ADL = 1.45E13;
AFNI = 2.63E9;
AFF = 2.78E9;
ADM = 3.41E11;
AE = 3.20E11;
AG = 3.171E4;
AAN2 = 3.1E12;
AGQ = 2.8E11;
AFN = 2.44E9;
ANN = 4.89E8;
ACL2 = 4.5E12;
ABF2 = 7.2E11;
ABL = 4.2E13;
AAD = 5.6E11;
AAL = 1.75E12;
ADG = 3.00E11;
AEG = 1.59E6;
AEL = 8.87E5;
AER = 2.49E5;
AFG = 3.7;
AAN3 = 2.567E13;
ACD = 1.7E11;
ALKb = 2.95E8;
*-----------------------------;
*------ACTIVATION-ENERGIES-Ea/R----;
EAB = 1795.7;
EAF = 1563.6;
EAG = 1889.6;
EAM = 1401.5;
EAN = 1563.6;
EBB = 1867.5;
EBC = 1091.9;
EBG = 2533.6;
EBN = 1824.2;
EBF = 1824.2;
ECG = 1661.4;
ECF = 799.2;
ECN = 1306.2;
ECL = 1434.6;
EDR = 1550.5;
EDL = 2928.5;
```

```
EFNI = 974.3;
EFF = 2416.4;
EDM = 1344.9;
EE = 5552.1;
EG = 7818.1;

*------ACTIVATION-ENERGIES---Ea-J--;
EAN2 = 13600.0;
EGQ = 73500.0;
EFN = 8600.0;
ENN = 52590.0;
ECL2 = 15600.0;
EBF2 = 10600.0;
EBL = 25600.0;
EAD = 7900.0;
EAL = 15400.0;
EDG = 15600.0;
EEG = 18840.0;
EEL = 18840.0;
EER = 18840.0;
EFG = 20000.0;
EAN3 = 18800.0;
ECD = 7700.0;
ELKb = 14200.0;
*--------------------------------;
*---------OTHER-LITERATURE-RATE-CONSTANTS-------------------------;
KLG = 4.5E-4                              ; F.R.Duke, T.W.Haas 1961
KLQ = 5.5E6                               ; J.Staehelin, J. Hoigne 1982
KKQ = 4.8E1                               ; L.Forni, E.J. Hart 1982
KFQ = 5.0E8                               ; Pastina, La Verne 2001
KNQ = 1.5E9                               ; E.J. Hart 1983
KNE = 1.0E4                               ; Pastina, La Verne 2001
KNG = 1.3E-1                             ; J.Weinstein, B.Bielski 1979
KLN = 8.23E-2                            ; P.Bouniol E.Bjergbakke 2008
KCQ = 1.1E8                              ; K. Sehested, E.J. Hart 1984
KEC2 = 2.5E9                             ; K. Sehested, E.J. Hart 1984
KDQ = 1.0E9                              ; E. Bjergbakke, H. Christensen
KBQ = 2.2E10                             ; E.J. Hart 1983
*KCD = 2.0E10                            ;
KDN = 6.00E8                             ;
KEC = 6.0E9                              ; Sehested, Holcman, Hart 1984
(269)
*KEC = 8.50E9                            ; P. Bouniol, E. Bjergbakke
*KDD = 8.4E9                             ; Adams G.E. Boag J.W.
KDD = 1.0E8                              ;
KED = 7.0E8                              ; Hart E.J. 1984
KEJ = 9.0E10                             ; Hart E.J.
KLK = 3.506E5                            ;
KLKb = 9.61E5                            ;
**;

*////////////////////////////////////////////////////////////;
*-GENERAL-ROUTINE-CONTINUALLY-ITTERATES-THROUGHOUT-CALCULATION-;
*\\\\\\\\\\\\\\\\\\\\\\\\\\\\\\\\\\\\\\\\\\\\\\\\\\\\\\\\\\\\\\\\;
```

```
COMPILE GENERAL;

*------TEMPERATURE-RAMPING-ROUTINE----------------;
TK = T + 273.15;
TAB = 1/TK;
RT = 8.314*TK;
DecTime = TIME / 3600;
T = (1.1414 * DecTime@3 - 8.0383 * DecTime@2
+ 19.256 * DecTime + 22.918);
IF(T - Tend)2,1,1;
LABEL 1;
T = Tend;
LABEL 2;
*----------------------;

H2O2T = H2O2 + HO2- + O2--; Total peroxide for output use

*------------------SETUP-OF-EQUILIBRIA---------------------------------;
pKw = (14.947 - 4.273E-2 * T + 2.115E-4 * T@2
 - 5.786E-7 *T@3 + 7.529E-10 * T@4);
pKH2O2 = (12.383 - 3.020E-2 * T + 1.70E-4 * T@2
 - 5.151E-7 * T@3 + 6.96E-10 * T@4);
pKOH = (12.383 - 3.020E-2 * T + 1.70E-4 * T@2
 - 5.151E-7 * T@3 + 6.96E-10 * T@4);
pKHO2 = (4.943 - 6.23E-3 * T + 4.125E-5 * T@2
 - 8.182E-9 * T@3);
pKH = (10.551 - 4.43E-2 * T + 1.902E-4 * T@2
 - 4.661E-7 * T@3 + 5.98E-10 * T@4);
pKH2O = (16.69 - 4.43E-2 * T + 2.071E-4 * T@2
 - 5.594E-7 * T@3 + 7.161E-10 * T@4);
Kprot = (3.41E10 + 2.75E8 * T + 1.24E7 * T@2
 - 6.23E4 * T@3 + 1.31E2 * T@4);
Khydx = (7.22E9 + 1.62E8 * T + 2.4E6 * T@2
 - 7.81E3 * T@3 + 10.6 * T@4) ;
pKHO2- = 16.5; see Bouniol 2001



*--------------------PARTITION-OF-O2-AND-H2---------------------;
* It should be noted that this routine is only valid for        ;
* a liquid to gas ratio of 1. See Chapter 3 for details         ;
*---------DIFFUSIVITY-WITH-TEMPERATURE---------;
DaqO2 = (2E-9 * T@2 + 4E-7 * T + 1E-5);
DaqH2 = (1E-8 * T@2 + 4E-7 * T + 3E-5);
DgO2 = (1E-6 * T@2 + 1.2E-3 * T + 0.2073);
DgH2 = (5E-6 * T@2 + 4.7E-3 * T + 0.7719);
*-----HENRY'S-COEFFICIENT-WITH-TEMPERATURE--------------------;
KpH2 = (TK * (7.8E-4 * EXP(543*((1/TK) - (1/298.15))))) / 12.2 ;
KpO2 = (TK * (1.3E-3 * EXP(1650*((1/TK) - (1/298.15))))) / 12.2;


*---H2----;
vgH2 = DgH2/dg;
vaqH2 = DaqH2/daq;
vintH2 = 1/(1/vaqH2 + KpH2/vgH2);
H2tot = H2 + H2g;
```

```
*---O2----;
vgO2 = DgO2/dg;
vaqO2 = DaqO2/daq;
vintO2 = 1/(1/vaqO2 + KpO2/vgO2);
vtot = 1/((1/(vaqO2))+(1/(vgO2*KpO2)));

*--------PARAMETER-EVOLUTION--------------;
kappH2 = vintH2*(Aint/Vl)*(1 - KpH2*(H2g/H2));
kappO2 = vintO2*(Aint/Vl)*(1 - KpO2*(O2g/O2));

Dose = DOSER * (TIME / 60);
pHreal = -LOG10( H+ );


*--------------------G-VALUES-------------------------;
*G-Values with temperature dependency ONLY;
*G-Values are initially obtained from literature molec /100eV;
*G-Values are converted to rates later;
*GEaq- = 2.641 + 4.162E-3 * T + 9.093E-6 * T**2 - 4.717E-8 * T**3;
*GH2 = 0.419 + 8.72E-4 * T - 4.971E-6 * T**2 + 1.503E-8 * T**3;
*GOH = 2.531 + 1.134E-2 * T - 1.269E-5 * T**2 + 3.513E-8 * T**3;
*GH2O2 = 0.752 - 1.62E-3 * T;
*GH = 0.556 + 2.198E-3 * T - 1.184E-5 * T**2 + 5.223E-8 * T**3;
*GH+ = GEaq-;
*G-H2O = GOH + 2*GH2O2;

*-----------------------------------------------------;
*------------G-VALUES-FROM-MULTIPLE-POLYNOMIAL-REGRESSION-----;
*Multiple polynomial regression was used to combine data that measured
primary yields as a function of temperature AND as a function of pH;
GEaq- = 2.798 + 2.85E-3 * T - 2.514E-2 * pHreal;
GH2 = 3.8781E-1 + 8.288E-4 * T + 5.988E-4 * pHreal;
GOH = 2.43146 + 1.111E-2 * T - 1.2E-3 * pHreal;
GH = 4.444E-1 + 3.67E-3 * T - 2.378E-4 * pHreal;
GH+ = GEaq-;
GH2O2 = 0.5*(GH + GEaq- + (2 * GH2) - GOH); Material Balance
G-H2O = GOH + 2*GH2O2;

MB1 = GH + GEaq- + (2 * GH2); Diagnostic Material Balance Variables
MB2 = GOH + (2 * GH2O2);



*-------------------G-VALUES--AS--RATES--------------;
GREaq- = (ADOSE * GEaq-)/6.022E23  ;
GRH = (ADOSE * GH)/6.022E23        ;
GRH2 = (ADOSE * GH2)/6.022E23      ;
GROH = (ADOSE * GOH)/6.022E23      ;
GRH2O2 =(ADOSE * GH2O2)/6.022E23   ;
GRH+ = (ADOSE * GH+)/6.022E23      ;
GROH- = (ADOSE * GOH-)/6.022E23    ;
GR-H2O = (ADOSE * G-H2O)/6.022E23  ;
GRO2 = (ADOSE * GO2)/6.022E23      ;
GRO2- = (ADOSE * GO2-)/6.022E23    ;
GRHO2 = (ADOSE * GHO2)/6.022E23    ;
GRHO2- = (ADOSE * GHO2-)/6.022E23  ;
```

```
*------REACTION-RATES-WITH-TEMP-DEPENDENCY--;
*--------POLYNOMIAL-EQUATIONS----------------;
KAA = 10@(12.281 - 3.768E2 * TAB - 6.673E4 * TAB@2 - 1.075E7 * TAB@3);
KAC = 10@(13.123 - 1.023E3 * TAB + 7.634E4 * TAB@2)                   ;
KBM = 10@(10.704 + 2.840E2 * TAB - 1.37E5 * TAB@2)                    ;
KCC = 10@(8.054 + 2.193E3 * TAB - 7.395E5 * TAB@2 + 6.87E7 * TAB@3)   ;
KJK = 10@(20.934 - 1.236E4 * TAB + 6.364E6 * TAB@2
- 1.475E9 * TAB@3 + 1.237E11 * TAB@4)                                 ;

KJN = 10@(16.41 - 4.888E3 * TAB + 1.622E6 * TAB@2 - 2.004E8 * TAB@3) ;
KCK = 10@(13.339 - 2.22E3 * TAB + 7.333E5 * TAB@2 - 1.065E8 * TAB@3) ;
KJA = 10@(39.127 - 3.888E4 * TAB + 2.054E7 * TAB@2 - 4.899E9 * TAB@3
+ 4.376E11 * TAB@4)                                                   ;

KBK = 10@(22.970 - 1.971E4 * TAB + 1.137E7 * TAB@2 - 2.991E9 * TAB@3
 + 2.803E11 * TAB@4)                                                  ;

KBI = 10@(9.408 - 2.827E3 * TAB - 3.792E5 * TAB@2)                    ;
KRC = 10@(-11.556 + 3.2546E4 * TAB - 1.8623E7 * TAB@2
+ 4.5543E9 * TAB@3 - 4.1364E11 * TAB@4)                               ;


*------------ARRHENIUS-EQUATIONS------------------;
*----------Ea/R--------------------;
KAB = AAB*(EXP(-EAB/TK))               ;
KAF = AAF*(EXP(-EAF/TK))               ;
KAG = AAG*(EXP(-EAG/TK))               ;
KAM = AAM*(EXP(-EAM/TK))               ;
KAN = AAN*(EXP(-EAN/TK))               ;
KBB = ABB*(EXP(-EBB/TK))               ;
KBC = ABC*(EXP(-EBC/TK))               ;
KBG = ABG*(EXP(-EBG/TK))               ;
KBN = ABN*(EXP(-EBN/TK))               ;
KBF = ABF*(EXP(-EBF/TK))               ;
KCG = ACG*(EXP(-ECG/TK))               ;
KCF = ACF*(EXP(-ECF/TK))               ;
KCN = ACN*(EXP(-ECN/TK))               ;
KCL = ACL*(EXP(-ECL/TK))               ;
KDR = ADR*(EXP(-EDR/TK))               ;
KDL = ADL*(EXP(-EDL/TK))               ;
KFNI = AFNI*(EXP(-EFNI/TK))            ;
KFF = AFF*(EXP(-EFF/TK))               ;
KDM = ADM*(EXP(-EDM/TK))               ;
KE = AE*(EXP(-EE/TK))                  ;
KG = AG*(EXP(-EG/TK))                 ;


*---------Ea-----------------;
KAN2 = AAN2*EXP(-EAN2/RT)              ;
KGQ = AGQ*EXP(-EGQ/RT)                 ; K.Sehested, E.J. Hart,1992
KFN = AFN*EXP(-EFN/RT)                 ; B.Bielski, A.Ross 1985
KNN = ANN*EXP(-ENN/RT)                 ; Eliot
KCL2 = ACL2*EXP(-ECL2/RT)              ; Eliot
KBF2 = ABF2*EXP(-EBF2/RT)              ; Eliot
KBL = ABL*EXP(-EBL/RT)                 ; S.P. Mezyk, D.M. Bartels
KAD = AAD*EXP(-EAD/RT)                 ; Eliot
KAL = AAL*EXP(-EAL/RT)                 ;
KDG = ADG*EXP(-EDG/RT)                 ;
KEG = AEG*EA                           ;Wren & Ball
```

```
KEL = AEL*EA                              ;Wren & Ball
KER = (AER*EA)                            ;Wren (Suggests *8 correction)
KFG = 5.0E-1                              ;
KAN3 = AAN3*EXP(-EAN3/RT)                 ;
KCD = ACD*EXP(-ECD/RT)                    ;

*-----------EQUILIBRIA----------------------------------------;
KCKb = KCK *((10@(-pKH2O))/(10@(-pKOH)))                      ;
KI = KJK*(10@-pKw)                                            ;
KF = KJN * (10@-pKHO2)                                        ;
KJL = KJN                                                     ;
KGK = KCK                                                     ;
KDI = KCK*((10@-pKH2O)/(10@-pKOH))                            ;
KLI = KCK*((10@-pKH2O)/(10@-pKH2O2))                          ;
KJD = KJN                                                     ;
KC = KJD*(10@-pKOH)                                           ;
KFK = KCK                                                     ;
KNI = KFK*((10@-pKH2O)/(10@-pKHO2))                           ;
KB = KJA*(10@-pKH)                                            ;
KAI = KBK*((10@-pKH2O)/(10@-pKH))                             ;
KJNb = KJN*(10@-pKH2O2)*((10@(-pKw))/(10@(-pKHO2)))           ;
**; //GENERAL

*////////////////////////////////////////////////////////////;
*-------EQUATIONS-ROUTINE-CONTAINS-RADIOLYSIS-CHEMISTRY--------;
*\\\\\\\\\\\\\\\\\\\\\\\\\\\\\\\\\\\\\\\\\\\\\\\\\\\\\\\\\\\\\;

COMPILE EQUATIONS;
*------INITIAL-SPECIES-GENERATION---------------------------;
Ra<0>%GREaq-       : = Eaq- + G0                                  ;
Ra<1>%GRH          : = H    + G1                                  ;
Ra<2>%GRH2         : = H2   + G2                                  ;
Ra<3>%GROH         : = OH   + G3                                  ;
Ra<4>%GRH2O2       : = H2O2 + G4                                  ;
Ra<5>%GRH+         : = H+   + G5                                  ;
Ra<6>%GROH-        : = OH-  + G6                                  ;
Ra<7>%GR-H2O/H2O   : H2O =    G7                                  ;
*----------REACTIONS-------------------------;
Ra<8>%KAA/(H2O*H2O):   Eaq- + Eaq- + H2O + H2O = H2 + OH- + OH- + R0 ;
Ra<9>%KAB/H2O      :   Eaq- + H + H2O = H2 + OH- + R1                 ;
Ra<10>%KAC         :   Eaq- + OH = OH- + R2                           ;
Ra<11>%KAD/H2O     :   Eaq- + H2O + O- = OH- + OH- + R3               ;
Ra<12>%KAG         :   Eaq- + H2O2 = OH- + OH + R4                    ;
Ra<13>%KAF         :   Eaq- + HO2 = HO2- + R5                         ;
Ra<14>%KAL         :   Eaq- + HO2- = O- + OH- + R6                    ;
Ra<15>%KAM         :   Eaq- + O2 = O2- + R7                           ;
Ra<16>%KAN         :   Eaq- + O2- = O2-- + R8                         ;
Ra<17>%KBB         :   H + H = H2 + R9                                ;
Ra<18>%KBC         :   H + OH = H2O + R10                             ;
Ra<19>%KBG         :   H + H2O2 = OH + H2O + R11                      ;
Rb<0>%KBM          :   H + O2 = HO2 + R12                             ;
Rb<1>%KBN          :   H + O2- = HO2- + R13                           ;
Rb<2>%KBF          :   H + HO2 = OH + OH + R14                        ;
Rb<3>%KBL          :   H + HO2- = OH + OH- + R15                      ;
Rb<4>%KBQ          :   H + O3 = OH + O2 + R16                         ;
Rb<5>%KCC          :   OH + OH = H2O2 + R17                           ;
Rb<6>%KCG          :   OH + H2O2 = H2O + HO2 + R18                    ;
Rb<7>%KCL          :   OH + HO2- = OH- + HO2 + R19                    ;
Rb<8>%KCF          :   OH + HO2 = H2O + O2 + R20                      ;
```

```
Rb<9>%KCN          :   OH + O2- = OH- + O2 + R21                    ;
Rb<10>%KCQ         :   OH + O3 = O2 + HO2 + R22                     ;
Rb<11>%KEG         :   O3- + H2O2 = O2- + O2 + H2O + R23            ;
Rb<12>%KEL         :   O3- + HO2- = O2- + O2 + OH- + R24            ;
Rb<13>%KER         :   O3- + H2 = O2 + H + OH- + R25                ;
Rb<14>%KEC         :   O3- + OH = HO2 + O2- + R26                   ;
Rb<15>%KEC2        :   O3- + OH = OH- + O3 + R27                    ;
Rb<16>%KEJ         :   O3- + H+ = OH + O2 + R28                     ;
Rb<17>%KNN         :   O2- + O2- = O2 + O2-- + R29                  ;
Rb<18>%KLN         :   O2- + HO2- = O2 + OH- + O- + R30             ;
Rb<19>%KNG         :   O2- + H2O2 = O2 + OH + OH- + R31             ;
Rc<1>%KFN          :   O2- + HO2 = O2 + HO2- + R32                  ;
Rc<2>%KNE          :   O2- + O3- = O-- + O2 + O2 + R33              ;
Rc<3>%KNQ          :   O2- + O3 = O2 + O3- + R34                    ;
Rc<4>%KFF          :   HO2 + HO2 = H2O2 + O2 + R35                  ;
Rc<5>%KFG          :   HO2 + H2O2 = O2 + H2O + OH + R36             ;
Rc<6>%KFQ          :   HO2 + O3 = OH + O2 + O2 + R37                ;
Rc<7>%KLG          :   H2O2 + HO2- = H2O + O2 + OH- + R38           ;
Rc<8>%KKQ          :   O3 + OH- = O2 + HO2- + R39                   ;
Rc<9>%KLQ          :   O3 + HO2- = O2 + OH + O2- + R40              ;
Rc<10>%KGQ         :   O3 + H2O2 = O2 + OH + HO2 + R41              ;

*------------------ADDITIONAL-WATER-CHEMISTRY-------------------------;
Rc<12>%2.00E10   :   H + O- = OH- + R42    ;Bjergbakke, Draganic,
Sehested,
Rc<13>%1.6E10    :   O3- + Eaq- = OH- + OH- + O2 + R43; Pastina & La
Verne
Rc<14>%3.6E10    :      O3 + Eaq- = O3- + R44                   ; NIST
Rc<16>%2.3E-7    :      H2O2 = OH + OH + R45         ;Yakabuskie et al.
Rc<17>%1.0E10/H2O     :      O-- + H2O = OH- + OH- + R46             ;
Bouniol and Bjergbakke 2008

*----------------ALKALI-REACTIONS-----------------;
Re<2>%KDR          :    O- + H2 = H + OH- + R47                     ;
Re<3>%KDG          :    O- + H2O2 = OH- + HO2 + R48                 ;
Re<4>%KDL          :    O- + HO2- = O2- + OH- + R49                 ;
Re<5>%KDN          :    O- + O2- = O-- + O2 + R50                   ;
Re<6>%KDD          :    O- + O- = O2-- + R51                        ;
Re<7>%KCD          :    O- + OH = HO2- + R52                        ;
Re<8>%KED          :    O- + O3- = O2- + O2- + R53                  ;
Re<9>%KDQ          :    O- + O3 = O2- + O2 + R54                    ;

*----------EQUILIBRIUM-REACTIONS--------------------;
Rc<18>%KI/H2O                :     H2O = H+ + OH- + R55             ;
Rc<19>%KJK                   :     H+ + OH- = H2O + R56             ;

Rd<0>%KJN*10@(-pKH2O2)       :     H2O2 = H+ + HO2- + R57           ;
Rd<1>%KJN                    :     H+ + HO2- = H2O2 + R58           ;

Rd<2>%KCK                    :     H2O2 + OH- = HO2- + H2O + R59    ;
Rd<3>%KLI/H2O                :     HO2- + H2O = H2O2 + OH- + R60    ;


Rd<4>%KLK                    :     HO2- + OH- = O2-- + H2O + R61    ;
Rd<5>%KLKb/H2O               :     O2-- + H2O = HO2- + OH- + R62    ;

Rd<6>%KJN*10@(-pKOH)         :     OH = H+ + O- + R63               ;
Rd<7>%KJN                    :     H+ + O- = OH + R64               ;
```

```
Rd<8>%KCK                    :     OH + OH- = O- + H2O + R65        ;
Rd<9>%KCKb/H2O               :     O- + H2O = OH + OH- + R66        ;

Rd<10>%KDM                   :     O- + O2 = O3- + R67              ;
Rd<11>%KE                    :     O3- = O- + O2 + R68              ;

Rd<12>%KF                    :     HO2 = H+ + O2- + R69             ;
Rd<13>%KJN                   :     H+ + O2- = HO2 + R70             ;

Rd<14>%KFK                   :     HO2 + OH- = O2- + H2O + R71      ;
Rd<15>%KNI/H2O               :     O2- + H2O = HO2 + OH- + R72      ;

Rd<16>%KB                    :    H = H+ + Eaq- + R73               ;
Rd<17>%KJA                   :    H+ + Eaq- = H + R74               ;

Rd<18>%KBK                   :    H + OH- = Eaq- + H2O + R75        ;
Rd<19>%KAI/H2O               :    Eaq- + H2O = H + OH- + R76        ;

Re<0>%KBI/H2O                :    H + H2O = H2 + OH + R77           ;
Re<1>%KRC                    :    H2 + OH = H + H2O + R78           ;



*---------------MASS-TRANSFER----------------------;
GR<0>%kappH2                 :    H2 = H2g + R79                    ;
GR<1>%kappO2                 :    O2 = O2g + R80                    ;

**;

*////////////////////////////;
*-------OUTPUTS-ROUTINE-------;
*\\\\\\\\\\\\\\\\\\\\\\\\\\\\;

SETPSTREAM 3 1 20;
OH H H2 H2g H2O2 O2 O2g H+ OH- Eaq-
O2- O2-- HO2 HO2- O- O-- O3- O O3;
**;

SETPSTREAM 4 11 20;
R0 R1 R2 R3 R4 R5 R6 R7 R8 R9 R10 R11 R12 R13 R14 R15 R16
R17 R18 R19;
**;

SETPSTREAM 5 12 20;
R20 R21 R22 R23 R24 R25 R26 R27 R28 R29 R30
R31 R32 R33 R34 R35 R36 R37 R38 R39;
**;

SETPSTREAM 6 15 20;
R40 R41 R42 R43 R44 R45 R46 R47 R48 R49
R50 R51 R52 R53 R54 R55 R56 R57 R58 R59
;
**;

SETPSTREAM 7 16 20;
R60 R61 R62 R63 R64 R65 R66 R67 R68 R69
R70 R71 R72 R73 R74 R75 R76 R77 R78 R79;
**;
```

```
SETPSTREAM 8 17 20;
R80 R81 R82 R83 G1 G2 G3
G4 G5 G6 G7 G8;
**;

COMPILE OUT;
PSTREAM 3;
PSTREAM 4;
PSTREAM 5;
PSTREAM 6;
PSTREAM 7;
PSTREAM 8;
WRITE 2 ?250, (N20, E10, 2), Ra %;
WRITE 3 ?250, (N20, E10, 2), Rb %;
WRITE 4 ?250, (N20, E10, 2), Rc %;
WRITE 8 ?250, (N20, E10, 2), Rd %;
WRITE 7 ?250, (N10, E10, 2), Re %;
WRITE 10, (N2, E10, 2), GR %;
WRITE 12, (E10, 2), TIME %;
**;

WHENEVER
TIME = TPrint Call Report;
TIME = 0 + 600 * #RUNt % CALL OUT;
**;
*------------DEBUG-REPORT--------------;
*-Contains a list of all parameters to
confirm that values are correct.-;
COMPILE Report;
WRITE 1, "THIS REPORT IS GENERATED AT ", TPrint, " SECONDS", % ;
WRITE 1, "RUNt = ", #RUNt % ;
WRITE 1, "KpH2 = ", (E12, 3), KpH2 %;
WRITE 1, "KpO2 = ", (E12, 3), KpO2 %;
WRITE 1, "pH = ", (F6, 1), pH % ;
WRITE 1, "Temperature = ", (F6, 1), T, " C", %;
WRITE 1, "Dose Rate = ", (F6, 1), DOSER, " Gy/min", %;
WRITE 1, "Vg/Vl Ratio = ", (F6, 2), Vr %;
WRITE 1, "Run Time = ", (F12, 2), #RUNt, " Mins", %;
WRITE 1, "Oxygen Fraction = ", (F6, 3), xO2 %;
WRITE 1, "G-VALUES" % ;
WRITE 1, "G(Eaq-) = ", (F6, 3), GEaq- % ;
WRITE 1, "G(H) = ", (F6, 3), GH % ;
WRITE 1, "G(H2) = ", (F6, 3), GH2 % ;
WRITE 1, "G(OH) = ", (F6, 3), GOH % ;
WRITE 1, "G(H2O2) = ", (F6, 3), GH2O2 % ;
WRITE 1, "G(H+) = ", (F6, 3), GH+ % ;
WRITE 1, "G(-H2O) = ", (F6, 3), G-H2O %;
WRITE 1, "G-VALUES AS RATES MOL/L/S", %;
WRITE 1, "GREaq- = ", (E12, 3), GREaq- %;
WRITE 1, "GRH = ", (E12, 3), GRH %;
WRITE 1, "GRH2 = ", (E12, 3), GRH2 %;
WRITE 1, "GROH = ", (E12, 3), GROH %;
WRITE 1, "GRH2O2 = ", (E12, 3), GRH2O2 %;
WRITE 1, "GRH+ = ", (E12, 3), GRH+ %;
WRITE 1, "GR-H2O = ", (E12, 3), GR-H2O %;
WRITE 1, "RATE CONSTANTS:" % ;
WRITE 1, "KAA = ", (E12, 3), KAA % ;
WRITE 1, "KAB = ", (E12, 3), KAB % ;
```

```
WRITE 1, "KAC = ", (E12, 3), KAC % ;
WRITE 1, "KAD = ", (E12, 3), KAD % ;
WRITE 1, "KAG = ", (E12, 3), KAG % ;
WRITE 1, "KAF = ", (E12, 3), KAF % ;
WRITE 1, "KAL = ", (E12, 3), KAL % ;
WRITE 1, "KAM = ", (E12, 3), KAM % ;
WRITE 1, "KAN = ", (E12, 3), KAN % ;
WRITE 1, "KBB = ", (E12, 3), KBB % ;
WRITE 1, "KBC = ", (E12, 3), KBC % ;
WRITE 1, "KBG = ", (E12, 3), KBG % ;
WRITE 1, "KBM = ", (E12, 3), KBM % ;
WRITE 1, "KBN = ", (E12, 3), KBN % ;
WRITE 1, "KBF = ", (E12, 3), KBF % ;
WRITE 1, "KBF2 = ", (E12, 3), KBF2 % ;
WRITE 1, "KBL = ", (E12, 3), KBL % ;
WRITE 1, "KBQ = ", (E12, 3), KBQ % ;
WRITE 1, "KCC = ", (E12, 3), KCC % ;
WRITE 1, "KCD = ", (E12, 3), KCD % ;
WRITE 1, "KCG = ", (E12, 3), KCG % ;
WRITE 1, "KCL = ", (E12, 3), KCL % ;
WRITE 1, "KCF = ", (E12, 3), KCF % ;
WRITE 1, "KCN = ", (E12, 3), KCN % ;
WRITE 1, "KCQ = ", (E12, 3), KCQ % ;
WRITE 1, "KDR = ", (E12, 3), KDR % ;
WRITE 1, "KDG = ", (E12, 3), KDG % ;
WRITE 1, "KDL = ", (E12, 3), KDL % ;
WRITE 1, "KDN = ", (E12, 3), KDN % ;
WRITE 1, "KEG = ", (E12, 3), KEG % ;
WRITE 1, "KEL = ", (E12, 3), KEL % ;
WRITE 1, "KER = ", (E12, 3), KER % ;
WRITE 1, "KEC = ", (E12, 3), KEC % ;
WRITE 1, "KED = ", (E12, 3), KED % ;
WRITE 1, "KNN = ", (E12, 3), KNN % ;
WRITE 1, "KFN = ", (E12, 3), KFN % ;
WRITE 1, "KFNI = ", (E12, 3), KFNI % ;
WRITE 1, "KFF = ", (E12, 3), KFF % ;
WRITE 1, "KFG = ", (E12, 3), KFG % ;
WRITE 1, "KI = ", (E12, 3), KI % ;
WRITE 1, "KJK = ", (E12, 3), KJK % ;
WRITE 1, "KG = ", (E12, 3), KG % ;
WRITE 1, "KJL = ", (E12, 3), KJL % ;
WRITE 1, "KGK = ", (E12, 3), KGK % ;
WRITE 1, "KLI = ", (E12, 3), KLI % ;
WRITE 1, "KC = ", (E12, 3), KC % ;
WRITE 1, "KJD = ", (E12, 3), KJD % ;
WRITE 1, "KCK = ", (E12, 3), KCK % ;
WRITE 1, "KDI = ", (E12, 3), KDI % ;
WRITE 1, "KDM = ", (E12, 3), KDM % ;
WRITE 1, "KE = ", (E12, 3), KE % ;
WRITE 1, "KF = ", (E12, 3), KF % ;
WRITE 1, "KJN = ", (E12, 3), KJN % ;
WRITE 1, "KFK = ", (E12, 3), KFK % ;
WRITE 1, "KNI = ", (E12, 3), KNI % ;
WRITE 1, "KB = ", (E12, 3), KB % ;
WRITE 1, "KJA = ", (E12, 3), KJA % ;
WRITE 1, "KBK = ", (E12, 3), KBK % ;
WRITE 1, "KAI = ", (E12, 3), KAI % ;
WRITE 1, "KBI = ", (E12, 3), KBI % ;
WRITE 1, "KRC = ", (E12, 3), KRC % ;
```

```
WRITE 1, "KJNb = ", (E12, 3), KJNB % ;
WRITE 1, "KCKb = ", (E12, 3), KCKb % ;
WRITE 1, "KLK = ", (E12, 3), KLK % ;
WRITE 1, "KLKb = ", (E12, 3), KLKb % ;
WRITE 1, "KDD = ", (E12, 3), KDD % ;
WRITE 1, "KEJ = ", (E12, 3), KEJ % ;
WRITE 1, "KBQ = ", (E12, 3), KBQ % ;
WRITE 1, "KDQ = ", (E12, 3), KDQ % ;
WRITE 1, "KCL2 = ", (E12, 3), KCL2 % ;
WRITE 1, "KCQ = ", (E12, 3), KCQ % ;
WRITE 1, "KNQ = ", (E12, 3), KNQ % ;
WRITE 1, "KFQ = ", (E12, 3), KFQ % ;
WRITE 1, "KNG = ", (E12, 3), KNG % ;
WRITE 1, "KNE = ", (E12, 3), KNE % ;
WRITE 1, "KKQ = ", (E12, 3), KKQ % ;
WRITE 1, "KLQ = ", (E12, 3), KLQ % ;
WRITE 1, "KGQ = ", (E12, 3), KGQ % ;
WRITE 1, "KLG = ", (E12, 3), KLG % ;
WRITE 1, "KLN = ", (E12, 3), KLN % ;
WRITE 1, "KEC2 = ", (E12, 3), KEC2 % ;
WRITE 1, "KAN2 = ", (E12, 3), KAN2 % ;
WRITE 1, "KRC = ", (E12, 3), KRC % ;
WRITE 1, "----PRE-EXPONENTIAL-FACTORS----", %;
WRITE 1, "AAB = ", (E12, 3), AAB % ;
WRITE 1, "AAF = ", (E12, 3), AAF % ;
WRITE 1, "AAG = ", (E12, 3), AAG % ;
WRITE 1, "AAM = ", (E12, 3), AAM % ;
WRITE 1, "AAN = ", (E12, 3), AAN % ;
WRITE 1, "ABB = ", (E12, 3), ABB % ;
WRITE 1, "ABC = ", (E12, 3), ABC % ;
WRITE 1, "ABG = ", (E12, 3), ABG % ;
WRITE 1, "ABN = ", (E12, 3), ABN % ;
WRITE 1, "ABF = ", (E12, 3), ABF % ;
WRITE 1, "ACF = ", (E12, 3), ACF % ;
WRITE 1, "ACL = ", (E12, 3), ACL % ;
WRITE 1, "ACG = ", (E12, 3), ACG % ;
WRITE 1, "ACN = ", (E12, 3), ACN % ;
WRITE 1, "ADR = ", (E12, 3), ADR % ;
WRITE 1, "ADL = ", (E12, 3), ADL % ;
WRITE 1, "AFNI = ", (E12, 3), AFNI % ;
WRITE 1, "AFF = ", (E12, 3), AFF % ;
WRITE 1, "ADM = ", (E12, 3), ADM % ;
WRITE 1, "AG = ", (E12, 3), AG % ;
WRITE 1, "AAN2 = ", (E12, 3), AAN2 % ;
WRITE 1, "AGQ = ", (E12, 3), AGQ % ;
WRITE 1, "AFN = ", (E12, 3), AFN % ;
WRITE 1, "ANN = ", (E12, 3), ANN % ;
WRITE 1, "ACL2 = ", (E12, 3), ACL2 % ;
WRITE 1, "ABF2 = ", (E12, 3), ABF2 % ;
WRITE 1, "ABL = ", (E12, 3), ABL % ;
WRITE 1, "AAD = ", (E12, 3), AAD % ;
WRITE 1, "AAL = ", (E12, 3), AAL % ;
WRITE 1, "ADG = ", (E12, 3), ADG % ;
WRITE 1, "AEG = ", (E12, 3), AEG % ;
WRITE 1, "AEL = ", (E12, 3), AEL % ;
WRITE 1, "AER = ", (E12, 3), AER % ;
WRITE 1, "AFG = ", (E12, 3), AFG % ;
WRITE 1, "----ACTIVATION ENERGIES----", %;
WRITE 1, "EAG = ", (E12, 3), EAG % ;
```

```
WRITE 1, "EAM = ", (E12, 3), EAM % ;
WRITE 1, "EAN = ", (E12, 3), EAN % ;
WRITE 1, "EBG = ", (E12, 3), EBG % ;
WRITE 1, "ECG = ", (E12, 3), ECG % ;
WRITE 1, "ECL = ", (E12, 3), ECL % ;
WRITE 1, "ECF = ", (E12, 3), ECF % ;
WRITE 1, "ECN = ", (E12, 3), ECN % ;
WRITE 1, "EFN = ", (E12, 3), EFN % ;
WRITE 1, "EFNI = ", (E12, 3), EFNI % ;
WRITE 1, "ECL2 = ", (E12, 3), ECL2 % ;
WRITE 1, "EAN2 = ", (E12, 3), EAN2 % ;

WRITE 1, "---pKa----", %;
WRITE 1, "pKw = ", (E12, 3), pKw %;
WRITE 1, "pKH2O2 =", (E12, 3), pKH2O2 %;
WRITE 1, "pKHO2 = ", (E12, 3), pKHO2 %;
WRITE 1, "pKOH = ", (E12, 3), pKOH %;
WRITE 1, "pKH = ", (E12, 3), pKH %;
WRITE 1, "pKH2O = ", (E12, 3), pKH2O %;
WRITE 1, "Kprot = ", (E12, 3), Kprot %;
WRITE 1, "Khydx = ", (E12, 3), Khydx%;
WRITE 1, "KappO2 = ", (E12, 3), kappO2%;
WRITE 1, "KappH2 = ", (E12, 3), kappH2%;
WRITE 1, "H2O2 Equ rate = ", (E12, 3), EqR%;

**;
SETHMAX 1;
BEGIN;
STOP;
```

Radiolysis Model Full Reaction Scheme

#	Primary Reaction	G-value (Molecules/100eV)	Temperature Dependency	Ref
G0	$H_2O \rightsquigarrow \cdot e^-_{aq}$	2.71	$2.641 + 4.162\times10^{-3}\,t + 9.093\times10^{-6}\,t^2 - 4.717\times10^{-8}\,t^3$	45
G1	$H_2O \rightsquigarrow H\cdot$	0.54	$0.556 + 2.198\times10^{-3}\,t - 1.184\times10^{-5}\,t^2 + 5.223\times10^{-8}\,t^3$	45
G2	$H_2O \rightsquigarrow H_2$	0.41	$0.419 + 8.721\times10^{-4}\,t - 4.971\times10^{-6}\,t^2 + 1.503\times10^{-8}\,t^3$	45
G3	$H_2O \rightsquigarrow \cdot OH$	2.70	$2.531 + 1.134\times10^{-2}\,t - 1.269\times10^{-5}\,t^2 + 3.513\times10^{-8}\,t^3$	45
G4	$H_2O \rightsquigarrow H_2O_2$	0.68	$0.752 - 1.620\times10^{-3}\,t$	45
G5	$H_2O \rightsquigarrow H^+$	2.71	$2.641 + 4.162\times10^{-3}\,t + 9.093\times10^{-6}\,t^2 - 4.717\times10^{-8}\,t^3$	45

#	Chemical Reaction	Rate Constant k ($M^{-1}\,s^{-1}$ @25°C)	Arrhenius	Activation Energy Ea (kJ)	Ref
R0	$\cdot e^-_{aq} + \cdot e^-_{aq} \rightarrow H_2 + 2OH^-$	7.260×10^{9}	$\log k_{R7} = 12.281 - 3.768\times10^{2}/T - 6.673\times10^{4}/T^2 - 1.075\times10^{7}/T^3$		45
R1	$\cdot e^-_{aq} + H\cdot \rightarrow H_2 + OH^-$	2.762×10^{10}	1.14×10^{13}	14.929	45
R2	$\cdot e^-_{aq} + \cdot OH \rightarrow OH^-$	3.553×10^{10}	$\log k_{R9} = 13.123 - 1.023\times10^{3}/T + 7.634\times10^{4}/T^2$		45
R3	$\cdot e^-_{aq} + \cdot O^- \rightarrow 2OH^-$	2.313×10^{10}	5.6×10^{11}	7.9	49
R4	$\cdot e^-_{aq} + H_2O_2 \rightarrow OH^- + \cdot OH$	1.362×10^{10}	7.7×10^{12}	15.71	45
R5	$\cdot e^-_{aq} + HO_2\cdot \rightarrow HO_2^-$	1.300×10^{10}	2.46×10^{12}	13.0	45
R6	$\cdot e^-_{aq} + HO_2^- \rightarrow O\cdot^- + OH^-$	3.507×10^{9}	1.75×10^{12}	15.4	49
R7	$\cdot e^-_{aq} + O_2 \rightarrow O_2\cdot^-$	2.253×10^{10}	2.52×10^{12}	11.652	45
R8	$\cdot e^-_{aq} + O_2\cdot^- \rightarrow O_2^{2-} + H_2O$	1.300×10^{10}	3.1×10^{12}	13.6	43,49
R9	$H\cdot + H\cdot \rightarrow H_2$	5.142×10^{9}	2.7×10^{12}	15.526	45
R10	$H\cdot + \cdot OH \rightarrow H_2O$	1.094×10^{10}	4.26×10^{11}	9.078	45
R11	$H\cdot + H_2O_2 \rightarrow \cdot OH + H_2O$	3.650×10^{7}	1.79×10^{11}	21.064	45
R12	$H\cdot + O_2 \rightarrow HO_2\cdot$	1.304×10^{10}	$\log k_{R23} = 10.704 + 2.840\times10^{2}/T - 1.369\times10^{5}/T^2$		45
R13	$H\cdot + O_2\cdot^- \rightarrow HO_2^-$	1.138×10^{10}	5.17×10^{12}	15.166	45
R14	$H\cdot + HO_2\cdot \rightarrow 2OH$	1.138×10^{10}	5.17×10^{12}	15.166	45
R15	$H\cdot + HO_2^- \rightarrow \cdot OH + OH^-$	1.374×10^{9}	4.2×10^{13}	25.6	85
R16	$H\cdot + O_3 \rightarrow \cdot OH + O_2$	2.200×10^{10}	No temperature dependence available		43
R17	$\cdot OH + \cdot OH \rightarrow H_2O_2$	4.814×10^{9}	$\log k_{R25} = 8.054 + 2.193\times10^{3}/T - 7.395\times10^{5}/T^2 + 6.870\times10^{7}/T^3$		45
R18	$\cdot OH + H_2O_2 \rightarrow H_2O + HO_2\cdot$	2.920×10^{7}	7.68×10^{9}	13.813	45
R19	$\cdot OH + HO_2^- \rightarrow OH^- + HO_2\cdot$	8.134×10^{9}	1.00×10^{12}	11.927	45
R20	$\cdot OH + HO_2\cdot \rightarrow H_2O + O_2$	8.840×10^{9}	1.29×10^{11}	6.645	45

R21	$\cdot OH + O_2\cdot^- \rightarrow OH^- + O_2$	1.097×10^{10}	8.77×10^{11}	10.860	45
R22	$\cdot OH + O_3 \rightarrow HO_2\cdot + O_2$	1.100×10^{8}	No temperature dependence available		43
R23	$\cdot O_3^- + H_2O_2 \rightarrow O_2\cdot^- + O_2 + H_2O$	1.590×10^{6}	xEXP(18.8×10^3 (1/298.15 – 1/TK)/R)		43
R24	$\cdot O_3^- + HO_2^- \rightarrow O_2\cdot^- + O_2 + OH^-$	8.870×10^{5}	xEXP(18.8×10^3 (1/298.15 – 1/TK)/R)		43
R25	$\cdot O_3^- + H_2 \rightarrow O_2 + H\cdot + OH^-$	2.490×10^{5}	xEXP(18.8×10^3 (1/298.15 – 1/TK)/R)		46
R26	$\cdot O_3^- + \cdot OH \rightarrow HO_2\cdot + O_2\cdot^-$	6.000×10^{9}	No temperature dependence available	4,6	43
R27	$\cdot O_3^- + \cdot OH \rightarrow HO^- + O_3$	2.500×10^{9}	No temperature dependence available	4,6	43
R28	$\cdot O_3^- + H^+ \rightarrow O_2 + \cdot OH$	9.000×10^{10}	No temperature dependence available	4	43
R29	$O_2\cdot^- + O_2\cdot^- \rightarrow O_2 + O_2^{2-}$	2.988×10^{-1}	4.89×10^{8}	52.59	43
R30	$O_2\cdot^- + HO_2^- \rightarrow O_2 + O^- + OH^-$	8.230×10^{-2}	No temperature dependence available	4	43
R31	$O_2\cdot^- + H_2O_2 \rightarrow O_2 + \cdot OH + OH^-$	1.300×10^{-1}	No temperature dependence available	4	43
R32	$O_2\cdot^- + HO_2\cdot \rightarrow O_2 + HO_2^-$	7.597×10^{7}	2.44×10^{9}	8.6	43
R33	$O_2\cdot^- + \cdot O_3^- \rightarrow O^{2-} + 2O_2$	1.000×10^{4}	No temperature dependence available	4,7	43
R34	$O_2\cdot^- + O_3 \rightarrow \cdot O_3^- + O_2$	1.500×10^{9}	No temperature dependence available	4	43
R35	$HO_2\cdot + HO_2\cdot \rightarrow H_2O_2 + O_2$	8.399×10^{5}	2.78×10^{9}	20.1	45
R36	$HO_2\cdot + H_2O_2 \rightarrow O_2 + H_2O + \cdot OH$	5.000×10^{-1}	No temperature dependence available	4	49
R37	$HO_2\cdot + O_3 \rightarrow \cdot OH + 2O_2$	5.000×10^{8}	No temperature dependence available	4	43
R38	$H_2O_2 + HO_2^- \rightarrow O_2 + H_2O + OH^-$	4.50×10^{-4}	No temperature dependence available	4	43
R39	$O_3 + OH^- \rightarrow HO_2^- + O_2$	4.800×10^{1}	No temperature dependence available	4	43
R40	$O_3 + HO_2^- \rightarrow \cdot OH + O_2 + O_2\cdot^-$	5.500×10^{6}	No temperature dependence available	4	43
R41	$O_3 + H_2O_2 \rightarrow \cdot OH + O_2 + HO_2\cdot$	3.714×10^{-2}	2.8×10^{11}	73.5	43
R42	$H\cdot + \cdot O^- \rightarrow OH^-$	2.000×10^{10}	No temperature dependence available	4	43
R43	$\cdot O_3^- + \cdot e^-_{aq} \rightarrow 2OH^- + O_2$	1.600×10^{10}	No temperature dependence available	4,7	43
R44	$O_3 + \cdot e^-_{aq} \rightarrow \cdot O_3^-$	3.600×10^{10}	No temperature dependence available	4	43
R45	$H_2O_2 \rightarrow 2\cdot OH$	2.300×10^{-7}	No temperature dependence available	-	86
R46	$O^{2-} + H_2O \rightarrow 2OH^-$	1.000×10^{10}	No temperature dependence available	-	43
R47	$\cdot O^- + H_2 \rightarrow \cdot H + OH^-$	1.279×10^{8}	2.32×10^{10}	12.891	45
R48	$\cdot O^- + H_2O_2 \rightarrow O_2\cdot^- + H_2O$	5.546×10^{8}	3.0×10^{11}	15.6	49
R49	$\cdot O^- + HO_2^- \rightarrow O_2\cdot^- + OH^-$	7.864×10^{8}	1.45×10^{13}	24.348	45
R50	$\cdot O^- + O_2\cdot^- \rightarrow O^{2-} + O_2$	6.000×10^{8}	No temperature dependence available	4,6	43
R51	$\cdot O^- + \cdot O^- \rightarrow O_2^{2-}$	1.000×10^{8}	No temperature dependence available	4	43
R52	$\cdot O^- + \cdot OH \rightarrow HO_2^-$	7.610×10^{9}	1.7×10^{11}	7.7	49

R53	$\cdot O^- + O_3^- \rightarrow 2O_2\cdot^-$	7.000×10^8	No temperature dependence available		4,6		43
R54	$O^- + O_3 \rightarrow O_2\cdot^- + O_2$	1.000×10^9	No temperature dependence available		4		43

	Equilibria	k_f (M^{-1} s^{-1})	k_b (M^{-1} s^{-1})	Temperature Dependence			pKa (25°C)	
R55/56	$H_2O \rightleftharpoons H^+ + OH^-$	1.172×10^{-3}	1.178×10^{11}	$\log k_{R67} = 20.934 - 1.236\times10^4/T + 6.364\times10^6/T^2 - 1.475\times10^9/T^3 + 1.237\times10^{11}/T^4$			15.75	45
R57/58	$H_2O_2 \rightleftharpoons H^+ + HO_2^-$	8.900×10^{-2}	4.780×10^{10}	$\log k_{R68} = 16.410 - 4.888\times10^3/T + 1.622\times10^6/T^2 - 2.004\times10^8/T^3$			11.73	45
R59/60	$H_2O_2 + OH^- \rightleftharpoons HO_2^- + H_2O$	1.265×10^{10}	1.403×10^6	$\log k_{R75} = 13.339 - 2.220\times10^3/T + 7.333\times10^5/T^2 - 1.065\times10^8/T^3$			$\frac{K_{H_2O}}{K_{H_2O_2}}$	45
R61/62	$HO_2^- + OH^- \rightleftharpoons O_2^{2-} + H_2O$	3.506×10^5	1.103×10^6	3.39×10^8	14.2		16.5	43
R63/64	$\cdot OH \rightleftharpoons H^+ + \cdot O^-$	8.900×10^{-2}	4.780×10^{10}	$\log k_{R66} = 16.410 - 4.888\times10^3/T + 1.622\times10^6/T^2 - 2.004\times10^8/T^3$			11.73	45
R65/66	$\cdot OH + OH^- \rightleftharpoons \cdot O^- + H_2O$	1.265×10^{10}	1.403×10^6	$\log k_{R72} = 13.339 - 2.220\times10^3/T + 7.333\times10^5/T^2 - 1.065\times10^8/T^3$			$\frac{K_{H_2O}}{K_{OH}}$	45
R67/68	$\cdot O^- + O_2 \rightleftharpoons \cdot O_3^-$	3.747×10^9	2.617×10^3	3.41×10^{11}	11.182	Forward		45
				3.20×10^{11}	46.16	Reverse		45
R69/70	$HO_2\cdot \rightleftharpoons H^+ + O_2\cdot^-$	4.780×10^{10}	7.354×10^5	$\log kR69 = 16.410 - 4.888x103/T + 1.622x106/T2 - 2.004x108/T3$			4.81	45
R71/72	$HO_2\cdot + OH^- \rightleftharpoons O_2\cdot^- + H_2O$	1.265×10^{10}	1.628×10^{-1}	$\log kR75 = 13.339 - 2.220x103/T + 7.333x105/T2 - 1.065x108/T3$			$\frac{K_{H_2O}}{K_{HO_2}}$	45
R73/74	$H\cdot \rightleftharpoons \cdot e^-_{aq} + H^+$	5.832	2.095×10^{10}	$\log kR74 = 39.127 - 3.888E4/T + 2.054E7/T2 - 4.899E9/T3 + 4.376E11/T4$			9.55	45
R75/76	$H\cdot + OH^- \rightleftharpoons \cdot e^-_{aq} + H_2O$	2.440×10^7	1.735×10^1	$\log kR70 = 22.970 - 1.971x104/T + 1.137x107/T2 - 2.991x109/T3 + 2.803x1011/T4$			$\frac{K_{H_2O}}{K_H}$	45
R77/78	$H\cdot + H_2O \rightleftharpoons H_2 + \cdot OH$	4.575×10^{-5}	3.954×10^7	$\log k_{R71f} = 9.408 - 2.827x10^3/T - 3.792x10^5/T^2$				45
				$\log k_{R71b} = -11.556 + 3.2546x10^4/T - 1.8623x10^7/T^2 + 4.5543x10^9/T^3 - 4.1364x10^{11}/T^4$				45
R79	$H_{2(aq)} \rightleftharpoons H_{2(g)}$	2.687×10^{-3}		See Chapter 3				
R80	$O_{2(aq)} \rightleftharpoons O_{2(g)}$	1.033×10^{-4}		See Chapter 3				